# THE AUTONOMOUS UNDERWATER VEHICLE EMERGENCY LOCALIZATION SYSTEM
## An under ice AUV tracking technology for over-the-horizon operations

by

**©Ronald Stephen Lewis**

B.Sc.H. (Mathematics and Statistics), Acadia University, 1998
M.Sc. (Mathematics), Memorial University of Newfoundland, 2003
M.Eng., Memorial University of Newfoundland

A Thesis submitted to the
School of Graduate Studies and
the Graduate Research Office
in partial fulfillment of the
requirements for the degree of
Doctor of Philosophy

Faculty of Engineering and Applied Science
Memorial University of Newfoundland

National Centre for Maritime Engineering and Hydrodynamics
Australian Maritime College - University of Tasmania

December 2015

# Abstract

There is an inherent risk of loss that accompanies any operations of Autonomous Underwater Vehicle (AUV) technology. This complexity and risk are increased for AUV missions that are conducted beneath ice and in harsh environmental conditions (i.e. extreme cold, compromised visibility, etc.). Risk-based methodologies have been developed to quantify the risk of loss for specific AUV platforms prior to deployments. Their goal is to identify and mitigate where possible the significant contributors (technical or otherwise) to the overall risk of a specific operation. Not surprisingly, there is an abundant amount of literature related to successful AUV missions; however, there has been very little published work related to AUV loss. Specifically, this author is not aware of any examples of a developed procedure to employ during an AUV loss event to date, much less specific algorithms developed to locate a missing AUV. This is a subset of the AUV tracking or positioning that is rarely given specific treatment.

The motivating problem is based on the loss event of an AUV during polar operations. For example, (i) the vehicle might navigate outside of its predefined spatial area through some fault or error, or, (ii) its mission involves over-the-horizon operations, i.e. beyond the range of standard acoustical tracking technologies. In either circumstance, at the end of its pre-programmed mission, the AUV fails to return to the base station. Such an eventuality defines the need for reliable, long-range acoustic tracking capability that is able to coarsely localize the AUV and subsequently enable communications and/or recovery of the AUV.

The thesis describes a novel approach for an acoustic positioning system for AUV localization in harsh environments with non-standard acoustic challenges that can be implemented using only basic acoustic technology, a basic single-beacon, single-hydrophone (SBSH) system. Inversive geometric techniques are applied for source localization of a one-way traveling, asynchronous acoustic signal. This differs from the usual methods of spherical, two-way direct flight measurement based on time of arrival (TOA), or hyperbolic, one-way time difference of arrival (TDOA) target tracking for transmission based on a purely Euclidean geometry. This is a novel approach to the problem of localizing an AUV.

A second method of solving the non-linear system of equations that arise from the problem using the SBSH approach is derived. Both methods, the novel Apollonian inversion geometry localization (AIGL) and the non linear system localization (NLSL), are evaluated in simulation and using live field data. It will be shown that

the novel algorithm performs comparable to the standard method of solving the non-linear systems resulting from a SBSH approach. Furthermore, in certain situations it improves the localization result.

# Dedication

My doctoral thesis and degree represent a high point on a journey that started years ago when I was five and first went to school. In the thirty-five years that have since passed, I have always had a lust for learning and a zeal for knowledge. Thank you to my teachers and my students that have fed these desires over the years.

This thesis is dedicated to my large family, all of whom have placed a premium on education in all its forms. Specifically, thank you to my parents and of course, my beloved wife, Sara, and our children, Christina and Jack. Your unwavering support, sacrifice and love have made this possible.

In particular, my thesis is dedicated to the memory of two very important ladies originally from Marquise, Placentia Bay that passed away during my program. Both had a significant influence on my educational aspirations and were dear to me.

'Aunt' Bride Wyse, 1915 - 2010

Patricia 'Mom' Dawson, 1923 - 2014

And to my Uncle, John Dawson, 1945 - 2014

# Acknowledgements

Thank you to my supervisors Dr. Ralf Bachmayer, Professor Neil Bose, Professor George Mann and Dr. Christopher Williams for their assistance and guidance over the years. Sincere gratitude and thanks to Professor Neil Bose at the Australian Maritime College - University of Tasmania, a great supervisor, colleague and friend; and Professor George Mann at Memorial University of Newfoundland, without whose timely support I would never have embarked upon my doctoral program.

I wish to acknowledge my graduate funding from Memorial University's School of Graduate Studies (F. A. Aldrich Fellowship), Natural Science and Engineering Research Council of Canada (Postgraduate Scholarship Doctoral Award) and the Atlantic Canada Opportunities Agency (ACOA) Atlantic Innovation Fund. I have studied and worked at Memorial for almost 15 years and am truly appreciative of the Institution, its staff, students and faculty. Memorial University has enabled me to live a life in a part of the world that I cherish deeply.

The support of the Australian Maritime College has been significant. In addition to my conjoint doctoral program, AMC and Neil Bose have afforded me a once in lifetime opportunity to conduct my research in Antarctica . . . twice.

Thank you to Peter King for your sense of humour, lightning quick wit and fun years working together in the lab and in the field. Lending your technical expertise and enthusiasm were greatly appreciated. Thanks to Dan Walker for rejoining MERLIN

and for being a constant source of encouragement during the final few, critical miles of my program.

# Table of Contents

# List of Tables

# List of Figures

# List of Acronyms

| | |
|---|---|
| AIGL | Apollonian inversion geometry localization |
| AUV | Autonomous underwater vehicle |
| CPU | Central processing unit |
| DR | Deduced reckoning or dead reckoning |
| DVL | Doppler velocity log |
| ELS | Emergency localization system |
| GPS | Global positioning system |
| INS | Inertial navigation system |
| LBL | Long baseline system |
| LORAN | Long range navigation |
| NLSL | Non linear system localization |
| OWTT | One way travel time |
| RF | Radio frequency |
| ROV | Remotely operated vehicle |
| Rx | Receiver |
| SBL | Short baseline system |
| SBSH | Single-beacon, single-hydrophone |
| SONAR | Sound navigation and ranging |
| SSBL | Super-short baseline system |
| TDOA | Time difference of arrival |
| TOA | Time of arrival |
| Tx | Transmitter (a.k.a. source) |
| USBL | Ultra-short baseline system |

# Chapter 1

# Introduction

## 1.1 Problem statement

The question: "What should one do when an AUV is lost?" goes unanswered in the majority of the current literature. There are no accredited sources on the detailed steps or procedures to implement in order to locate a lost asset to date. There have been bodies of work associated with planning strategies for successful operations [1–3]; reliability and risk mitigation to prevent loss occurrences [4–8]; obtaining insurance in advance in case of loss or damage [9, 10]; and studies of technical loss [11].

The seldom cited and appropriately titled Ferguson publication, "When things go horribly wrong," [12] has some content devoted to possible actions during a loss event. However, it is predominantly concerned with identifying best practices to increase the likelihood of a successful mission. Given the increasing number of AUV operations worldwide, the number of loss events will increase as the technology sees greater usage by a broader range of operators with varying levels of experience and expertise. The ever growing community of AUV developers and users would benefit from frank and candid details of less positive AUV experiences such as in [13–15]. Frequently,

these critical details are overlooked in the literature when, and quite understandably, the focus is on the important data collected [16] and/or the impressive operation itself [17, 18].

## 1.2 Technological motivation

When an AUV is operating beneath the sea surface and without an external positional update, its deduced or 'dead' reckoning (DR) navigation error will grow unbounded. In DR navigation the vehicle estimates its current position based on its previous position and a set of sensor inputs (velocity, heading, depth, attitude, etc.) to generate a current position solution.

Mission requirements dictate the tolerable limits of the magnitude of the navigation error. Certain data sets such as precision seabed surveys require spatial resolution on the order of centimetre to metre scale for data reconciliation, whereas some oceanographic profiling (temperature, conductivity and salinity) are not as spatially sensitive. Regardless, in all cases there is a requirement to recover the AUV. Poor localization has the potential to complicate the recovery process, and in extreme cases, can lead to asset loss.

Generally, underwater acoustic positioning systems are used to supplement inertially aided AUV navigation systems by providing an external position estimate. Commercially available acoustic positioning technologies include long baseline systems (LBL) or ultra short baseline systems (USBL). Each system has its particular strengths and weaknesses related to ease of deployment, cost, environmental performance, and range.

In some ways, AUVs have advanced considerably as a technology since their inception in the 1970s. This is especially true in terms of the number of platforms,

and the scope and the nature of the work being undertaken. In all but a few cases, operations rely on the traditional acoustic positioning systems. Generally, AUV mission specifications are such that the existing technologies (LBL, USBL) are acceptable. However, as AUV technology is pushed and pulled into application areas with non-standard operational and environmental characteristics, the existing technologies sometimes cannot deliver the required localization capability. Rapid deployment of a LBL array in an ice covered environment is not possible with the current state of the art of that technology. USBL technology has greater mobility, but it relies on two-way communications and frequencies ranges that are not optimally suited for acoustic ranging and localization as part of an emergency AUV response action in a polar environment. In this thesis, a single-beacon, single-hydrophone (SBSH) system is proposed to address this technological gap. The SBSH system utilizes a series of recordings from a sequentially deployed single hydrophone of a single free running acoustic beacon to remotely localize the beacon's position in two dimensions.

## 1.3 Objectives

The motivation for undertaking this research topic is born from first-hand experiences of operating AUV assets in challenging and harsh environments coupled by a lack of satisfaction with the performance of currently available commercial-off-the-shelf technologies for this application. A practical illustration of the utility for this research is during the performance of under-ice science missions using AUV technology such as [19, 20] resulting in undesired outcomes as described in [11]. The goal of the research is to develop a novel method of deriving AUV location using basic system constraints [21] and then establish a detailed process for emergency localization of an AUV.

The approach is to use a basic acoustic signal for remote localization of a signal source based purely on time difference of arrival (TDOA), as opposed to intensity. Notionally, the proposed algorithm will enable determination of the spatial position of the source to a minimal resolution threshold compatible with standard subsea acoustic modem technology, i.e. on the range of metres. The targeted acoustic technology is in the low frequency band (approximately 10 kHz) to reduce signal attenuation and improve signal propagation distance potential. The method calls for acquiring a series of sound measurements at different locations. Essentially, by timing the signal's difference in time of arrival at these different receiving locations it is possible to determine some information regarding the range to the signal source, i.e. how much further or closer the source is located using inversive geometry. In four measurements it is possible to determine the location of a stationary source.

This is an alternative approach to hyperbolic tracking methods employed in standard LBL systems for under ice AUV applications and other difficult acoustic environments, i.e. susceptible to multi-path (see Figure 1.1). Sometimes an AUV, either by mission design or accidentally, operates outside of its pre-defined spatial working area and beyond the acoustic tracking range, i.e. over-the-horizon. The physical nature for over-the-horizon, under ice missions and harshness of that environment result in degraded performance for the standard acoustic tracking technologies employed for open water AUV operations hence the need for an alternative system: the AUV Emergency Localization System (ELS).

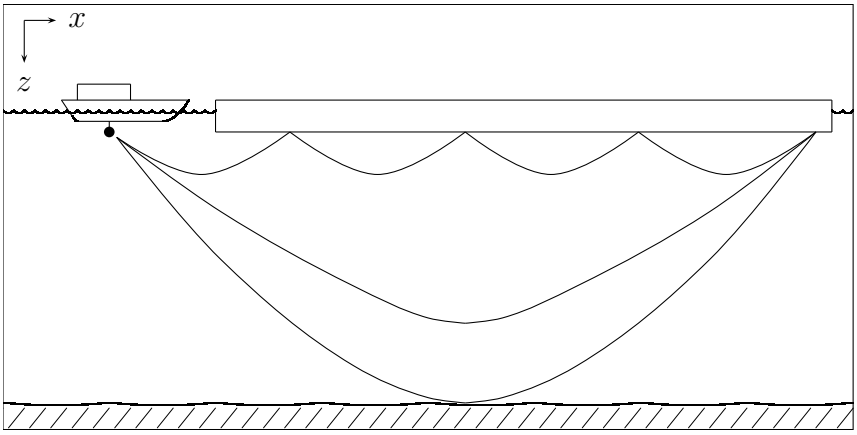


Figure 1.1: Acoustic multi-path in a polar environment. Three possible paths for acoustic propagation beneath an ice layer.

## 1.4 Thesis organization

Chapter Two is the literature review for the thesis. It commences with a brief introduction to AUVs and their foundational developments and operations. Highlights of polar environment deployments are provided. This general background information frames the overall context for the area of application for the proposed research. It is an opportunity to appreciate where AUV technology is being applied and the technological challenges for successful operations.

The standard approaches to acoustic tracking are explained. Specific detail and attention is given to the most widely used, commercially available acoustic measurement systems: short baseline, ultra-short baseline and long baseline. It is very important to recognize systems that function reliably because, in practice, such systems will be relied upon by operators to achieve successful AUV missions. A close examination of the system geometries and algorithmic approaches of these standard technologies enable an appreciation of the differences with the alternative methods of this proposal.

The proposed localization research represents a slight divergence from the stan-

dard acoustic positioning technologies. A review of the current literature with respect to other non-standard beacon/transponder work is provided. It should be noted that all of this work is in the context of AUV navigation. Localization is intertwined with navigation in many instances, so this non-standard work bears referencing. Biological applications of acoustic localization technology are discussed to conclude the literature survey component of the thesis.

The novel localization techniques are introduced in Chapter Three. A high level overview of the technological framework and considerations are presented. Specifically, the acoustic signal characteristics, the geometric interpretation and the mathematical theory are discussed in relation to the problem space. These elements establish the foundation for the SBSH algorithm developments at the core of this research: the Apollonian Inversion Geometry Localization (AIGL) and Non-linear System Localization (NLSL) algorithms.

In Chapter Four, a complete example is explained in order to illustrate the specific details of the AIGL algorithm. The algorithm is divided into separate sections. A series of accurate graphic illustrations accompanied by pseudocode for the relevant sections is included. The chapter concludes with a restatement of the problem using a different mathematical treatment. The non-linear system representation of the problem is explained and a solution using the NLSL algorithm is determined.

The SBSH algorithms are tested extensively in simulation. Algorithm performance is tested for a series of progressively larger simulated source location regions. Chapter Five contains the results of the simulations to gauge the numerical error of the SBSH algorithm implementation. Chapter Six is another series of simulations of the SBSH algorithm with external error included in the simulations for the same source region dimensions from Chapter Five. In Chapter Seven, the receiver array dimensions are varied for different source location regions. Chapter Eight describes

field testing and the results of applying the SBSH algorithms against actual acoustic data sets collected through the ice in Antarctica.

Chapter Nine contains the conclusion of the thesis, the contributions to research and suggestions for future research work efforts related to this localization approach.

# Chapter 2

# Context and Literature Review

## 2.1 Autonomous Underwater Vehicles

A general definition for an AUV (partially taken from [22]) is a self-powered, self-controlled robot capable of autonomous navigation and data collection in the undersea environment, and requires no communication in order to complete its preassigned mission. It is part of the broader family of unmanned submersibles that includes towed bodies, remotely operated vehicles (ROVs) and unmanned, untethered vehicles which require a degree of real time remote operation [22]. AUVs are typically divided into classes either based on usage: research, industrial and military [23], or by size [24, 25]. There are certain advantages inherent with this technology. In most cases, it enables the collection of spatially richer data sets compared to traditional point sampling methods using sensor casts or drop cameras from surface ships. Data sets collected from sensors deployed on an AUV will be significantly dense compared to traditional discrete data collection with sensors that interrogate the water column itself. Suitably-sized and reasonably-powered sound navigation and ranging or *sonar* devices deployed from AUVs result in superior data quality compared to traditional

ship-based deployments. The benefits of greater platform stability in terms of yaw, pitch and roll; superior depth and altitude control; and isolation from acoustic interference in the form of surface and ship noise culminate in sonar data products that require less post-processing and yield improved target resolution. AUVs are also particularly effective when used as a delivery platform of scientific payloads and sensors for environments that are otherwise unreachable by surface vessels, manned submersibles or tethered ROVs due to obstructions such as ice, extreme depths, or exceptional unmitigatable risk.

### 2.1.1 A short history of AUVs

The precursor to AUV technology was developed in the 1950s: a series of unmanned, untethered submersibles developments that were remotely controlled. The Self Propelled Underwater Research Vehicles (SPURVs) were developed by the Applied Physics Laboratory, University of Washington in the 1960s [26,27]. The first reported "AUV" missions were from an American Navy vessel in 1957 used to explore Cobb Seamount off the coast of the state of Washington. The first descriptions of this AUV technology in the literature is due to W. Nodland, one of the co-developers of the SPURV series of platforms [28]. An arctic variant of the SPURV was the Unmanned Arctic Research Vehicle and was developed in the early 1970s [29–31]. It was an acoustically controlled platform [32]. The deep water EPAULARD vehicle was another acoustically controlled free swimming vehicle that conducted dives up to 5300 m. This platform was developed in France at the Centre National pour l'Exploitation des Ocean (CNEXO), now known as Institute français de recherche pour l'exploitation de la mer (Ifremer) [33,34]. The Canadian built Autonomous Remotely Controlled Submersible (ARCS) is considered to be the first truly autonomous platform as it operated without the mechanical or acoustic tether of its predecessors [35]. The platform was in

its concept stages in 1981 [36]. This International Submarine Engineering Ltd. (ISE) platform became operational in 1983 and was the first to conduct an AUV hydrographic survey [37]. ARCS was used as the half scale model for the Theseus AUV built by ISE for specific defense establishment requirements, specifically for laying a 200 km cable beneath ice in the Canadian Arctic [17].

Parallel AUV development efforts occurred at the Institute of Marine Technology Problems (IMTP) in Russia during the 1970s and into the 1980s. The American Office of Naval Research and National Science Foundation commissioned a technical assessment group, the World Technology Evaluation Center (WTEC), to conduct an international technical assessment in specific areas including underwater technology. A WTEC panel sent to Europe and Asia concluded in 1996 after a series of visits to Russian Institutes, that the IMTP had amassed a greater amount of AUV operational experience compared to AUV work in the United States [38]. The SKAT-GEO AUV series of developments also took place in the 1970s and 1980s. This institute developed additional vehicles late in this period including the L2 capable of 6000 m operations. IMTP introduced a third deepwater AUV, the MT-88 and the Southwest Research Institute introduced its Large Scale Vehicle LSV-1 which was 27 m in length, the largest AUV to date. The American Naval Ocean Systems Centre commenced its own developments of AUV technology in the mid 1970s. It culminated with the launch of the Advanced Unmanned Search System (AUSS) in 1983 [39, 40].

The other major vehicle development during this time period was out of the Marine Systems Engineering Lab at the University of New Hampshire in the United States. The EAVE program resulted in a series of platform developments in the 1970s and 1980s including the EAVE East [41–44], EAVE West [45–47] and EAVE III [48]. By the end of the 1980s the developmental progress and demonstrated results of AUV technology were recognized as taking the technology from an immature state toward

a more stable state suitable for regular, repeatable operations [49].

In Japan, the University of Tokyo's PTEROA Project which had started in the mid 1980s successfully developed a vehicle by 1990, the PTEROA150 [50]. Not long afterward, another platform, the Aqua Explorer 1000 was designed, built and tested in 1992, specifically for inspection of underwater cables. This platform was developed by KDD Laboratories [51, 52]. A somewhat similar flatfish-shaped AUV, the Marine Utility Vehicle System (MARIUS) originated in Denmark under the Marine Science and Technology Program of the Commission of the European Communities [53, 54].

In the 1990s and through to the 21st century usage of AUV technology both in the scientific community and commercial domains has increased significantly compared to the previous decades. The Autosub program based out of the National Oceanography Centre (NOC) in the United Kingdom has made significant contributions to oceanographic science and engineering [19]. The multiphase Autosub program commenced in 1988 and was originally administered out of the Institute of Ocean Sciences Deacon Laboratory [55]. The Autosub project evolved from a AUV developmental project of two application specific AUV platforms, the Deep Ocean Long Path Hydrographic Instrument and Deep Ocean Geophysical Instrument Explorer [56], into the design and build of a platform called the Autosub [57–59]. At the turn of the millennium the Autosub program transitioned toward a focus on under ice-operations [60].

The Massachusetts Institute of Technology AUV Lab and Draper Lab developed the Sea Squirt AUV as a testbed during this period [61]. The Odyssey series of AUVs came into being in the early 1990s [62]. The Odyssey quickly spawned Odyssey II [63, 64] which was commercialized in the late 1990s. This was the birth of Bluefin Robotics Inc., now a major AUV manufacturer [65].

The Woods Hole Oceanographic Institution (WHOI) has developed several AUV

platforms starting in the mid 1990s. The Autonomous Benthic Explorer (ABE) was one of the first AUVs with four actuated degrees of freedom [66, 67]. Following ABE, it was the Remote Environmental Monitoring Units (REMUS) vehicle series out of WHOI's Ocean Systems Lab in the late 1990s [68]. In 2001, Hydroid Inc. was created to commercialize and develop this platform series. A second hovering AUV platform, the SeaBED AUV series, was developed in 2000 by WHOI [69].

The jointly military/commercial developed Hugin AUV was introduced at the start of the 1990s by Kongsberg Maritime [70]. In terms of AUV technology, this platform has logged the most hours and kilometres largely attributed to its endurance and seabed mapping capabilities. It was the first AUV to complete a fully commercial offshore operation in the fall of 1997 [71].

A summary of the significant AUV developments in the $20^{\text{th}}$ century is provided in Table 2.1. By the end of the millennium, the technology had matured sufficiently to the point where regular, repeatable deep water and harsh environment operations were possible [72]. The technology had turned a corner and taken large steps toward commercial acceptance [73]. Since 2000, academic researchers and commercial interests have pursued more sophisticated advancements with AUVs. This includes work with autonomy, multi-vehicle operations, sensor development, improved navigation and endurance as the technology is propelled into wider areas of application [22, 74].

### 2.1.2 AUV polar operations

The untethered and unmanned characteristics of AUV technology are particularly attractive for high risk under-ice scientific applications. The technology has been utilized to varying degrees of success in such similar harsh environments for several decades. Interestingly, the technology has been deployed in polar environments quite early in its overall development timeline. The earliest reported under-ice AUV work

| Decade | Platform | Developer | Country |
|---|---|---|---|
| 1960s | SPURVs, UARS | U. Washington - App. Physics Lab | United States |
| 1970s | EAVE East, EAVE West | U. New Hampshire: Marine Sys. Eng. Lab | United States |
| 1980s | EPAULARD | CNEXO/Ifremer | France |
| | ARCS | International Submarine Engineering | Canada |
| | SKAT-GEO, L2, MT-88 | Institute for Marine Technology Problems | Russia |
| | LSV-1 | Southwest Research Institute | United States |
| | AUSS | US Navy | United States |
| 1990s | PTEROA150 | U. of Tokyo | Japan |
| | Aqua Explorer 1000 | KDD Laboratories | Japan |
| | MARIUS | Marine Science and Technology Commiss. Europe | Denmark |
| | Autosub | Ins. of Oceans Sciences/National Oceanography Centre | United Kingdom |
| | Sea Squirt, Odyssey | Massachusetts Institute of Technology, Draper Lab | United States |
| | ABE, REMUS, SEABED | Woods Hole Oceanographic Institution | United States |
| | Theseus | International Submarine Engineering | Canada |
| | Hugin | Kongsberg | Norway |

Table 2.1: AUV platforms of the 20$^{\text{th}}$ century.

was undertaken with the Unmanned Arctic Research Vehicle or UARS AUV [29–31]. Since that time, records have been established with respect to depth: 4062 m [75] and endurance: 330 km [76]. Various entities such as NOC, ISE, and WHOI have established track records for under ice AUV operations and made valuable contributions in the area of practical considerations and operational challenges for under ice AUV deployments. Doble et al. [77] and McPhail et al. [15] provide a comprehensive history of under-ice AUV operations. These are the current benchmarks for AUV operations in polar environments.

The presence of an ice layer results in several ramifications that must be considered for under-ice operations [78]. The potential inability to access the surface affects both the mission-critical components such as fault response and can result in longer horizontal ranging and navigation requirements in the absence of shepherding capability. A fundamental consequence of the ice boundary layer is the significant effect on radio frequency and satellite-surface communications channels. There is a reliance upon longer range, low frequency acoustics for safe AUV operations and risk mitiga-

tion. Using long-baseline acoustics for a deepwater AUV seabed survey of a relatively small operating area is an approach that can be optimal in some situations [79].

High latitude operations can prove problematic for AUV navigation systems. The earth's magnetic field lines are near vertical, so compass-based heading estimates have limited reliability close to the poles. Inertial navigation systems north/south aligning ability is reduced as a function of the secant of latitude. These systems rely on sensing acceleration due to gravity and acceleration due to the earth's rotation and then resolving a heading solution from these measured accelerations [80, 81].

Despite the number of polar deployments with AUV technology, it is still an environment which demands significant effort and planning before the execution of operations [82, 83]. The underlying motivation for this work is to develop a system that is robust and practical in such extreme environments that lowers the overall risk of AUV operations.

## 2.2 Acoustic measurement systems

### 2.2.1 Standard systems

A good reference for acoustic position measurements that describes the mathematical basics of positioning and measurement errors can be found in [84]. Vickery discusses currently available acoustic systems and their respective strengths and weaknesses [85]. He describes some new system concepts that were in development at the turn of the millennium [86]. An AUV perspective for acoustic navigation using acoustic position systems is included in a general survey paper of AUV navigation [87]. The definitive reference for underwater acoustic positioning systems was written by Milne [88]. The author identifies a list of the different underwater positioning fixing or tracking methods, captured in Table 2.2. This table, compiled from the work

of previous researchers, contains tracking technologies suitable for underwater vehicle tracking applications. This table is several decades old, but it still captures the different technological configurations possible for acoustic underwater positioning. Underwater positioning systems (5)-(8) are singled out as being better suited for submersible applications [88]. Generally it is recognized that receiver directionality as a means of tracking can be problematic in terms of accuracy in the absence of ranging information and the nature of underwater sound transmission. Gains in computational capacity with respect to power and space have resulted in sonar being used for positioning of AUVs. This technology is not quite aligned with the motivation for this particular work because of the limited range of sonar. An overview of the basics of acoustic tracking technology with respect to the baseline length used is appropriate to give context for the proposed approach of this thesis.

| | Description | Mode of operation |
|---|---|---|
| (1) | Surface ship using a directional hydrophone | bearing - bearing |
| (2) | Submersible using a directional hydrophone | bearing - bearing |
| (3) | Surface ship using a scanning sonar | range - bearing |
| (4) | Submersible using a scanning sonar | range - bearing or range - range |
| (5) | Surface ship using a short baseline system | bearing - bearing or range - bearing |
| (6) | Surface ship using an ultra short baseline system | range - bearing |
| (7) | Surface ship using a long baseline system | range - range |
| (8) | Submersible using a long baseline system | range - range |
| (9) | Surface ship using hyperbolic system | phase difference |
| (10) | Submersible using hyperbolic system | phase difference |

Table 2.2: Surface and submersible acoustic tracking technologies.

### 2.2.2 Short baseline system

The theoretical underpinnings of short baseline systems are described. Such a system tends only to be deployed from larger platforms (ships) and is of limited use in submersible technologies. However, it is included here for completeness and it is the simplest manifestation from a theoretical vantage point.

The system is composed of a source and multiple receivers. It utilizes differences in the received signal time of arrival (TOA) to determine a bearing to the source. The source can either be a transponder or a beacon that is placed at a *known* depth. System functionality depends on the nature of the source, i.e. beacon or transponder. The source will also determine whether the receivers are hydrophones or transponders. The receiving system requires a minimum of three receivers that are spaced approximately 5 m to 20 m apart. Additional receivers can be employed to provide redundancy that will improve system performance and be necessary if there is a receiver dropout or malfunction.

There are advantages and disadvantages with either beacon or the transponder based short baseline systems. Some of the stronger points of the transponder based systems [89] include:

1. The source transponders will only transmit when queried. This power conservation will improve source endurance compared to a free running beacon source;

2. Transponders provide range directly between the source transponder and vessel transponders; therefore, it is possible to derive a three dimensional solution without relying on the known depth assumption as is the case with the beacon based system;

3. Transponder broadcasts can be controlled with the resulting ability to optimize position estimation with mission requirements and ability to synchronize or

schedule interrogations;

4. Controllable interrogations can minimize multipath effects and false data which results in improved data quality;

5. If there is redundancy in the system both with the receiving and source nodes, then it is possible to maintain the fidelity of the acoustic signal path if the system is deployed in an area where physical obstructions or localized acoustic interference may exist.

Depending on the application, the beacon-based system has certain advantages. Transponder systems rely on signal transmission in two directions whereas the beacon system only requires signal transmission in one direction. If there are environmental conditions that degrade acoustic performance, then halving the distance for signal transmission increases the likelihood of successful signal transfer.

Figure 2.1 presents the general three receiver SBL configuration in the horizontal $xy$-plane and in a vertical cross section. There is no redundancy with this system layout. The general configuration for the SBL system is the same regardless of whether a beacon or transponder is employed as the source. The beacon based system will be described below, followed by detail on the transponder based system.

The mathematics underlying the basic case for derivation of a position solution relative to a known seafloor mounted source will be described. For this base case, the receivers of the SBL system will be positioned such that the baselines are orthogonal, this differs slightly from the general arrangement as shown in Figure 2.1(a). The relative TOA for the acoustic signal at different receivers provides sufficient information to estimate the position of the source.

Consider the acoustic signal emanating from the source. The pressure wave associated with the signal can be considered a plane wave when it arrives at the

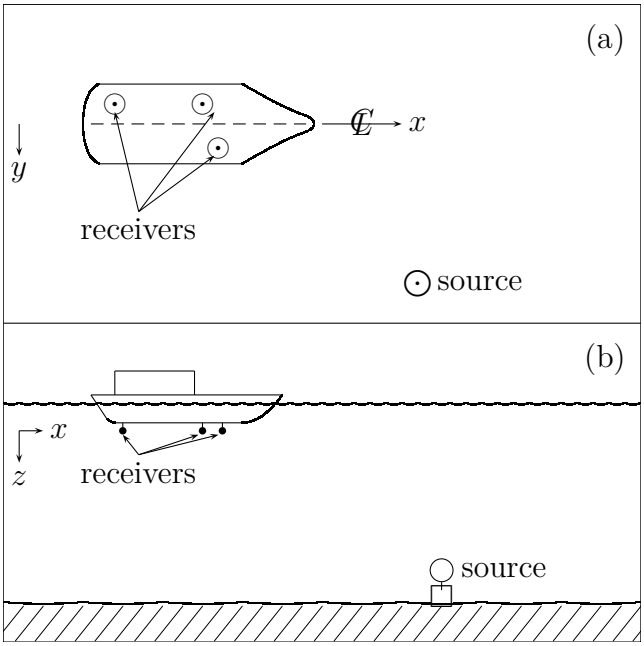


Figure 2.1: Top view (a) and side view (b) of SBL - source configuration.

receivers installed on the ship. Generally, there is a difference in the TOA of the wave at two receivers. This TOA difference determines a bearing of the source relative to the baseline of the two receivers.

Define $D_{12}$ to be the distance between two receiving nodes on a vessel as shown in Figure 2.2. The TOA for the signal at the first receiver relative to the second receiver is $\Delta t_{12}$. For a given sound velocity, $v$, the TOA determines a distance $v\Delta t_{12}$ which in turn defines an angle of arrival or bearing angle to the source in the plane defined by the two receivers and the source by

$$\phi = \cos^{-1}\left(\frac{v\Delta t_{12}}{D_{12}}\right).$$

This angle, $\phi$, from the horizontal defines a vertical angle $\theta$ from the centre of the baseline $\theta = 90 - \phi$. The angle $\theta$ can be used along with the known depth of the source, $Z$, to calculate a horizontal perpendicular distance from the projection of the

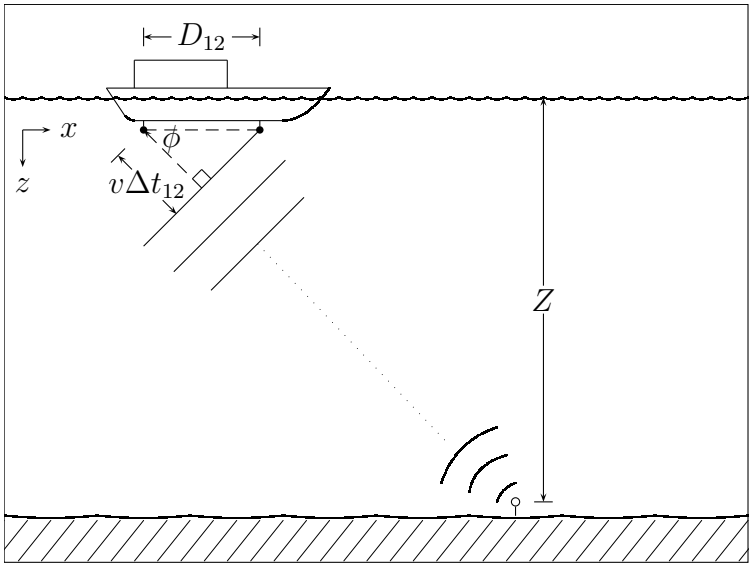


Figure 2.2: Acoustic pressure wave emanating from source to SBL receiving array.

midpoint of the baseline onto the sea bed in the direction of the baseline to the source position.

The receivers are suspended from beneath the vessel at the points $R_1, R_2$ and $R_3$ as depicted in Figure 2.3. The point $R_{12}$ is the midpoint of the baseline formed by $R_1$ and $R_2$ and $R_{13}$ is the midpoint of the baseline formed by $R_1$ and $R_3$. The points $P_{12}$ and $P_{13}$ are the orthogonal projections of the midpoints $R_{12}$ and $R_{13}$ onto the sea floor. Then the location of the source at $P$ can be determined from

$$\begin{aligned} X &= Z \tan\theta_x, \text{ and} \\ Y &= Z \tan\theta_y, \end{aligned}$$

where $X$ is the distance in the $R_1R_2$ baseline direction (taken as the $x$-axis in the diagram above) from $P_{12}$ and $Y$ is the distance in the $R_1R_3$ baseline direction (taken as parallel to the $y$-axis in the diagram above) from $P_{13}$. If the hardware configuration for the short baseline system employs transponders instead of a beacon - hydrophone

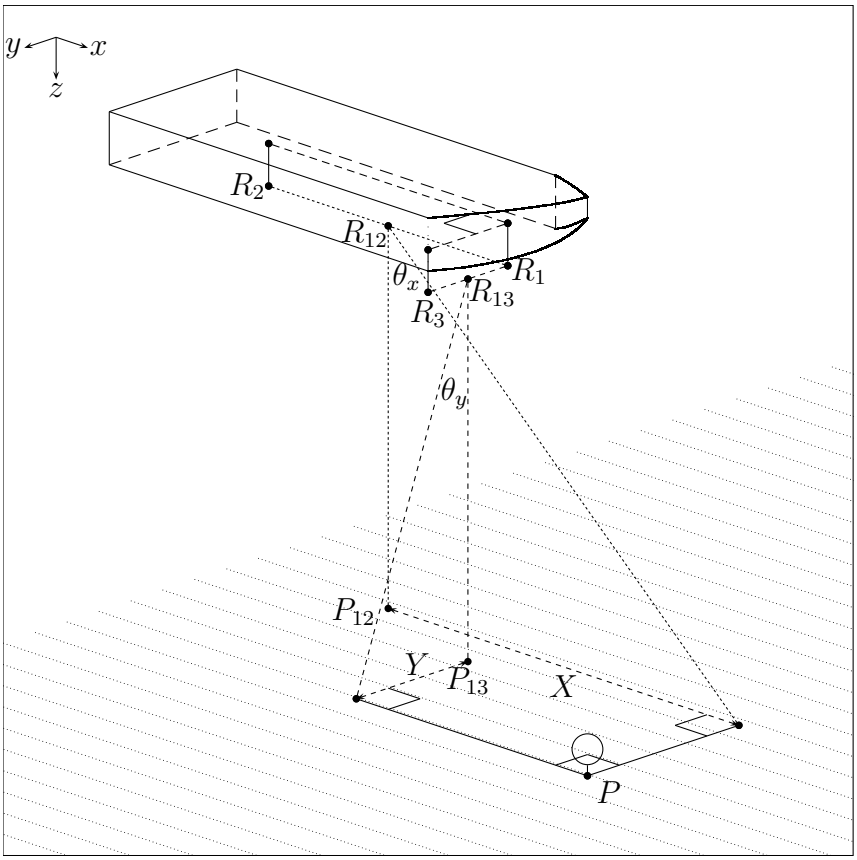


Figure 2.3: Beacon based SBL receiver - source geometry.

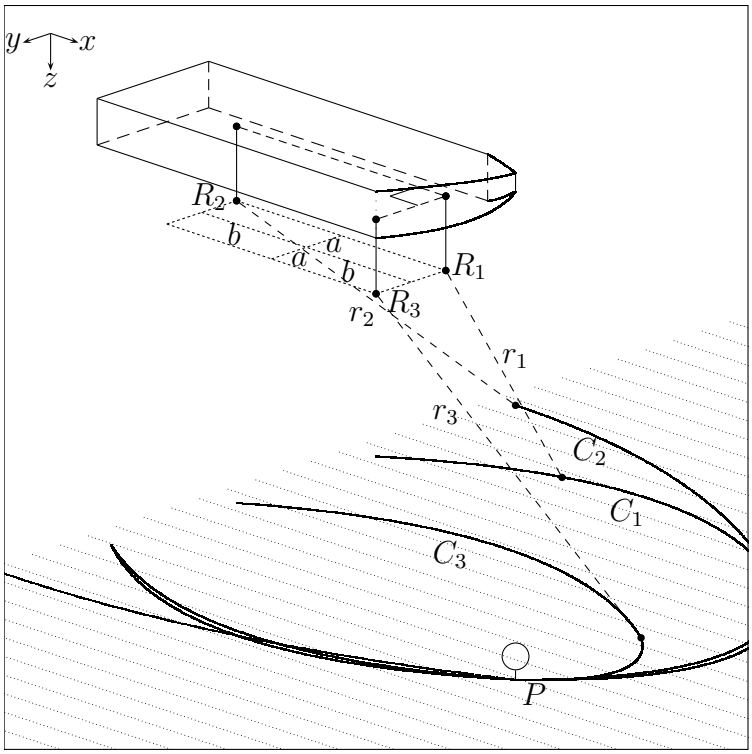


Figure 2.4: Transponder based SBL receiver - source geometry.

system then the mathematics will differ. A transponder measures round trip travel time for an acoustic signal between nodes from which it calculates the range or the TOA. In a SBL system, three range measurements taken at different locations are sufficient to determine a 3-dimensional positional estimate for the source transponder. The geometrical problem for the transponder-based configuration is the intersection of three spheres. The beacon-based system relies on bearing estimation determined by the signal time difference of arrival (TDOA). Figure 2.4 depicts the transponder-based geometry for the localization problem.

A range $r_i$ is measured for each node $R_i$. Let the centre of the coordinate system be the centre of the plane in which the ship based array is located. The three spheres defined by the transponder ranges

$$(x+b)^2 + (y-a)^2 + z^2 = r_1^2; \tag{2.1}$$

$$(x+b)^2 + (y+a)^2 + z^2 = r_2^2; \tag{2.2}$$

$$(x-b)^2 + (y-a)^2 + z^2 = r_3^2. \tag{2.3}$$

Consider the difference of Equation (2.1) and Equation (2.2)

$$(y-a)^2 - (y+a)^2 = r_1^2 - r_2^2.$$

This reduces to

$$y = \frac{r_2^2 - r_1^2}{4a}.$$

Similarly, the difference of Equation (2.1) and Equation (2.3)

$$(x+b)^2 - (x-b)^2 = r_1^2 - r_3^2,$$

yields a distinct solution for $x$

$$x = \frac{r_1^2 - r_3^2}{4b}.$$

The solution for $z$ can be determined by substituting $x$ and $y$ into one of the original equations

$$z = \pm\sqrt{r_1^2 - \left(\frac{r_1^2 - r_3^2 + 4b^2}{4b}\right)^2 + \left(\frac{r_2^2 - r_1^2 + 4a^2}{4a}\right)^2}.$$

Note that the negative solution can be excluded by the choice of coordinate system and the practicality of the application. It is limited to the half space, i.e. the source is located beneath the plane containing the receiving array.

### 2.2.3 Ultra short baseline system

An ultra short baseline system (USBL), sometimes referred to as a super short baseline system, utilizes range and bearing to determine the position of the source. It differs from the short baseline system in that it utilizes the phase difference of a received signal of closely spaced receivers to derive a bearing to the source. This bearing when coupled with range and/or depth information yields a location solution. Similar to a SBL, a USBL can use different technologies for the source. When the source is a beacon, a known depth is required to derive a solution. While a transponder requires no additional spatial measurements. If depth information is available to supplement a transponder, then measurement error is reduced and accuracy is improved [88].

The typical USBL system consists of a small array (3 to 4 elements) physically encased in a single transducer or as exposed single receiving elements. The spacing on the multiple receivers is typically between 200 mm to 300 mm. A strength of the technology is its deployment versatility. Generally, it can be deployed over the side of most vessels of opportunity compared to an installed and surveyed SBL.

It is possible to derive a bearing angle, $\theta$ to the source based on acoustic signal

phase difference at distinct elements. Consider Figure 2.5 where $f$ is the acoustic signal frequency, $\Phi$ is the phase difference, $\phi$ is the acoustic signal incidence arrival angle, $v$ is the velocity of sound in water and $d$ is the baseline distance between two receiving elements $R_1$ and $R_2$.

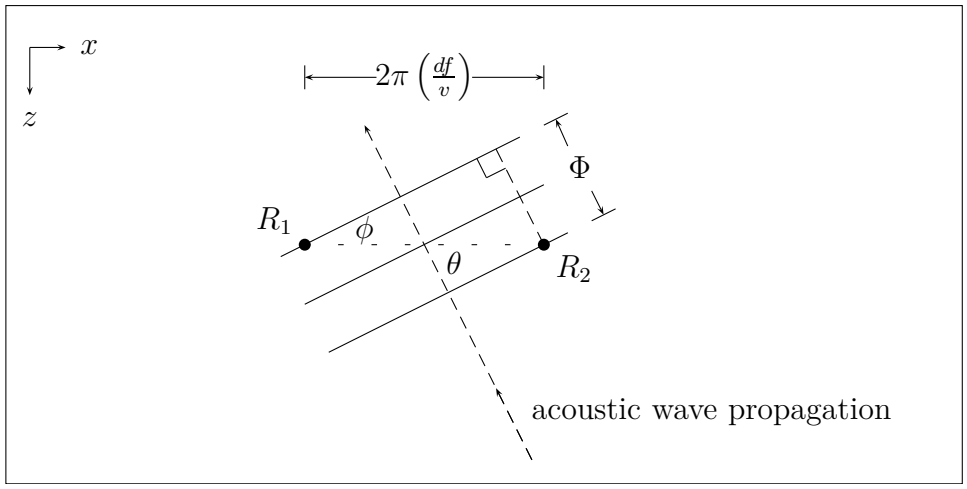


Figure 2.5: Phase difference geometry between two USBL elements.

The acoustic pressure wave can be treated as a planar wave due to spreading of the wave emanating from the source and the significant distance between the source and the receivers relative to the spacing of the receiver nodes. The receiver spacing can be expressed in terms of phase for the given frequency, $f$, as in Figure 2.5:

$$2\pi\left(\frac{df}{v}\right) = 2\pi\left(\frac{d}{\lambda}\right).$$

The angle $\phi$ can be calculated from the ratio of the measured phase difference and the distance expressed in radians

$$\sin\phi = \frac{\Phi}{2\pi\left(\frac{df}{v}\right)}.$$

Using the vertically opposite angle substitution of $90-\phi = \theta$ and a cofunction identity

yields the equation

$$\cos\theta = \frac{\Phi}{2\pi\left(\frac{df}{v}\right)}.$$

Then the angle of arrival relative to the baseline is given by

$$\theta = \cos^{-1}\left(\frac{v\Phi}{2\pi df}\right).$$

The mechanical angle of incidence, $\theta$, derived from the phase difference between two

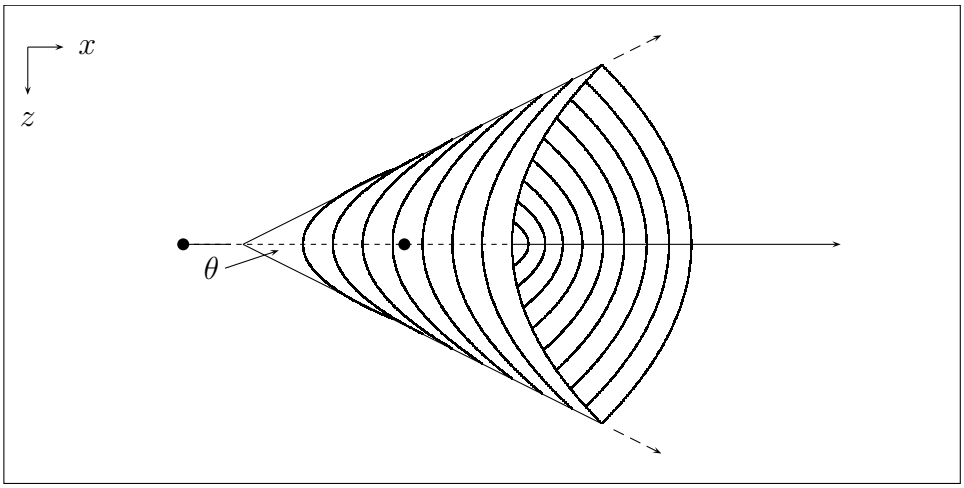


Figure 2.6: Cone created by signal angle of arrival between two USBL elements.

receiving elements defines a cone in three dimensional space as depicted in Figure 2.6. Two lines result from the intersection with another distinct cone that arises from another baseline in the USBL array. However, one line can be rejected because of the constraints of the practical problem, i.e. it is possible to isolate the source in the hemisphere of interest [90]. Therefore, a known depth or range will yield a solution in three space for the location of the source.

The three dimensional configuration is depicted for both cases of known range $r$ or depth $h$ in Figure 2.7(a) and Figure 2.7(b) respectively. The method for determining the source location $(x, y, z)$ will be explained for both cases separately. In Figure

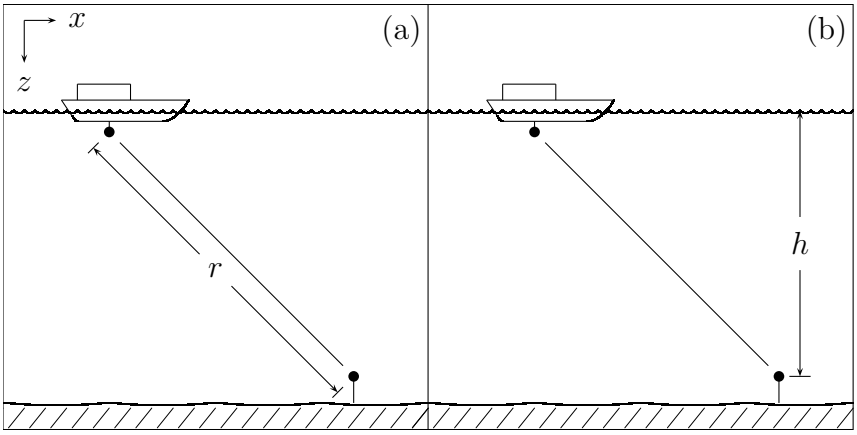


Figure 2.7: Two USBL configurations: (a) known range $r$ and (b) known depth $h$.

2.8, the given information is $\theta_x$, $\theta_y$ and either one or both $r$ and $h$.

Consider the first case when the range $r$ to the source is known in Figure 2.8. The horizontal coordinates for the source position can be calculated directly from the arrival angles and the range to the source

$$\begin{aligned} x &= r\cos\theta_x; \\ y &= r\cos\theta_y. \end{aligned}$$

The depth of the source is determined using the Pythagorean equation in three dimensional space and making the appropriate substitutions

$$\begin{aligned} r^2 &= x^2 + y^2 + z^2 \\ z^2 &= r^2 - x^2 - y^2 \\ z^2 &= r^2 - r^2\cos^2\theta_x - r^2\cos^2\theta_y \\ z &= r\sqrt{1 - \cos^2\theta_x - \cos^2\theta_y}. \end{aligned}$$

So the position of the source when a transponder based USBL is employed is given

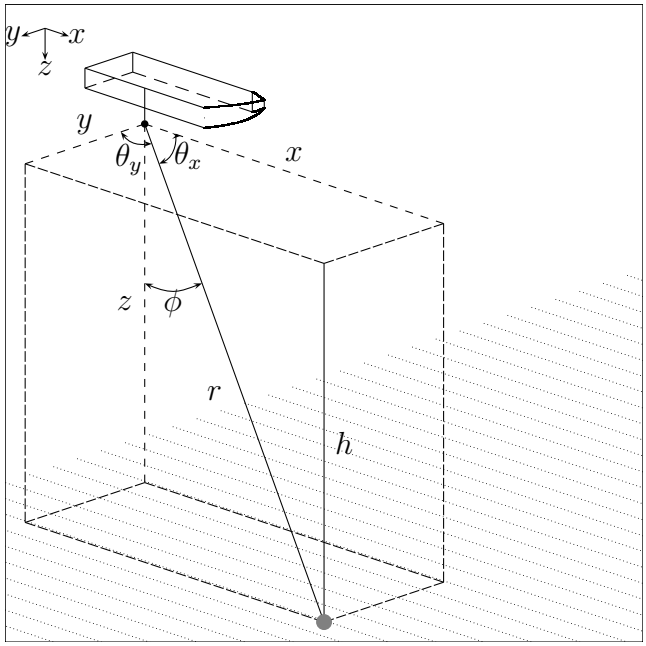


Figure 2.8: USBL system geometry.

by

$$(x, y, z) = \left( r \cos\theta_x, r \cos\theta_y, r\sqrt{1 - \cos^2\theta_x - \cos^2\theta_y} \right).$$

The second case configuration is when a beacon is employed for the USBL source and it is deployed at a known depth $h$. It can be seen from Figure 2.8 that

$$h = r \cos\phi,$$

where $\phi$ is the unknown bearing angle to the source from the vertical. It can be shown

using the Pythagorean equation and substituting for $x$ and $y$

$$\begin{aligned} r^2 &= x^2 + y^2 + h^2 \\ h^2 &= r^2 - x^2 - y^2 \\ r^2 \cos^2 \phi &= r^2 - r^2 \cos^2 \theta_x - r^2 \cos^2 \theta_y \\ \cos \phi &= \pm \sqrt{1 - \cos^2 \theta_x - \cos^2 \theta_y}. \end{aligned}$$

It is possible to determine explicit solutions for $x$ and $y$

$$\begin{aligned} x &= r \cos \theta_x = \left(\tfrac{h}{\cos \phi}\right) \cos \theta_x = \tfrac{h \cos \theta_x}{\sqrt{1 - \cos^2 \theta_x - \cos^2 \theta_y}}, \\ y &= r \cos \theta_y = \left(\tfrac{h}{\cos \phi}\right) \cos \theta_y = \tfrac{h \cos \theta_y}{\sqrt{1 - \cos^2 \theta_x - \cos^2 \theta_y}}. \end{aligned}$$

Then the position source $(x, y, z)$ for a beacon-based USBL is

$$(x, y, z) = \left( \frac{h \cos \theta_x}{\sqrt{1 - \cos^2 \theta_x - \cos^2 \theta_y}}, \frac{h \cos \theta_y}{\sqrt{1 - \cos^2 \theta_x - \cos^2 \theta_y}}, h \right).$$

If both the range and the depth of the source are known then the overall accuracy of the USBL is increased.

### 2.2.4 Long baseline system

A long baseline system (LBL) utilizes range to determine a position solution for a source spatially located within a multi-node network. The general configuration is similar to a SBL system, i.e. a source coupled with multiple receivers. However, the distance between receivers is significantly larger and is approximately at the kilometre scale or hundreds of metres and the stationary receiver locations are established to a high degree of accuracy. Receivers are typically oriented such that they form the

vertices of a regular polygon and the source operates within the operational area defined by this polygon. Generally, the position solution for the source is derived using TOA and spherical tracking techniques in a transponder based network. If free running beacons are utilized in lieu of transponders, then it is not possible to measure directly the signal time of flight between the source and a network node. In this case, where the ping emission time is unknown, a method of hyperbolic tracking is used [84, 87, 91].

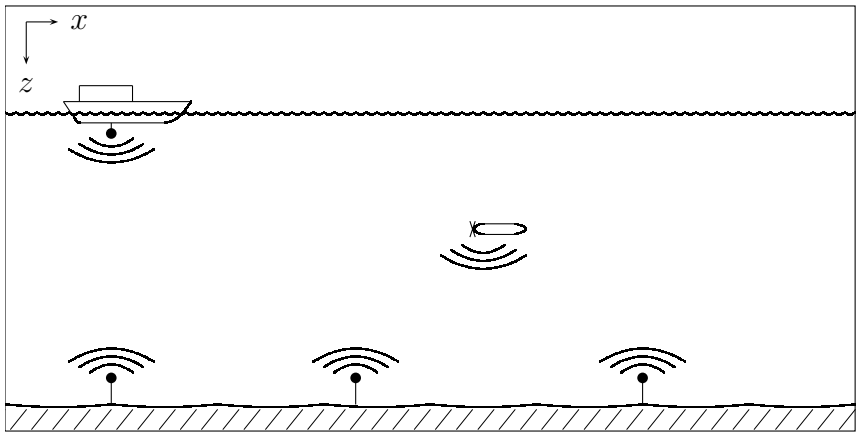


Figure 2.9: Side view of LBL general configuration.

In terms of operation, the baseline is deployed to fixed positions on the seabed. The baseline nodes are then surveyed in to the network. Milne [88] describes the approaches and techniques for the survey process. It is essential that depth and horizontal position for each node are known as accurately as possible in order to generate a good position fix for the source. A least squares approach is commonly used to determine precise node positions for LBL network calibration [88]. A side view of a general configuration for a LBL system is shown in Figure 2.9. Note that the three nodes would not be deployed in an actual co-linear arrangement as may be interpreted by this figure, but rather in a triangular configuration.

An additional level of complexity exists with regards to communication protocol

within the LBL network to establish position of the asset of interest, the AUV in this case. There are multiple configurations that can be employed [85]. In a transponder based LBL network, the AUV can derive its position directly using spherical methods by interrogating all networks nodes simultaneously or one at a time. In the former case, the responses from the network nodes must be distinguishable from one another so that the individual nodes with their known locations can be identified. In this scenario, the AUV position still must be communicated to the surface if external tracking and supervision requirements need to be satisfied.

An alternative method not reliant upon modem communication to relay the AUV position requires the supervising vessel to interrogate the AUV and the AUV act as a relay to interrogate the network. The known ship position coupled with known LBL node positions makes it possible to derive the AUV position from the set of individual LBL node responses [85]. A free running beacon that is synchronized with the supervising vessel can also be utilized to interrogate the network and make localization of the AUV possible using the LBL node responses.

These previous scenarios all use spherical tracking methods for derivation of the AUV position. If the LBL network consists of free running beacons then hyperbolic tracking is employed.

#### 2.2.4.1 Spherical positioning

The basic technique to derive a position estimate within a transponder based LBL network is to use the acoustic signal time of flight or TOA to determine the distance from an individual node to an AUV. Each distance defines a sphere about a LBL node. Figure 2.10 depicts a planar slice of the spheres (circles) intersecting at the AUV position. Let $(x, y, z)$ be the unknown AUV position and $(x_i, y_i, z_i)$ be the known position for each LBL node, $N_i$. For a range, $r_i$ between each node and the

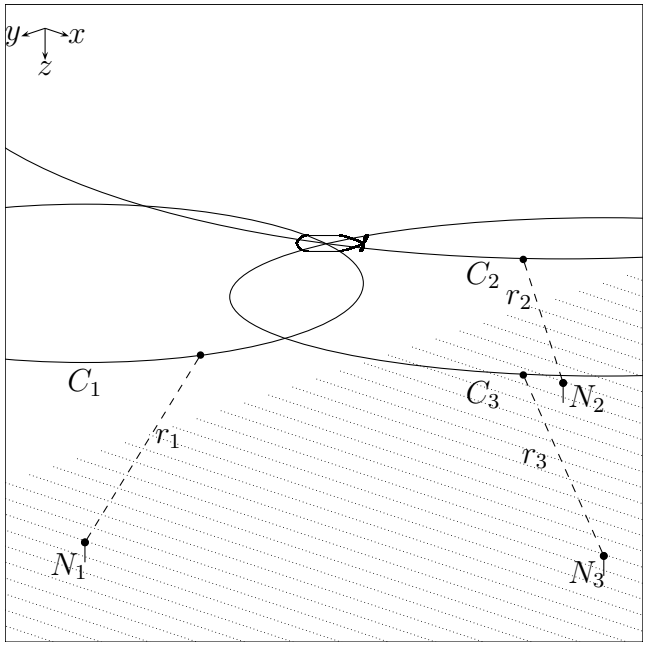


Figure 2.10: LBL spherical geometry.

AUV the set of equations used to determine the AUV location is

$$(x - x_1)^2 + (y - y_1)^2 + (z - z_1)^2 = r_1^2;$$

$$(x - x_2)^2 + (y - y_2)^2 + (z - z_2)^2 = r_2^2;$$

$$(x - x_3)^2 + (y - y_3)^2 + (z - z_3)^2 = r_3^2.$$

The system can be expressed linearly

$$x(x_1 - x_3) + y(y_1 - y_3) - 2z(z_1 - z_3) = \tfrac{r_3^2 - r_1^2}{2};$$

$$x(x_1 - x_2) + y(y_1 - y_2) - 2z(z_1 - z_2) = \tfrac{r_2^2 - r_1^2}{2};$$

$$x(x_2 - x_3) + y(y_2 - y_3) - 2z(z_2 - z_3) = \tfrac{r_3^2 - r_2^2}{2}.$$

Then it can be expressed in matrix form $A\mathbf{x} = R$

$$\begin{bmatrix} X_{13} & Y_{13} & Z_{13} \\ X_{12} & Y_{12} & Z_{12} \\ X_{23} & Y_{23} & Z_{23} \end{bmatrix} \begin{bmatrix} x \\ y \\ z \end{bmatrix} = \begin{bmatrix} R_{31} \\ R_{21} \\ R_{32} \end{bmatrix},$$

where $X_{ij} = (x_i - x_j)$, $Y_{ij} = (y_i - y_j)$, $Z_{ij} = (z_i - z_j)$ and $R_{ij} = \frac{1}{2}(r_i^2 - r_j^2)$. The general solution can be derived explicitly by determining $A^{-1}R$

$$\begin{bmatrix} x \\ y \\ z \end{bmatrix} = \frac{1}{det(A)} \begin{bmatrix} (Y_{12}Z_{23} - Y_{23}Z_{12}) + (Y_{23}Z_{13} - Y_{13}Z_{23}) + (Y_{13}Z_{12} - Y_{12}Z_{13}) \\ (X_{23}Z_{12} - X_{12}Z_{23}) + (X_{13}Z_{23} - X_{23}Z_{13}) + (X_{12}Z_{13} - X_{13}Z_{12}) \\ (X_{12}Y_{23} - X_{23}Y_{12}) + (X_{23}Y_{13} - X_{13}Y_{23}) + (X_{13}Y_{12} - X_{12}Y_{13}) \end{bmatrix} \begin{bmatrix} R_{31} \\ R_{21} \\ R_{32} \end{bmatrix}$$

where

$$det(A) = X_{13}(Y_{12}Z_{23} - Y_{23}Z_{12}) - Y_{13}(X_{12}Z_{23} - X_{23}Z_{12}) + Z_{13}(X_{12}Y_{23} - X_{23}Y_{12})$$

and $det(A) \neq 0$.

#### 2.2.4.2 Hyperbolic positioning

Hyperbolic positioning is employed when the acoustic emission time is unknown from known beacon locations. Unlike TOA, hyperbolic position relies on TDOA to establish a set hyperbolic curves whose intersection is the target location as shown in Figure 2.11. There is no master clock providing synchronized operation between the beacon sources and the receivers. TDOA techniques have been used for localization of ship and air assets using low frequency radio signals. Examples of such systems include LORAN-C, Decca Navigator and Omega Navigation System. The satellite based Global Positioning System (GPS) has replaced radio based technology in most cases.

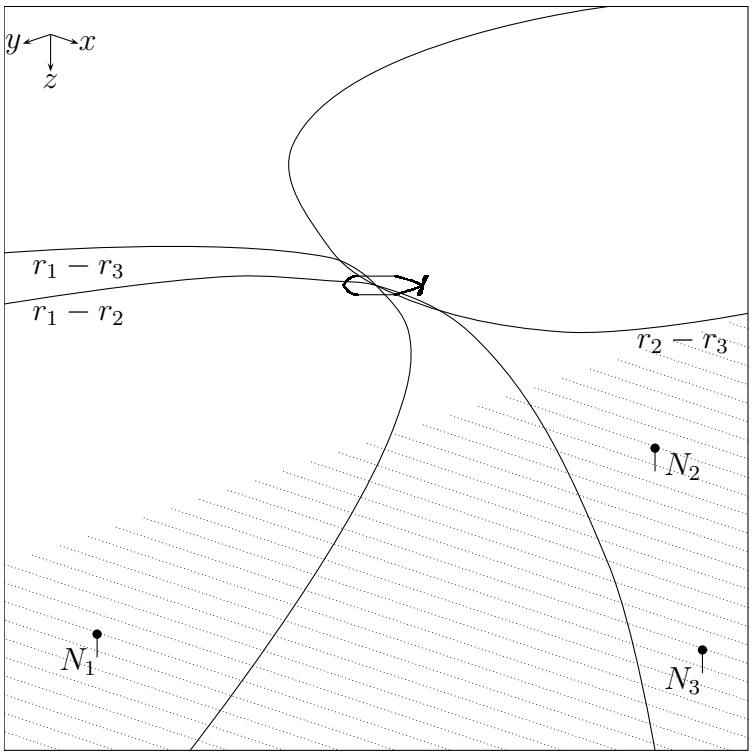


Figure 2.11: LBL hyperbolic geometry.

The principles of underwater acoustic based hyperbolic tracking are similar to the radio frequency (RF) applications. Given an unknown range $r_i$ between the unknown AUV position $(x, y, z)$ and the known node location $(x_i, y_i, z_i)$ for each $N_i$ within a 3 element LBL network, the difference in TOA between signals from the

respective nodes determines a set of distances $R_{ij}$ can be determined

$$\begin{aligned}
R_{31} &= r_3 - r_1 \\
&= \sqrt{(x_3-x)^2+(y_3-y)^2+(z_3-z)^2} - \sqrt{(x_1-x)^2+(y_1-y)^2+(z_1-z)^2} \\
R_{32} &= r_3 - r_2 \\
&= \sqrt{(x_3-x)^2+(y_3-y)^2+(z_3-z)^2} - \sqrt{(x_2-x)^2+(y_2-y)^2+(z_2-z)^2} \\
R_{21} &= r_2 - r_1 \\
&= \sqrt{(x_2-x)^2+(y_2-y)^2+(z_2-z)^2} - \sqrt{(x_1-x)^2+(y_1-y)^2+(z_1-z)^2}
\end{aligned} \tag{2.4}$$

Solving this system explicitly for $(x, y, z)$ is an involved process. It can be shown in the two dimensional variation of this problem in the horizontal plane, (i.e. $z$ known) that the set of possible solutions of $(xy)$ is a hyperbola. Set $R_{31} = R$:

$$R = \sqrt{(x_3-x)^2+(y_3-y)^2} - \sqrt{(x_1-x)^2+(y_1-y)^2}. \tag{2.5}$$

Algebraic manipulation of the first equation then yields

$$R^2 + 2R\sqrt{(x_1-x)^2+(y_1-y)^2} + (x_1-x)^2 + (y_1-y)^2 = (x_3-x)^2 + (y_3-y)^2$$

$$R^2 + 2R\sqrt{(x_1-x)^2+(y_1-y)^2} + x_1^2 - 2x_1x + y_1^2 - 2y_1x = x_3^2 - 2x_3x + y_3^2 - 2y_3y$$

$$4R^2\left((x-x_1)^2+(y-y_1)^2\right) = \left(2(x_1-x_3)x + 2(y_1-y_3)y + x_3^2 - x_1^2 + y_3^2 - y_1^2 - R^2\right)^2.$$

This can be expressed in the conic form $Ax^2 + Bxy + Cy^2 + Dx + Ey + F = 0$,

$$\begin{aligned}
&[4R^2 - 4(x_1 - x_3)^2]\, x^2 + [8(x_1 - x_3)(y_1 - y_3)]\, xy + [4R^2 - 4(y_1 - y_3)^2]\, y^2 \\
&- [8R^2 x_1 + 4(x_1 - x_3)(x_3^2 - x_1^2 + y_3^2 - y_1^2 - R^2)]\, x \\
&- [8R^2 y_1 + 4(y_1 - y_3)(x_3^2 - x_1^2 + y_3^2 - y_1^2 - R^2)]\, y \\
&- [(x_3^2 - x_1^2 + y_3^2 - y_1^2 - R^2)^2 - 4R_{31}^2(x_1^2 + y_1^2)] = 0.
\end{aligned}$$

Now

$$R = \sqrt{(x_3 - x)^2 + (y_3 - y)^2} - \sqrt{(x_1 - x)^2 + (y_1 - y)^2} \leq \sqrt{(x_3 - x_1)^2 + (y_3 - y_1)^2}.$$

The geometric support for this claim can be seen in Figure 2.12. Without loss of generality assume that $r_3 > r_1$. Draw a circle centered at $N_3 = (x_3, y_3)$ with radius $r_0 = \sqrt{(x_3 - x_1)^2 + (y_3 - y_1)^2}$. Then it is not possible to find a point $(x, y)$ such that a circle of radius $r_1$ and centered at $(x, y)$ can be drawn with $R > r_0$. It is only when $(x, y)$ is co-linear with $N_1$ and $N_2$ that $R = r_0$ otherwise $R < r_0$.

Next, consider the discriminant $B^2 - 4AC$ and that $R$ is bounded above by

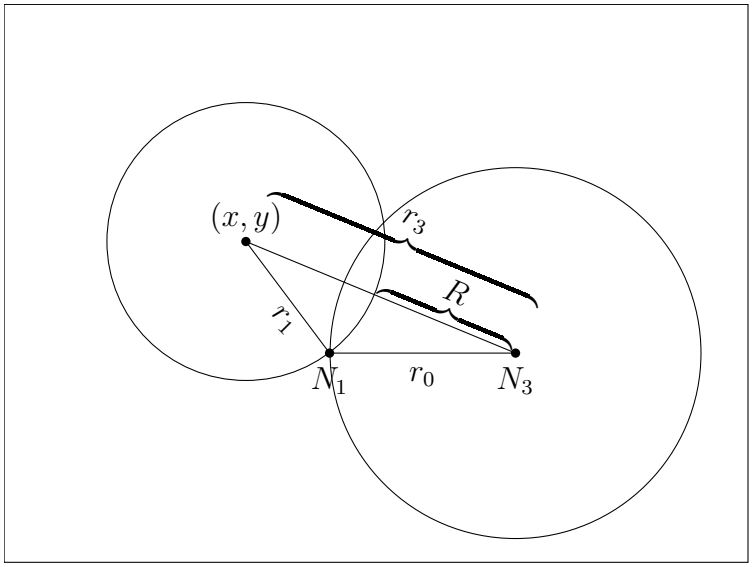


Figure 2.12: Geometric argument for $R \leq r_0$.

$r_0 = \sqrt{(x_3 - x_1)^2 + (y_3 - y_1)^2}$. Then

$$\begin{aligned}
& 4AC \\
= \;& 4\left[4R^2 - 4(x_1 - x_3)^2\right]\left[4R^2 - 4(y_1 - y_3)^2\right] \\
\leq \;& 4\left[4((x_3 - x_1)^2 + (y_3 - y_1)^2 - 4)(y_1 - y_3)^2)\right]\left[4(x_1 - x_3)^2)\right] \\
\leq \;& 4\left[4(y_1 - y_3)^2)\right]\left[4(x_1 - x_3)^2)\right] \\
= \;& \left[8(x_3 - x_1)(y_3 - y_1)\right]^2 \\
= \;& B^2.
\end{aligned}$$

Hence $B^2 - 4AC \leq 0$ and the solution to Equation 2.5 is a hyperbola whenever $R < \sqrt{(x_3 - x_1)^2 + (y_3 - y_1)^2}$ and parabola for the trivial case with $(x, y) = (x_1, y_1)$, i.e. $R = \sqrt{(x_3 - x_1)^2 + (y_3 - y_1)^2}$.

The solution $(x, y, z)$ for the system of equations 2.4 is the intersection of three hyperboloids. A complete derivation of the general solution in the context of mobile

networks can be found in [92].

### 2.2.5 Other localization systems

#### 2.2.5.1 Single transponder/node approaches

There has been research using single beacon and transponder based systems. Early work in this area used least squares to estimate AUV positioning using range data from only one transponder in a long baseline system [93]. Comparable single beacon LBL-like systems have been studied in the context of navigation. A thorough review of the directly related literature to single beacon navigation can be found in [94]. There has been previous research done in this area [93, 95–103]. These works utilize ranging to a known beacon location from an AUV to derive navigational information for the vehicle. A primary difference between these efforts and the application for the SBSH based Emergency Localization System (ELS) is that the beacon position is unknown and range information cannot be measured directly because there is no synchronization between transmitting and receiving systems. Other more recent research based on single beacon technology and navigation use transponders [104] or time synchronized beacons [105–110].

A transponder based effort to localize a deep diving AUV from a surface ship is somewhat related to this ELS research. The mission configuration is comparable in that there is an effort to determine the AUV's position remotely from a surface ship [111].

#### 2.2.5.2 Acoustic fish/mammal detection

Acoustics have been used to track fish and marine mammals in an unrestrained manner to monitor the behavior of the species since 1956 [112]. In some instances, the sound

source is the vocalizations of the target species to be tracked [113] and in other instances a species may be acoustically tagged [114–116]. Over the decades tagging has evolved into an acceptable technique to monitor fish and is now being studied in terms of its performance [117].

Passive acoustic detection often utilizes hyperbolic methods and least squares approaches to determine location of the target species [113, 118, 119]. Alternative to hyperbolic tracking techniques, a model-based localization approach utilizes underwater sound propagation characteristics to predict source localization [120, 121]. The significant acoustic environment variation under ice would potentially hinder the application of a model-based technique for AUV localization.

## 2.3 Weakness of current technologies

Generally, LBL and USBL systems provide localization capability for AUV tracking and mission supervision. Such systems have their advantages and disadvantages as previously discussed.

The accuracy of LBL system can be on a centimetre scale. However, it can be time consuming and hence expensive to deploy such systems. Multiple nodes must be deployed to fixed positions on the seabed through a survey. Substantial time and effort are required for survey and placement of such systems because each node position must be known in order to determine a solution for the AUV position. The process of surveying in the LBL nodes into the network is involved and typically the system is laid out such that the asset being tracked operates within the LBL node network in a physical sense. The nodes themselves may not be recoverable. Variants on LBLs have been used such as GPS intelligent buoys composed of a network of buoys equipped with Differential GPS and hydrophones that receive a synchronized acoustical signal

from the target to be tracked [122]. Spherical tracking is used in this case. Some newer LBL systems are self-calibrating. The LBL approach has identified shortcomings at the fringes of a beacon network, specifically when hyperbolic positioning methods are employed as opposed to spherical methods [91]. In general, deploying an LBL network to address emergency AUV localization is not feasible due to an unknown source location which may be well outside the LBL network. Additionally, there is an increased cost (time and resources) associated with deploying LBL nodes through ice versus deploying a much smaller, single hydrophone.

A USBL system is easier to deploy, but these systems can be quite expensive and their performance in certain environments, such as under ice and horizontal mission configurations reduces their reliability [123]. Generally, a system calibration is required, although it is not as extensive as with LBL. Other acoustic systems that provide some ranging capability are transponders. The round trip time of travel for the signal is measured for which the range to the asset can be determined. In certain conditions, achieving a successful one-way signal transfer can be very difficult, let alone a two-way signal transfer required for USBL. This research is focused on a technique to locate a subsea asset or AUV using only one-way signal transfer to minimize the energy and mass cost to the AUV.

There are alternative systems available that provide AUV location capabilities including modems and transponders. These devices can be less complex to operate and deploy with an AUV when compared to baseline systems, but the mass and size of the components requiring integration can be a deterrent to their usage. They both require two-way communications and in the case of a modem, a high degree of channel fidelity is necessary for successful data interpretation. The acoustic signal propagation channel in a polar environment is characterized by challenges such as upward refraction, significant multipath, fading and blocking [32, 124].

A smaller system in terms of cost and size is a simple beacon-hydrophone system. A free running beacon (pinger) can be integrated into the AUV and provided it has a consistent ping rate, the AUV position can be determined based on observations of the propagation time delay for the acoustic signal at different points in space. The research and data collection employs ship-based and through-ice deployed hydrophone.

The challenge is to derive meaningful information for an AUV location as optimally as possible by using a minimal number of data points. Under certain conditions, an AUV location can be ascertained with only three or four measurements. If the conditions applied are less rigorous, more realistic and a specific AUV location cannot be obtained outright, an optimal search method should be developed to increase the likelihood of recovery.

Once tested and validated, the ELS can be used to mitigate an AUV loss. Its value will be most appreciated for AUV operations under-ice and AUV shallow water/coastal operations where acoustic signal multipath is a common problem. Typically, the current commercial acoustic range meters and USBL systems fail to function reliably in these latter environments. A robust, single beacon, single hydrophone ELS is has the potential to be an important tool for high risk, over the horizon AUV operations.

# Chapter 3

# Theory and Approach

The basics of the general underwater acoustic tracking problem are well established [125]. A typical acoustic tracking system is comprised of a transmitter that broadcasts acoustic signals and propagates through the non-homogeneous underwater environment which is received by one or more receivers.

Milne classifies different acoustic marker units which are used in underwater tracking and navigation systems [88]. There are five different units that function as transmitters or receivers or both which are defined as:

**Transducer:** A transmitter/receiver that sends out an interrogation signal on one frequency and receives a reply signal on a second frequency. The transducer, typically hull mounted or surface deployed, composes the topside component of the tracking system.

**Transponder:** A receiver/transmitter that upon reception of an interrogation signal on one frequency will emit a reply signal on a second frequency. The transponder, typically seabed or submersible mounted, is the subsea component of the tracking system.

**Beacon/pinger:** A transmitter that continuously emits a signal on a certain frequency. It is free running and typically seabed or submersible mounted as the subsea component of a tracking system.

**Hydrophone:** A receiver capable of receiving a reply either from a transponder or beacon/pinger. The hydrophone is a topside component of the tracking system.

**Responder:** A transmitter that can be triggered by a hardwired external control signal to transmit an interrogation signal for a transponder or hydrophone. A responder is the subsea component of a tracking system.

The signals received via these systems are processed to determine the transmitter's location relative to the receiver. As described in the previous chapter, various acoustic network topologies exist for this problem.

This thesis focuses on development of algorithms that utilize the post-processed acoustic signals to derive location information based on the extracted timing information. Various techniques have been applied to estimate a signal source: spherical (TOA), hyperbolic (TDOA), propagation models (TDOA) and conic (TDOA) [126].

In this chapter, the structure of the acoustic signal required for this localization approach and its geometric implications are described. Next, the theoretical framework for the SBSH localization algorithms, AIGL and NLSL, are presented.

## 3.1 Acoustic signal

This research is based upon a physical configuration where a periodic acoustic signal is broadcast from a free running beacon integrated into an AUV at an unknown location in the horizontal plane given by $(x_0, y_0)$. The signal is received by a single hydrophone at known different locations $H_i = H_i(x_i, y_i)$ in space and time where $i$ is the number

of receiving locations. In practice, the signal's phase difference will be determined at the different locations to determine a relative range difference to the source for each receiving location. Note that the phase difference will be referred to as TDOA for our purposes. This information will then be incorporated to derive the location of the source.

A simple continuous wave with no encoding is used for the acoustic signal. The signal is constructed such that its period is composed of a short burst of energy followed by a sufficiently long blanking window. The purpose of a signal constructed in this manner is to eliminate the risk of aliasing. A requirement is that the tracking system is not reliant upon temporal synchronization between source and receiver. So the transmit time from the beacon is not known, thus it is imperative that signal receptions be distinguishable with respect to the period, $\tau$. An illustration of an example signal is depicted in Figure 3.1.

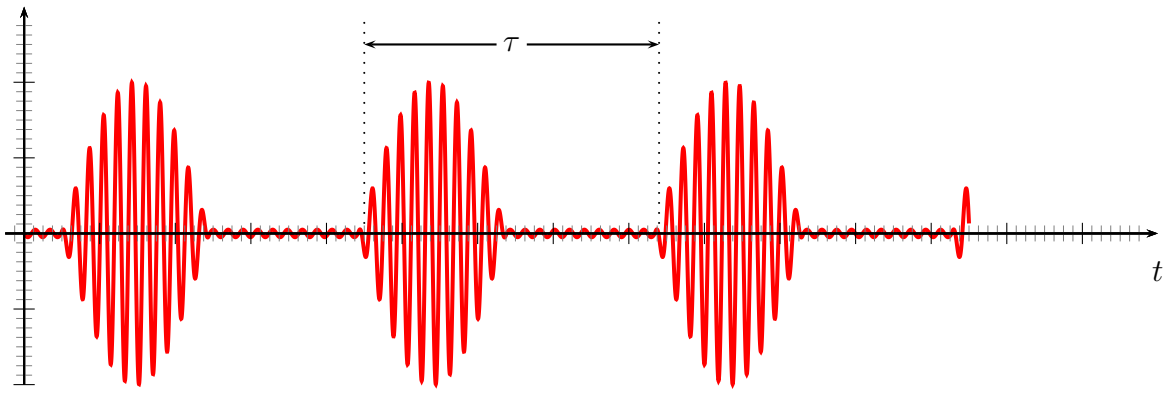


Figure 3.1: Basic unencoded acoustic signal for localization with period $\tau$.

## 3.2 Time difference of arrival

In general, when the signal is received at two distinct locations $(x_i, y_i)$ and $(x_j, y_j)$ there will be a difference in the signal TOA (see Figure 3.2). This TDOA can then be

used to determine a relative range difference between the distance of $(x_i, y_i)$ to $(x_0, y_0)$ and $(x_j, y_j)$ to $(x_0, y_0)$. Assume that the sound velocity is constant $c(T, S, D) = c$ (where $T$ is temperature, $S$ is salinity and $D$ is depth) then the range difference in distance to the source is

$$\delta_{ij} = c\Delta_{ij}.$$

The geometric interpretation of $\delta_{ij}$ is captured in Figure 3.3.

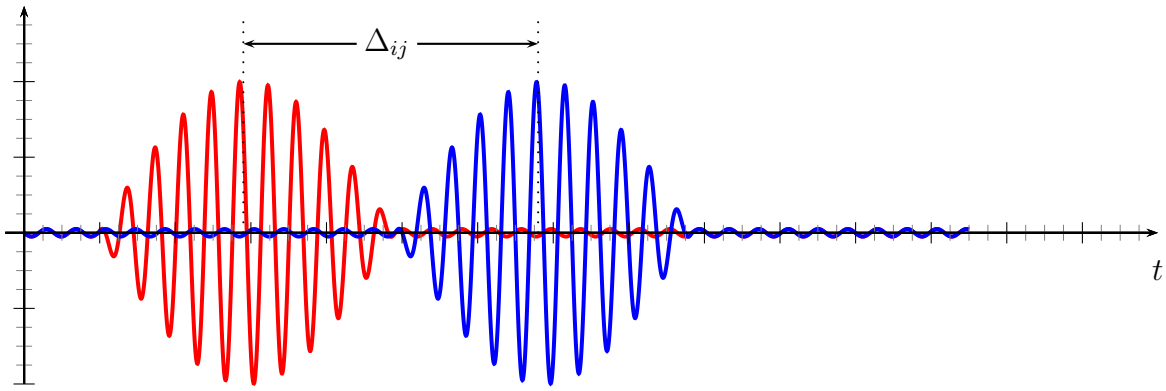


Figure 3.2: Time difference of arrival ($\Delta_{ij}$) for the same signal received at difference receiving locations $H_i$ (red) and $H_j$ (blue).

### 3.2.1 Geometric framework

Consider Figure 3.3. It is possible to create a circle of radius $\delta_{ij}$ centered at $H_j$. There is a point on this circle, say $P_j$, such that $\Delta_{ij} = 0$, i.e. the spherical or cylindrical pressure wave of the pulse in the acoustic signal arrives at $P_j$ the same time as it arrives at $H_i$ as in Figure 3.4. The circle centered at $(x_s, y_s)$ is unique. When $(x_s, y_s)$ is not known, often the case during a loss event, then there are an infinite number of circles that can be constructed including $P_j$ and $H_i$. However, with the addition of one other distinct point $P_k$ arising from the circle of radius $\delta_{ik}$ centered at $H_k$ where $H_k = H_k(x_k, y_k)$ is another receiving location, then the number of circles that include the points $H_i$, $P_j$ and $P_k$ is finite. There are up to four solutions for that general

version of the problem. In order to converge on a unique solution, a series of four receiving locations, $H_0, H_1, H_2$ and $H_3$ will be considered such as depicted in Figure 3.5.

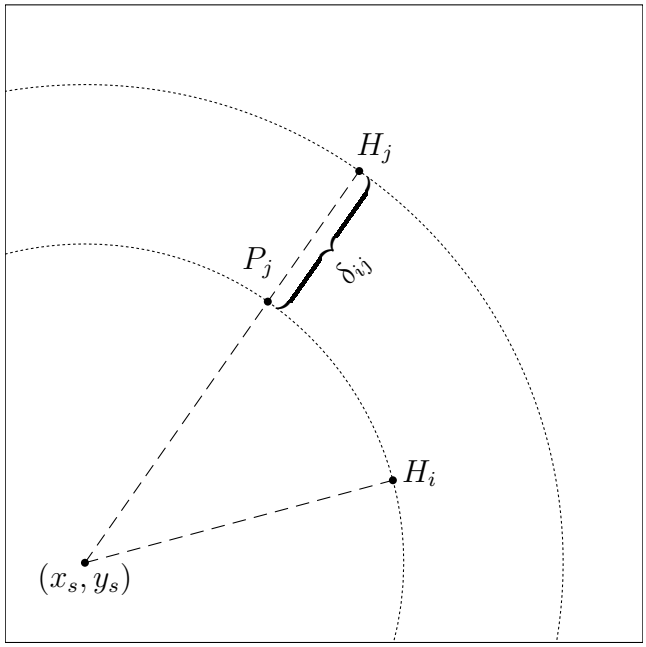


Figure 3.3: Geometric interpretation of the distance $\delta_{ij}$ with a signal emanating from $(x_0, y_0)$ and received at $H_i$ and $H_j$.

In mathematics, this is known as the problem of Apollonius, after Apollonius of Perga [127]. Given three geometric objects: point, line and/or circle, it is possible to construct a circle that passes through the points and is tangent to the lines and/or circles. The methods associated with derivation of a closed form of the positioning solution for GPS using the Apollonius problem have been explored [128]. These methods are not known to have been previously applied in acoustic localization. In the case of Figure 3.5, the unique solution for the problem is depicted in Figure 3.6.

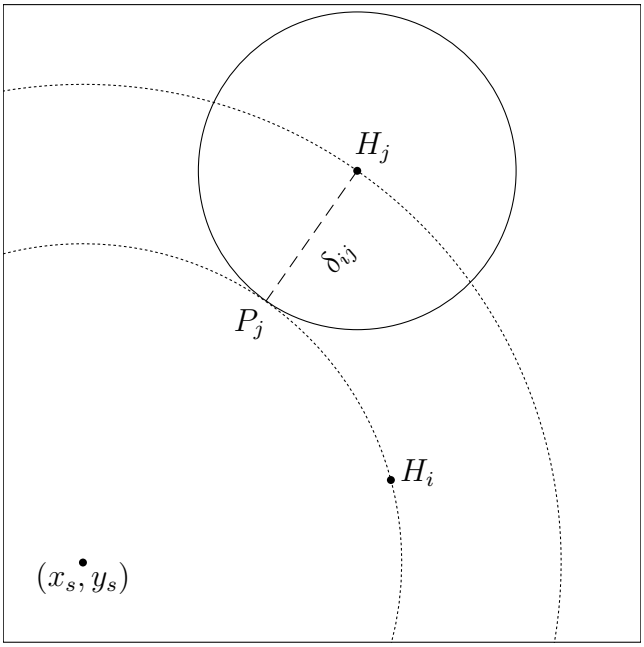


Figure 3.4: Circle of radius $\delta_{ij}$ centered at $H_j$ tangent at $P_j$ which is a point on the surface of the acoustic pressure wave the same distance from the source as $H_i$.

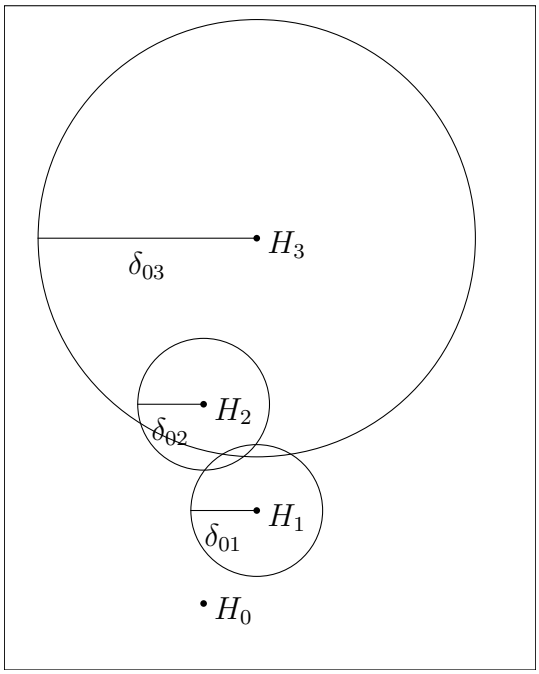


Figure 3.5: The receiving locations $H_0$, $H_1$, $H_2$, $H_3$ and the TDOA for those locations $\delta_{01}$, $\delta_{02}$, $\delta_{03}$.

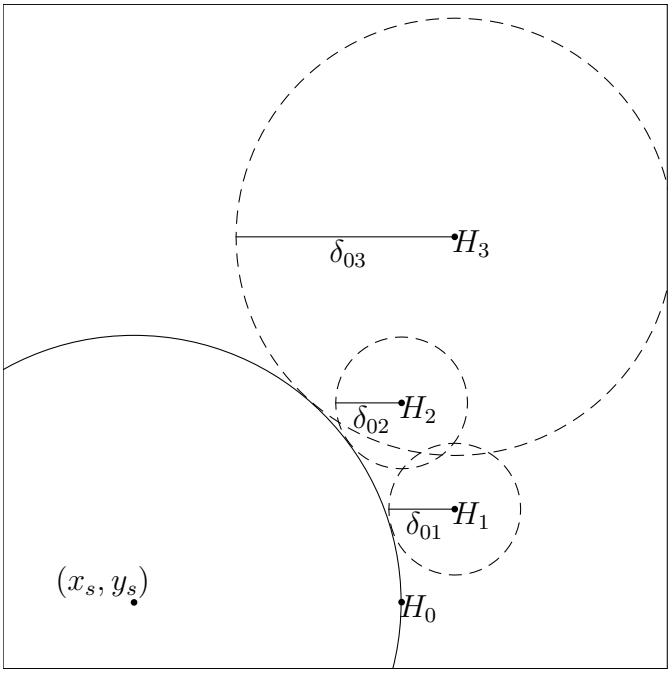


Figure 3.6: The source solution location $(x_s, y_s)$ for the given receiver locations $H_0$, $H_1$, $H_2$, $H_3$ and the TDOA for those locations $\delta_{01}$, $\delta_{02}$, $\delta_{03}$.

### 3.2.2 Inversive geometry

As Coxeter [127] points out, different methods have been applied to solve this problem dating back to Apollonius' own two volume series 'Contacts'. It has engaged many notable geometers since Vieta, Descartes and Newton. The method utilized here will be to employ an inversive transformation attributed to Steiner, Plücker and/or Liouville [129]. Inversion is a modern geometry developed in the first half of the ninteenth century [130]. The non-Euclidean transformation of inversion is based on Definition 3.2.1.

**Definition 3.2.1.** *Two points $P$ and $P'$ are inverse points with respect to a point $O$ and given a positive real number $k$ if $OP \cdot OP' = k$ and $O, P, P'$ are collinear.*

A geometric illustration of inversion is depicted in Figure 3.7. The example distance values for this illustration are $\sqrt{k} = 2$, $OP = 1$ and $OP' = 4$.

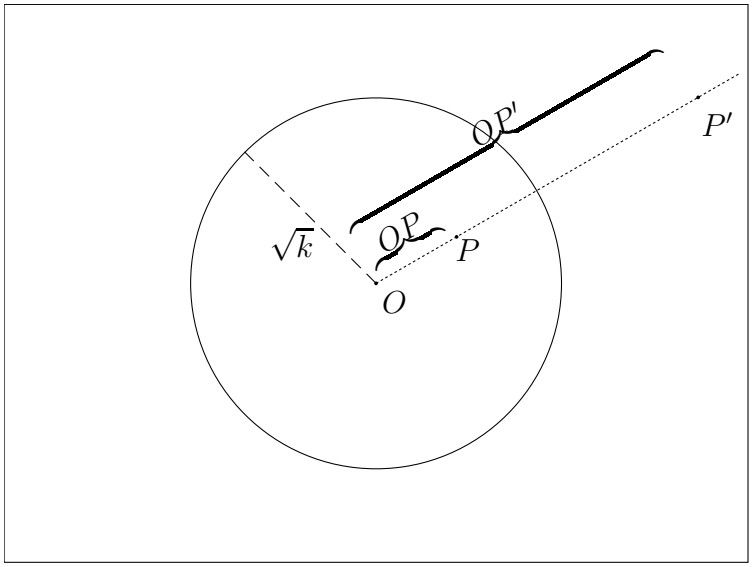


Figure 3.7: Geometric illustration of the inversion transformation, the points $P$ and $P'$ are inversion pairs.

The point $O$ and the constant $k$ define the circle of inversion for this transformation. This transformation maps points outside the circle of inversion to its inside and vice versa. A useful property that we will exploit is that any circle that passes though the centre of the circle of inversion maps to a line and that points that lie on the circumference of the circle of inversion are invariant, i.e. they map to themselves. Three inversion pairs are shown in Figure 3.8. It will be shown that the choice of the circle of inversion can simplify the derivation of the circle associated with the source location.

When the circle of inversion is centered at the origin, i.e. $x^2 + y^2 = r^2$, then the inversion transformation equation for the co-ordinate pair $(x, y)$ is the co-ordinate pair $(x', y')$ such that

$$x' = \frac{xr^2}{x^2 + y^2}, \qquad y' = \frac{yr^2}{x^2 + y^2}. \tag{3.1}$$

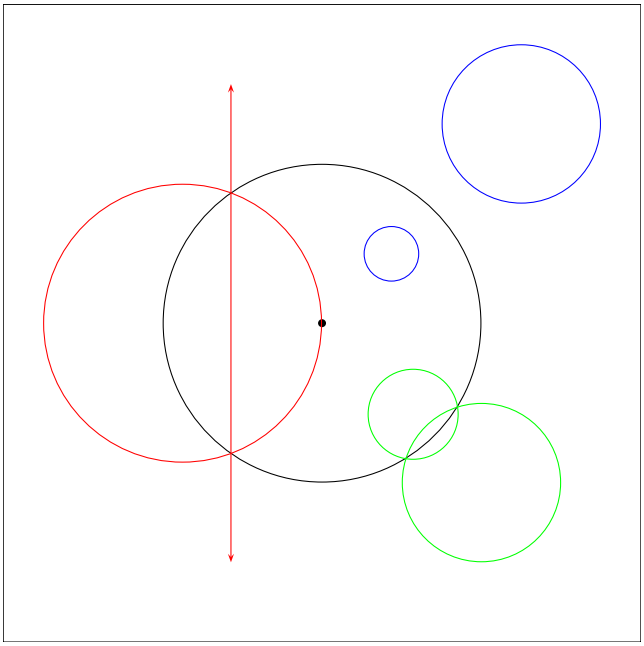

Figure 3.8: Examples of inversive pairs for a given circle of inversion (black).

The inverse equations for a general circle of inversion centered at $(h, k)$ are given by

$$x' - h = \frac{(x-h)r^2}{(x-h)^2 + (y-k)^2}, \qquad y' - k = \frac{(y-k)r^2}{(x-h)^2 + (y-k)^2}. \tag{3.2}$$

### 3.2.3 Receiver array geometry

It is necessary to configure the sample location geometry for the receivers in a certain manner in order to reduce the Apollonian problem to a specific case. For example, consider a set of only three receiving locations $(H_0, H_1, H_2)$ spaced as vertices of a triangle. Three general possibilities arise for the circle arrangement as shown in Figure 3.9. There can either be one TDOA circle $(b)$ or two TDOA circles $(a)$ and $(c)$. In the case of two TDOA circles, the circles can either be mutually exclusive $(a)$ or intersect $(c)$. One can consider tangency as the case of a single intersection point. Note that these different circle arrangements arise from an identical receiving array. The only

change is the position of the source relative to the array.

There are four general solutions to $(a)$ and only two for $(b)$ and $(c)$. The inversive transformation method employed in this thesis requires the latter cases where there are intersections of the TDOA circles because a TDOA intersection point is used to define the centre of inversion thereby enabling exploitation of the circles through the origin transformed to lines.

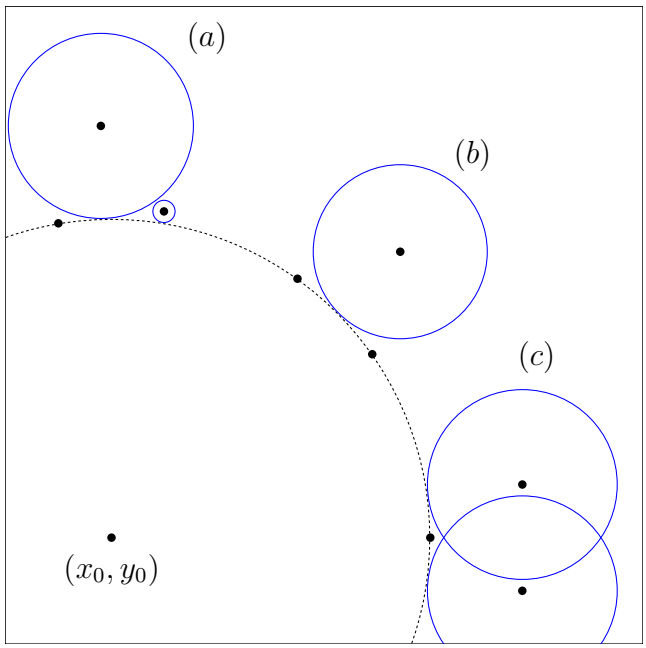


Figure 3.9: A sample of the possible TDOA circle patterns resulting from the difference in receiver geometry relative to the source located at $(x_0, y_0)$.

Consider the three point receiving array, then there are regions where the source could be located that result in case $(a)$ from Figure 3.9, i.e. no TDOA circle intersections. This absence of intersection depends on the range and location of the source relative to the array orientation. In order to mitigate against this result and ensure the existence of a TDOA circle arrangement with suitable intersection, a fourth receiving point is added to the array. The introduction of this fourth receiving location eliminates the possibility of non-intersecting TDOA circles for any source location

external to the array. It is possible to determine this non-intersecting TDOA region within the array. Set the four receiver locations at the corners of a square and the source location given by:

$$\begin{aligned} H_0 &= H_0(x_0, y_0); \\ H_1 &= H_1(x_1, y_1); \\ H_2 &= H_2(x_2, y_2); \\ H_3 &= H_3(x_3, y_3); \\ S &= S(x_s, y_s). \end{aligned}$$

Without loss of generality, it suffices to consider $H_0$ as the point closest to the source location, $S$. The radius of the TDOA circles at the other receiver locations are:

$$\begin{aligned} \delta_{01} &= \sqrt{(x_s - x_1)^2 + (y_s - y_1)^2} - \sqrt{(x_s - x_0)^2 + (y_s - y_0)^2}; \\ \delta_{02} &= \sqrt{(x_s - x_2)^2 + (y_s - y_2)^2} - \sqrt{(x_s - x_0)^2 + (y_s - y_0)^2}; \\ \delta_{03} &= \sqrt{(x_s - x_3)^2 + (y_s - y_3)^2} - \sqrt{(x_s - x_0)^2 + (y_s - y_0)^2}. \end{aligned}$$

Then the conditions for non-intersection TDOA circles are:

$$\delta_{01} + \delta_{02} < \sqrt{(x_1 - x_2)^2 + (y_1 - y_2)^2}, \text{ and} \tag{3.3}$$

$$\delta_{02} + \delta_{03} < \sqrt{(x_2 - x_3)^2 + (y_2 - y_3)^2}. \tag{3.4}$$

Explicitly, the only possible source locations $(x_s, y_s)$ that result in nonintersecting TDOA circles are located inside the region bounded by Inequalities 3.3 and 3.4 generalized to each of the receiver locations. The set of curves that create the bounded region are shown in Figure 3.10. A source location outside of the receiver box ensures

that:

$$\delta_{0i} + \delta_{0,i+1} > \sqrt{(x_i - x_{i+1})^2 + (y_i - y_{i+1})^2}$$

for some $i$, thus ensuring an intersection.

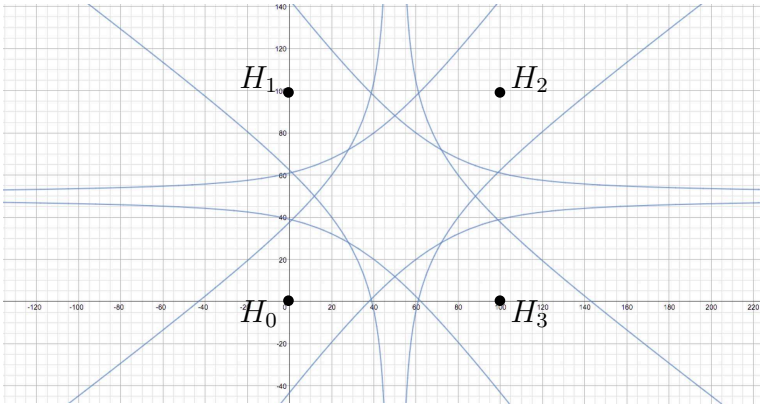


Figure 3.10: The region bounded by the given curves indicates the set of possible locations of source $(x_s, y_s)$ that result in nonintersecting TDOA circles for a sample of four receiving locations set at the corners of a 100 m $\times$ 100 m array.

The box-style four point receiving array is the receiver configuration that will be used to illustrate and evaluate the SBSH localization algorithms in detail. In addition to eliminating the possibility of non-intersecting circles, see Figure 3.10, the general symmetry of the box-style configuration can reduce the space required to thoroughly evaluate the SBSH algorithm and make conclusions regarding its performance. The source need only be considered in a 90° sector relative to the centre of the array. Contrast this to an 120° sector to cover the set of all orientations for an equilateral triangle configured receiving array relative to the source location.

# Chapter 4

# The Single Beacon, Single Hydrophone Localization Algorithms

In this chapter, the SBSH localization algorithms are described in detail. The algorithms are applied to the two dimensional problem. The source of the acoustic signal (AUV beacon) and the receiver (hydrophone) are located in three dimensional space in reality; however, the hydrophone and AUV will be treated as in the same horizontal plane. The system is proposed for missions where the vehicle is operating at relatively shallow depths and potentially sitting stationary beneath the ice layer. Then the vertical difference between the AUV depth and the hydrophone will be insignificant in terms of the horizontal distances expected for this application. Therefore the work is in only two dimensions to reduce the complexity of the solutions. The sound velocity is assumed to be $c = 1500\,\mathrm{m/s}$. This algorithm has been implemented in the Matlab numerical computing environment.

## 4.1 Control case

Consider the following problem which illustrates the utility of the SBSH algorithm to localize an acoustic source. Suppose that the source is transmitting from a location approximately 22 km away from the vicinity of the receiver array. The location of the source will be determined using the SBSH algorithm and by using a standard approach by directly solving the non-linear system associated with the particular case. The sections of pseudocode related to the algorithm are presented as they relate to the exposition of the algorithm.

### 4.1.1 Algorithm I: Establish Inversion Transformation

For this case, there are four receiving stations located on the corners of a 200 m $\times$ 200 m box. The receiver array is temporarily given by:

$$\begin{aligned} H_0 = H_0(x_0, y_0) &= H_0(100, 100); \\ H_1 = H_1(x_1, y_1) &= H_1(100, 300); \\ H_2 = H_2(x_2, y_2) &= H_2(300, 300); \\ H_3 = H_3(x_3, y_3) &= H_3(300, 100). \end{aligned}$$

Measurements are made at each receiver location $H_i$. The reference signal is set at $H_0$ then a set of TDOA measurements (in milliseconds) for the remaining receivers is

$$\begin{aligned} H_1 : \Delta_{01} &= -58.905\,\text{ms}; \\ H_2 : \Delta_{02} &= -178.642\,\text{ms}; \\ H_3 : \Delta_{03} &= -119.256\,\text{ms}. \end{aligned}$$

Note the negative denotes an earlier arrival time compared to the reference signal. The radial distance relative to $H_0$ for each receiver location is:

$$\begin{aligned}
H_0(100,100) : c \cdot \Delta_{00} = 1500\,\mathrm{m\,s^{-1}} \times 0\,\mathrm{ms} &= 0\,\mathrm{m};\\
H_1(100,300) : c \cdot \Delta_{01} = 1500\,\mathrm{m\,s^{-1}} \times -58.905\,\mathrm{ms} &= -88.358\,\mathrm{m};\\
H_2(300,300) : c \cdot \Delta_{02} = 1500\,\mathrm{m\,s^{-1}} \times -178.642\,\mathrm{ms} &= -267.963\,\mathrm{m};\\
H_3(300,100) : c \cdot \Delta_{03} = 1500\,\mathrm{m\,s^{-1}} \times -119.256\,\mathrm{ms} &= -178.885\,\mathrm{m}.
\end{aligned}$$

The receiver locations are reordered and renamed based on increasing radial distance to the source relative to the closest receiver location. The sorted receiver array with the relative distance:

$$\begin{aligned}
H_0(300,300) : \delta_{00} &= 0\,\mathrm{m};\\
H_1(300,100) : \delta_{01} &= 89.078\,\mathrm{m};\\
H_2(100,300) : \delta_{02} &= 179.605\,\mathrm{m};\\
H_3(100,100) : \delta_{03} &= 267.963\,\mathrm{m}.
\end{aligned}$$

The discrepancy between $\delta_{01}$, $\delta_{02}$ and $c \cdot \Delta_{01}$, $c \cdot \Delta_{03}$ is due to the former being relative to $H_0(300,300)$ and the latter being relative to $H_0(100,100)$, i.e. $\delta_{01} = |c \cdot \Delta_{02}| - |c \cdot \Delta_{03}|$, and similarly for $\delta_{02}$.

It is now possible to generate the set of TDOA circles arising from the given receiver array configuration and the relative difference of arrival times with the closest receiver to the source, i.e. $H_0$. The source location is the centre of the circle tangent to the three TDOA circles and the point.

Notice that in Figure 4.1 not all the TDOA circles intersect. It is necessary to

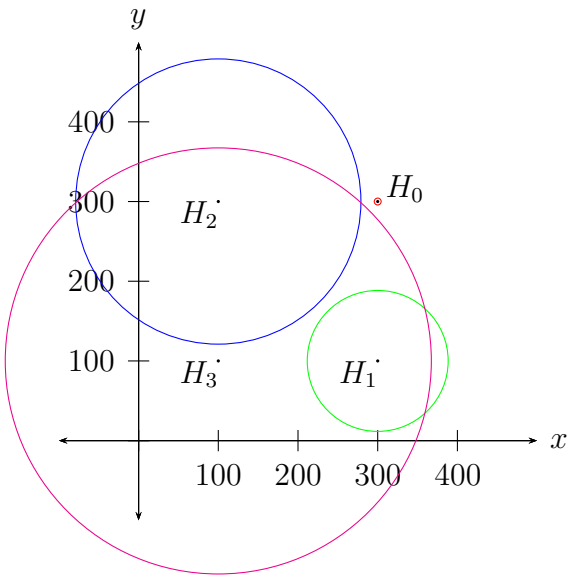


Figure 4.1: The circle set arising from the TDOA measurements.

isolate an intersecting pair for generation of the centre of inversion and the radius. In this case, the circles arising from $H_2$ (blue) and $H_3$ (magenta) are used. The two intersection points of these circles are:

$$Intersection(H_2, H_3) = \{(279.601, 298.866), (-79.601, 298.866)\}.$$

Arbitrarily, the centre of the circle of inversion is set to $O = O(279.601, 298.866)$. Then the radius of the circle of inversion is given by:

$$O_{rad} = \sqrt{(279.601 - (-79.601))^2 + (298.866 - 298.866)^2} = 359.203\,\mathrm{m}.$$

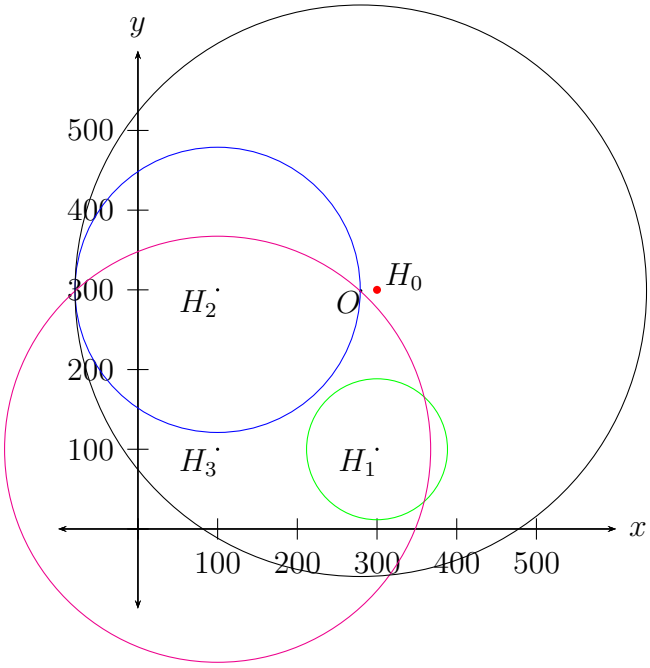


Figure 4.2: The circle of inversion to be used for the inverse transformation of the problem.

**Algorithm 1** AIGL: Establish inversion transformation

**function** SOURCEFIND($H_i(x_i, y_i), \Delta_{0i}$)
  $H_i \leftarrow$ Receiver locations for $i \in \{0, 1, 2, 3\}$
  $\Delta_{0i} \leftarrow$ Phase difference measurements for $\forall i \neq 0$
  $\epsilon_\alpha \leftarrow$ Equality and proximity thresholds $\exists \alpha \in \mathbb{N}$
    ▷ Can affect final position estimate accuracy and algorithm run time
  $\delta_{0i} \leftarrow c \times \Delta_{0i}, \forall i \neq 0$
  **function** SORT($H_i, \delta_{0i}$)  ▷ Ascending sort on $H_i$ such that $\delta_{01} < \delta_{02} < \delta_{03}$
  $(H_i, \delta_{0i}) \leftarrow$ ResultSORT
  **for** $i \neq j$ **do**
    Check: $Circle_{H_i} \cap Circle_{H_j} \neq \emptyset$
    $O(x, y) \leftarrow (Circle_{H_i} \cap Circle_{H_j})_{Point1}, \exists i \neq j$
      ▷ Set centre for circle of inversion
    **function** DIST($(Circle_{H_i} \cap Circle_{H_j})_{Point1}, (Circle_{H_i} \cap Circle_{H_j})_{Point2}$)
    $O_{Radius} \leftarrow$ ResultDIST  ▷ Set radius for circle of inversion
  $Circle_O \leftarrow (O, O_{Radius})$

### 4.1.2 Algorithm II: Inversion transformation

Once the circle of inversion is set, it is possible to apply the inverse transformation, $T_I$. Recall the inverse transformation Equation 3.2. The equations can be now written explicitly as:

$$T_I : \begin{cases} x' - 279.601 &= \frac{(x-279.601)(359.203)^2}{(x-279.601)^2+(y-298.866)^2}, \\ y' - 298.866 &= \frac{(y-298.866)(359.203)^2}{(x-279.601)^2+(y-298.866)^2} \end{cases} \tag{4.1}$$

Apply the transformation to the reference signal receiver location $H_0(300, 300)$:

$$T_I : H_0(300, 300) \mapsto H_0'(6585.343, 649.405).$$

Recall that circles that pass through the origin of the inversion circle transform to lines and points that lie on the circumference of the inversion circle are invariant. In order to transform the TDOA circles centred at $H_2$ and $H_3$, it is necessary to determine where those circles intersect with the circle of inversion centred at $O$. Therefore, the TDOA circles centred at $H_2$ and $H_3$ are respectively transformed into the lines given by:

$$\ell_2 : \quad 158.382x - y = 12906.316;$$

$$\ell_3 : \quad -0.903x + y = 226.976.$$

Consider Figure 4.3 depicting the transformed TDOA circles. Note, due to scaling the point $H_0'$ is not shown.

In the inverted space, the problem is reduced to finding the point equidistant to the inverted point $H_0'$ and the two lines $\ell_2, \ell_3$.

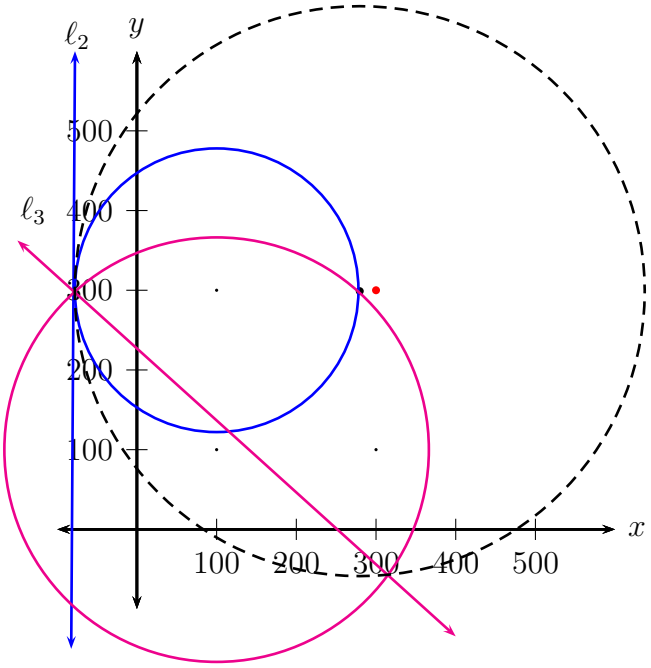


Figure 4.3: The inversion circle (black) TDOA circles (blue, magenta) and their inversion pairs, respectively $\ell_2$ and $\ell_3$.

**Algorithm 2** AIGL: Inversion Transformation

▷ NOTE the actual code must account for different combinations of $H_1, H_2, H_3$. $H_2, H_3$ employed to be consistent with the control problem.

14: **function** INVERT($H_0$)

15: $H_0' \leftarrow$ ResultINVERT

16: **procedure** FINDINTERSECTION($Circle_O, Circle_{H_2}$)
▷ FINDINTERSECTION returns a pair of coordinate pairs

17: $intOH_2 \leftarrow$ ResultFINDINTERSECTION

18: **procedure** FINDLINE($intOH_2$)
▷ FINDLINE returns the line (standard form) defined by the two coordinate pairs of $intOH_2$

19: $\ell_2 \leftarrow$ ResultFINDLINE

20: **procedure** FINDINTERSECTION($Circle_O, Circle_{H_3}$)

21: $intOH_3 \leftarrow$ ResultFINDINTERSECTION

22: **procedure** FINDLINE($intOH_3$)

23: $\ell_3 \leftarrow$ ResultFINDLINE

### 4.1.3 Algorithm III: Inversion space solution

After applying the inversion transformation, the problem of finding a circle tangent to two circles a point is transformed to a problem of finding a point $(x', y')$ equidistant from a point and two lines, i.e. a circle touching these three objects. Figure 4.4 depicts the geometry of the problem.

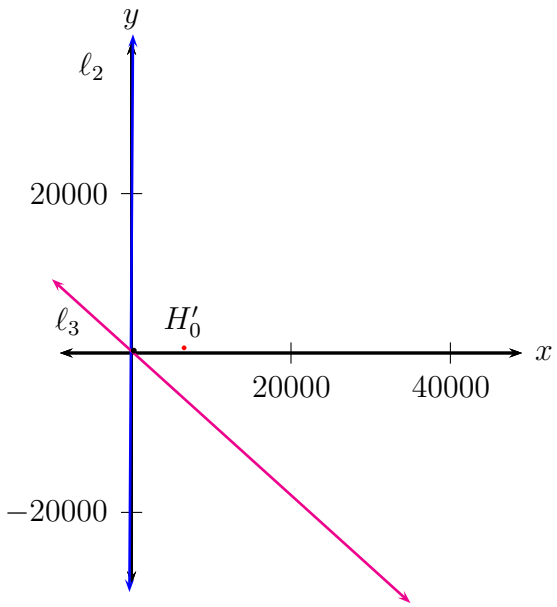


Figure 4.4: The problem reformulated in inversion space: a point and two lines. Note for reference, the circle of inversion is barely visible in proximity to the origin.

The general form for finding the perpendicular distance, $r$ from a point $P(x, y)$ to a line $Ax + By + C = 0$ is given by:

$$r = \frac{|Ax + By + C|}{\sqrt{A^2 + B^2}}.$$

Then the point $(x', y')$ can be found by simultaneously solving the following nonlinear

system of equations:

$$\begin{aligned} |158.382x - y - 12906.316| &= 158.386r; \\ |-0.903x + y - 226.976| &= 1.348r; \\ \sqrt{(x - 6585.343)^2 + (y - 649.405)^2} &= r \end{aligned} \tag{4.2}$$

where $r$ is the distance to $H_0'(6585.343, 649.405)$ and the perpendicular distance to $\ell_2$, $\ell_3$.

Finding a solution to this problem involves moving outward from the intersection of $\ell_2$ and $\ell_3$ along the bisecting lines to find a point equidistant to $H_0'$ and one of $\ell_2$, $\ell_3$. Figure 4.5 shows these lines for this version of the problem.

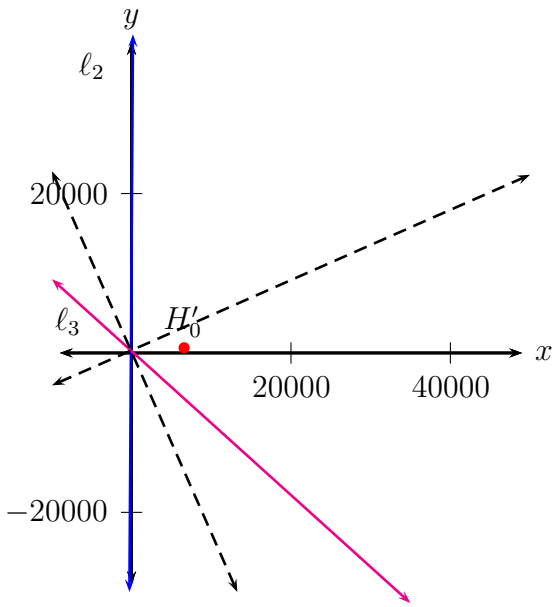


Figure 4.5: The solution to the problem reformulated in inversion space lies on the line that bisects the angles created by the coloured lines.

The Matlab `fsolve` function is used to find the solution to the non-linear system. It generally solves a system $F(x) = 0$ by minimizing the sum of squares for each $x_i \in x = (x_1, x_2, ..., x_n)$ for all $F_i = (F_1(x), F_2(x), ...F_n(x))$.

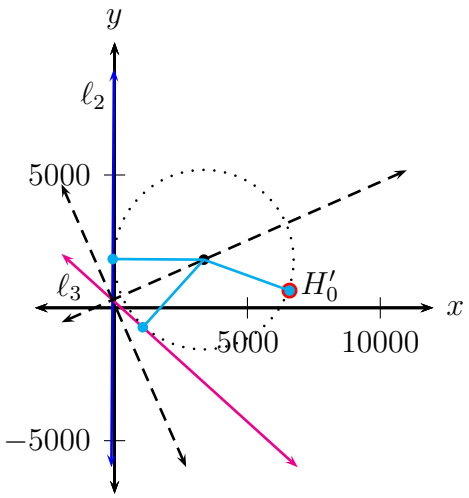


Figure 4.6: The solution in inversion space is the point equidistant to $H_0', \ell_2$ and $\ell_3$.

There are two sets of solutions to the non-linear problem described by Equations 4.2. An individual solution comprises of a set of three pairs or points. The solutions are visualized by considering the two circles that pass through $H_0'$ and are tangent to the two inverted circles (i.e. lines) as depicted in Figure 4.5. In order to find the solutions, it is necessary to determine a point equidistant to those lines and $H_0'$. One such solution point is depicted in Figure 4.6.

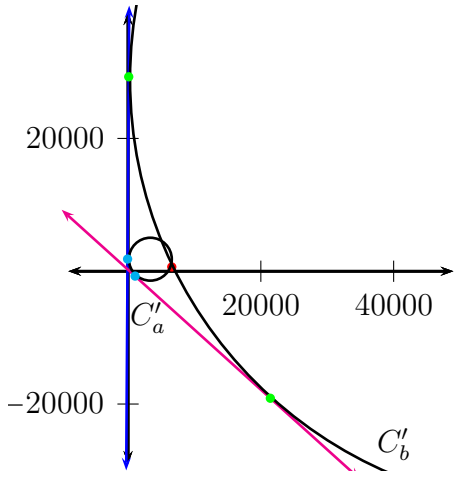


Figure 4.7: The circle $C_a'$ and circle arc section corresponding to a circle $C_b'$ are tangent to the two inverted circles and passing throughout the point $H_0'$.

Note that the centres of the solution circles shown in Figure 4.7 do not constitute the solution to the localization problem in inversion space. That is, if the centres are transformed back to regular cartesian space neither will correspond to the source location. Rather it is the points of tangency that are required. The points of tangency corresponding to the circles $C'_a$ and $C'_b$ are:

$$\{H'_0(6585.343, 649.405), C'_{a1}(-69.898, 1835.668), C'_{a2}(1060.942, -731.190)\},$$

$$\{H'_0(6585.343, 649.405), C'_{b1}(103.398, 29282.809), C'_{b2}(21430.945, -19127.890)\}.$$

**Algorithm 3** AIGL: Inverted Space Solution

24: **procedure** BISECTLINE($\ell_2, \ell_3$)
▷ BISECTLINE returns the rise, run of the line bisecting the angle between $\ell_2, \ell_3$
25: $m = (m_1, m_2) \leftarrow$ ResultBISECTLINE
26: **procedure** INITPOINTSCALEFACTOR($m$)
▷ INITPOINTSCALEFACTOR returns a value $10^k$ for some $k > 0$ when $|m(1) \cdot m(2)| \approx 0$
27: $p \leftarrow$ ResultINITPOINTSCALEFACTOR
28: $i \leftarrow 10$ ▷ set counters
29: $k \leftarrow 0$
30: $a \leftarrow 1$ ▷ set condition variables
31: $b \leftarrow 0$
32: $c \leftarrow 0$
33: **procedure** LINEINTERSECTION($\ell_2, \ell_3$)
▷ LINEINTERSECTION returns the intersection point of $\ell_2, \ell_3$
34: $InitialSolution_1 \leftarrow$ ResultLINEINTERSECTION
35: $InitalSolutionCentre \leftarrow InitialSolution_1$
36: **while** $\neg((a = b) \wedge (b = c) \wedge (a = c))$ **do**
37: **function** FSOLVE($H'_0, \ell_2, \ell_3$) ▷ FSOLVE applied to inversion problem
38: $TangentCircleSolution_1 \leftarrow$ ResultFSOLVE
39: **procedure** ADVANCESEARCH($i, k, m, p, InitalSolutionCentre$)
40: ▷ move $InitialSolution_1$ outward from $InitalSolutionCentre$ along $\ell_2, \ell_3$ bisecting axis (see Fig 4.5 by increment of $p * i$ every $k = 4^{th}$ iteration of loop
41: $InitialSolution_1 \leftarrow$ ResultADVANCESEARCH
42: **function** DIST($TangentCircleSolution_1, H'_0$)
43: $a \leftarrow$ ResultDIST
44: **function** POINTLINEDIST($TangentCircleSolution_1, \ell_2$)
▷ Perpendicular distance from point to line
45: $b \leftarrow$ ResultPOINTLINEDIST
46: **function** POINTLINEDIST($TangentCircleSolution_1, \ell_3$)
47: $c \leftarrow$ ResultPOINTLINEDIST
48: $k = k + 1$
49: **if** $Mod(k, 4) = 0$ **then**
50: $i = i + 100$ ▷ Increase $i$ each $k = 4^{th}$ iteration of loop
51: **if** $i > 100000$ **then** ▷ WHILE loop exit condition, user defined - influences sim runtime
52: $a \leftarrow 0$
53: $b \leftarrow 0$
54: $c \leftarrow 0$

**Algorithm 4** AIGL: Inverted Space Solution

▷ Apply FSOLVE to determine second inverted space solution distinct from $TangentCircleSolution_1$

55: $TangentCircleSolution_2 \leftarrow TangentCircleSolution_1$
56: $k \leftarrow 0$ ▷ reset $k$ counter
57: $a \leftarrow 1$ ▷ reset condition variables
58: $b \leftarrow 0$
59: $c \leftarrow 0$
60: **procedure** LINEINTERSECTION($\ell_2, \ell_3$)
61: $InitialSolution_2 \leftarrow$ ResultLINEINTERSECTION
62: $InitalSolutionCentre \leftarrow InitialSolution_2$
63: **while** $\neg((a = b) \wedge (b = c) \wedge (a = c) \wedge (TangentCircleSolution_2 \neq TangentCircleSolution_1))$ **do**
64: **function** FSOLVE($H'_0, \ell_2, \ell_3$)
65: $TangentCircleSolution_2 \leftarrow$ ResultFSOLVE
66: **procedure** ADVANCESEARCH($i, k, m, p, InitalSolutionCentre$) ▷ $i$ carried from $TangentCircleSolution_1$ loop
67: $InitialSolution_2 \leftarrow$ ResultADVANCESEARCH
68: **function** DIST($TangentCircleSolution_2, H'_0$)
69: $a \leftarrow$ ResultDIST
70: **function** POINTLINEDIST($TangentCircleSolution_2, \ell_2$)
71: $b \leftarrow$ ResultPOINTLINEDIST
72: **function** POINTLINEDIST($TangentCircleSolution_2, \ell_3$)
73: $c \leftarrow$ ResultPOINTLINEDIST
74: $k = k + 1$
75: **if** $Mod(k, 4) = 0$ **then**
76: $i = i + 1000$ ▷ $i$ step increased in second loop
77: **if** $i > 1000000$ **then** ▷ WHILE loop exit condition increased in second loop
78: $a \leftarrow 0$
79: $b \leftarrow 0$
80: $c \leftarrow 0$

### 4.1.4 Algorithm IV: Retransformation and solution

The inverse transformation can be applied to transform the tangent points back to the regular cartesian space. Applying Equations 3.2 to the solution set yields the following two sets of points:

$$\{H_0(300,300), C_{a1}(261.447,378.695), C_{a2}(339.914,219.354)\},$$

$$\{H_0(300,300), C_{b1}(279.574,303.318), C_{b1}(282.910,295.827)\}$$

Given three pairs of points $(x_1,y_1),(x_2,y_2)$ and $(x_3,y_3)$, it is possible to determine the circle defined by those points by solving:

$$\begin{vmatrix} x^2+y^2 & x & y & 1 \\ x_1^2+y_1^2 & x_1 & y_1 & 1 \\ x_2^2+y_2^2 & x_2 & y_2 & 1 \\ x_3^2+y_3^2 & x_3 & y_3 & 1 \end{vmatrix} = 0. \tag{4.3}$$

The two circles determined from the two sets of tangent points $\{H_0, C_{a1}, C_{a2}\}$ and $\{H_0, C_{b1}, C_{b2}\}$ are

$$C_a: \quad (x-20000)^2+(y-10000)^2 = 21958.60^2,$$

$$C_b: \quad (x-290.09)^2+(y-303.51)^2 = 10.52^2$$

In this case, $C_b$ lies only just outside the receiving array location. It corresponds to the solution in inversion space that was much further out, i.e. greater distance to the intersection of $\ell_2, \ell_3$ (the initialization point) and consequently larger range to $(H_0', \ell_2, \ell_3)$.

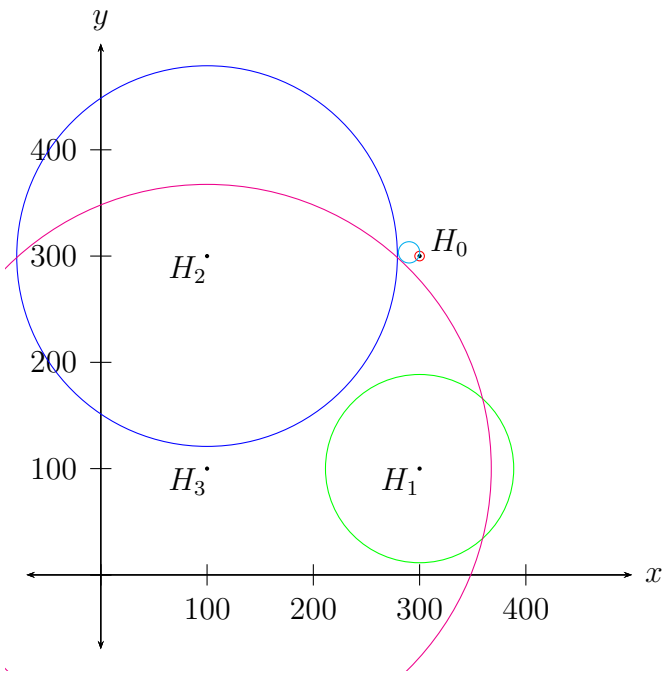


Figure 4.8: The possible solution arising from $C_b$ (shown in cyan). Note it is not tangent to the TDOA circle stationed at receiver location $H_1$ (shown in green).

From a practical perspective, it would be unlikely that a source located at the centre of $C_b$ would be lost for very long, see Figure 4.8. However, it can be eliminated as the solution because it is not tangent with the TDOA circle arising from receiver location $H_1$. The unique solution to the problem is the centre of the circle $C_a$, see Figure 4.9.

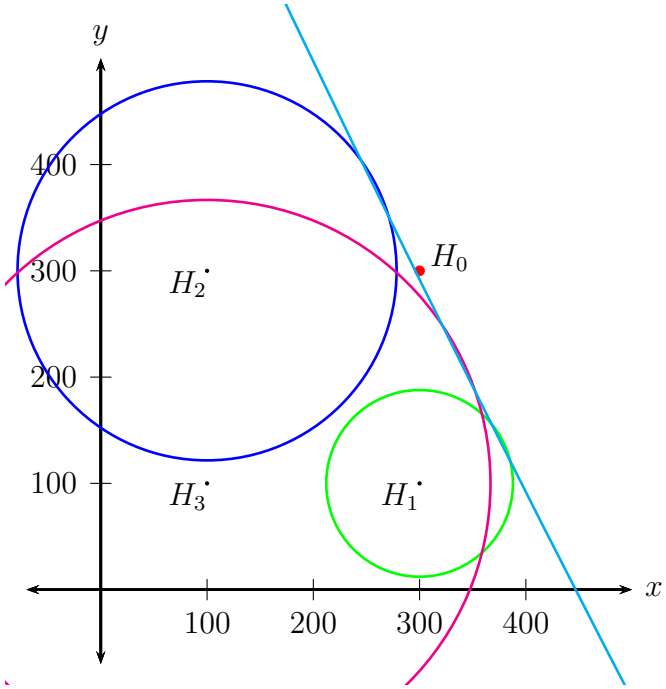


Figure 4.9: The unique solution arising from $C_a$ (shown in cyan) tangent to $H_0$ and the three TDOA circles centred at receiver locations $H_1, H_2$ and $H_3$. $C_a$ appears linear due to its large radius.

**Algorithm 5** AIGL: Retransformation and solution

▷ Determine solution one.

**procedure** FINDTANGENTPOINT($TangentCircleSolution_1, \ell_2$)
$TangentPointOneSolution_1 \leftarrow$ ResultFINDTANGENTPOINT
**procedure** FINDTANGENTPOINT($TangentCircleSolution_1, \ell_3$)
$TangentPointTwoSolution_1 \leftarrow$ ResultFINDTANGENTPOINT
**function** INVERT($TangentPointOneSolution_1$)
$PerimPntOneSolution_1 \leftarrow$ ResultINVERT
**function** INVERT($TangentPointTwoSolution_1$)
$PerimPntTwoSolution_1 \leftarrow$ ResultINVERT
**function** FINDCIRCLE($PerimPntOneSolution_1, PerimPntTwoSolution_1, H_0$)
$Solution_1 \leftarrow$ ResultFINDCIRCLE

▷ Determine solution two.

**procedure** FINDTANGENTPOINT($TangentCircleSolution_2, \ell_2$)
$TangentPointOneSolution_2 \leftarrow$ ResultFINDTANGENTPOINT
**procedure** FINDTANGENTPOINT($TangentCircleSolution_2, \ell_3$)
$TangentPointTwoSolution_2 \leftarrow$ ResultFINDTANGENTPOINT
**function** INVERT($TangentPointOneSolution_2$)
$PerimPntOneSolution_2 \leftarrow$ ResultINVERT
**function** INVERT($TangentPointTwoSolution_2$)
$PerimPntTwoSolution_2 \leftarrow$ ResultINVERT
**function** FINDCIRCLE($PerimPntOneSolution_2, PerimPntTwoSolution_2, H_0$)
$Solution_2 \leftarrow$ ResultFINDCIRCLE
Check validity of $Solution_i$ with respect to $Circle_{H_1}$

▷ Can use $DIST(H_1, Solution_i) = DIST(H_0, Solution_i) + \delta_{01}$

### 4.1.5 Algorithm V: Result

There are numerical errors associated with the algorithm as described in Table 4.1. The source location to the tenth decimal place determined by the AIGL algorithm in this case is:

$$(x_s, y_s)_{AIGL} = (19999.9999998646, 9999.9999999325).$$

The actual source location used for the problem is $(x_s, y_s) = (20000.000, 10000.000)$. Therefore, there is good agreement between the AIGL estimated source location and the actual source location for the control problem example.

| Source | $x$ | $\text{Error}_x$ | $y$ | $\text{Error}_y$ | Range | $\text{Error}_{Range}$ |
|---|---|---|---|---|---|---|
| Actual | 20000 | 0 | 10000 | 0 | 22092.532 | 0 |
| AIGL | 20000 | $1.35 \times 10^{-7}$ | 10000 | $6.75 \times 10^{-8}$ | 22092.532 | $1.51 \times 10^{-7}$ |

Table 4.1: Position estimate error and range estimate error for the AIGL. All units are in metres.

## 4.2 Standard non-linear system approach

An alternative approach, NLSL, to solve the single beacon, single hydrophone version of the localization problem would be to solve the following system of non-linear equations directly.

$$\begin{aligned} (x - x_0)^2 + (y - y_0)^2 &= r^2 \\ (x - x_1)^2 + (y - y_1)^2 &= (\delta_{01} + r)^2 \\ (x - x_2)^2 + (y - y_2)^2 &= (\delta_{02} + r)^2 \\ (x - x_3)^2 + (y - y_3)^2 &= (\delta_{03} + r)^2 \end{aligned} \tag{4.4}$$

An illustration of the problem is shown in Figure 4.10. The source location coincides with the intersection of the circles described in 4.4 as depicted in Figure 4.11.

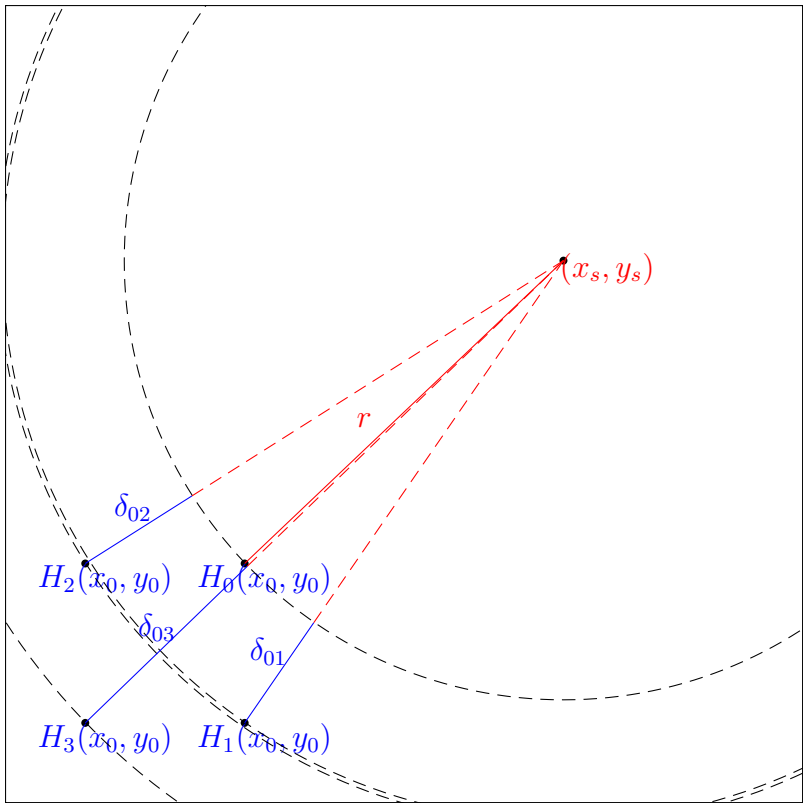


Figure 4.10: The non-linear system described by Equation 4.4. Variables in blue are known and variables in red are unknown.

The Matlab `fsolve` function can be applied to determine a solution for Equation 4.4. There is a subtle differences when solving the system directly using this approach. Matlab's `fsolve` requires an initialization point. In the case of the AIGL algorithm, the inverted circles intersection is used as the initialization point. The selection of an initial starting point for the routine and its variation are not as natural for NLSL compared to the AIGL algorithm solution. In practice, and at first glance, the conclusion might be that one can reasonably propose an initial starting point by considering the operational boundaries for an AUV deployment. However, for the

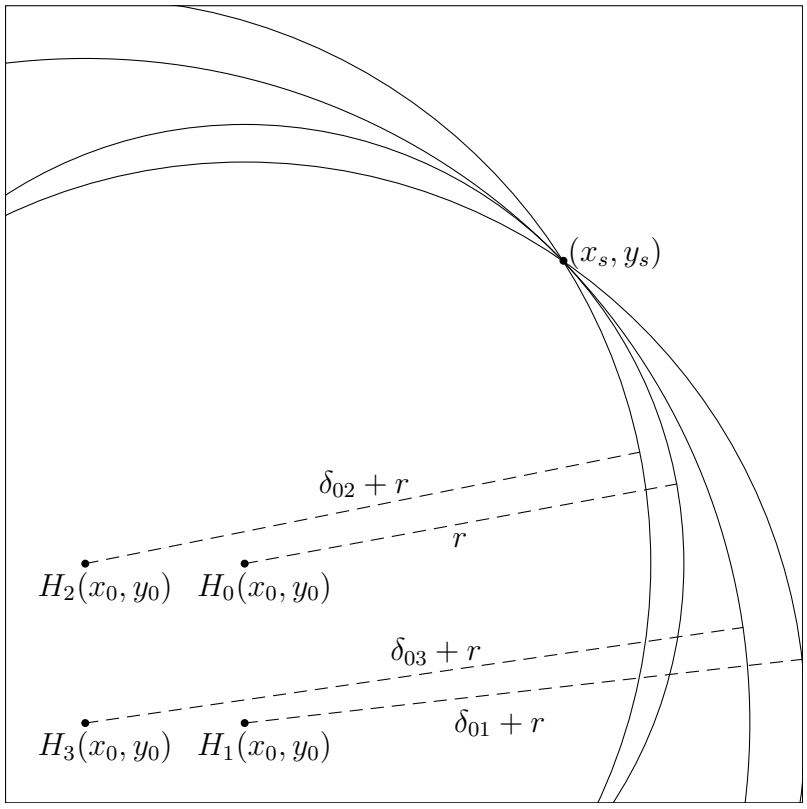


Figure 4.11: The solution to the non-linear system described by Equation 4.4 can be found by determining the intersection of circles.

evaluation purposes of this thesis, the centre of the receiving array is selected as the initialization point.

Table 4.2 contains the results of the direct method solution of the non-linear system.

| Source | $x$ | $\text{Error}_x$ | $y$ | $\text{Error}_y$ | Range | $\text{Error}_{Range}$ |
|---|---|---|---|---|---|---|
| Actual | 20000 | 0 | 10000 | 0 | 22092.532 | 0 |
| AIGL | 20000 | $1.35 \times 10^{-7}$ | 10000 | $6.75 \times 10^{-8}$ | 22092.532 | $1.51 \times 10^{-7}$ |
| NLSL | 20000 | $1.23 \times 10^{-7}$ | 10000 | $6.07 \times 10^{-8}$ | 22092.532 | $1.37 \times 10^{-7}$ |

Table 4.2: Position estimate error and range estimate error for the AIGL and NLSL. All units are in metres.

**Algorithm 6** NLSL

**procedure** BOXCENTRE($H_0, H_1, H_2, H_3$) ▷ Centre of receiving array
$InitialSolution \leftarrow$ Result BOXCENTRE
$CircleSol_1 \leftarrow (\infty, \infty)$
$i \leftarrow 0$ ▷ Set counters
$j \leftarrow 1$
$minCircleSol_1 \leftarrow CircleSol_1$
**while** $\|minCircleSol_1 - SourceLocationPoint\| > \epsilon \wedge i < 100000$ **do**
▷ Can be used for simulation (i.e. SourceLocationPoint known)
    **procedure** ADVANCESEARCHSTANDARD($i, j, InitalSolutionCentre$)
    ▷ move $InitialSolution$ outward from axis catered at $BOXCENTRE$ axis by increment of $i$
    $InitialSolution \leftarrow$ ResultADVANCESEARCHSTANDARD
    **function** FSOLVE($H_0, H_1, H_2, H_3, \delta_{01}, \delta_{02}, \delta_{03}, InitialSolution$) ▷ FSOLVE applied to solve direct problem
    $CircleSol_1 \leftarrow$ ResultFSOLVE
    **if** $\|CircleSol_1 - SourceLocationPoint\| < \|minCircleSol_1 - SourceLocationPoint\|$ **then**
        $minCircleSol_1 \leftarrow CircleSol_1$
    $i \leftarrow i + 100$
    $j \leftarrow j + 1$
$CircleSol_1 \leftarrow minCircleSol_1$

**Algorithm 7** NLSL

**procedure** BOXCENTRE($H_0, H_1, H_2, H_3$) ▷ Centre of receiving array
$InitialSolution \leftarrow$ Result BOXCENTRE
$CircleSol_2 \leftarrow (\infty, \infty)$
$i \leftarrow 0$ ▷ Set counters
$j \leftarrow 1$
$iLimit \leftarrow iLimitThreshold$ ▷ Thresholds determine extensiveness of solution.
$\epsilon \leftarrow ErrorThreshold$
$a \leftarrow 1$ ▷ set loop variables
$b \leftarrow 0$
$c \leftarrow 0$
$minCircleSol_2 \leftarrow CircleSol_2$
$minErr_{total} \leftarrow \infty$
**while** $i < iLimit \wedge minErr_{total} > \epsilon$ **do**
    **function** FSOLVE($H_0, H_1, H_2, H_3, \delta_{01}, \delta_{02}, \delta_{03}, InitialSolution$)
    $CircleSol_2 \leftarrow$ Result FSOLVE
    **procedure** ADVANCESEARCHSTANDARD($i, j, InitialSolution$)
    **function** DIST($H_0, CircleSol_2$)
    $r \leftarrow$ ResultDIST
    **function** DIST($H_1, CircleSol_2$)
    $a \leftarrow$ ResultDIST
    **function** DIST($H_2, CircleSol_2$)
    $b \leftarrow$ ResultDIST
    **function** DIST($H_3, CircleSol_2$)
    $c \leftarrow$ ResultDIST
    $Err_a \leftarrow |(a - (r + \delta_{01})|$
    $Err_b \leftarrow |(b - (r + \delta_{02})|$
    $Err_c \leftarrow |(c - (r + \delta_{03})|$
    $Err_{total} \leftarrow Err_a + Err_b + Err_c$
    **if** $Err_{total} < minErr_{total}$ **then**
        $minErr_{total} \leftarrow Err_{total}$
        $minCircleSol_2 \leftarrow CircleSol_2$
    $i \leftarrow i + 100$
    $j \leftarrow j + 1$
$CircleSol_2 \leftarrow minCircleSol_2$

# Chapter 5

# Simulation I: Numerical Error

The single-beacon, single- hydrophone algorithm evaluation simulation results will be presented in this chapter. The performance of the two SBSH localization methods are compared in simulation to determine the accuracies of the implemented method using floating-point arithmetic and with rounding errors. The Apollonian inversion geometry localization and the non linear system localization will be applied using the receiving array described at the end of Chapter 3 for a comprehensive evaluation in simulation using Matlab. The precise locations of the receivers will be shifted slightly so that it is not strictly symmetrical. This addresses certain difficulties that occur as part of the algorithm implementation for AIGL. However, the general square, box-like geometry is maintained for the entirety of the simulation evaluation.

The following physical geometry-related details and parameters that will be varied as part of the simulation include:

1. The length and width of the simulation source location region;

2. The orientation of the receiving array relative to the source location region; and

3. The resolution of the source location region.

The ACENET computing cluster is used for simulations, specifically the Placentia heterogeneous Linux cluster which includes 3792 cores.[1] A source position estimate is generated for a range of simulated source locations and set of stationary receiver array locations. The simulation results in this section demonstrate the numerical error associated directly with the evaluation of the AIGL and NLSL algorithms for a set receiver location and array of possible source positions.

Two receiving array orientations are employed for the simulation, as shown in Figure 5.1. The standard square box arrangement is rotated by 45° in order to present a different orientation with respect to source locations. The source simulation region consists of 40 000 source locations. A positional estimate error is generated for each source location for both the AIGL and NLSL algorithm. The size of the resulting data set is manageable for plotting and visualization purposes. Error plots are included for both algorithms and their relative difference.

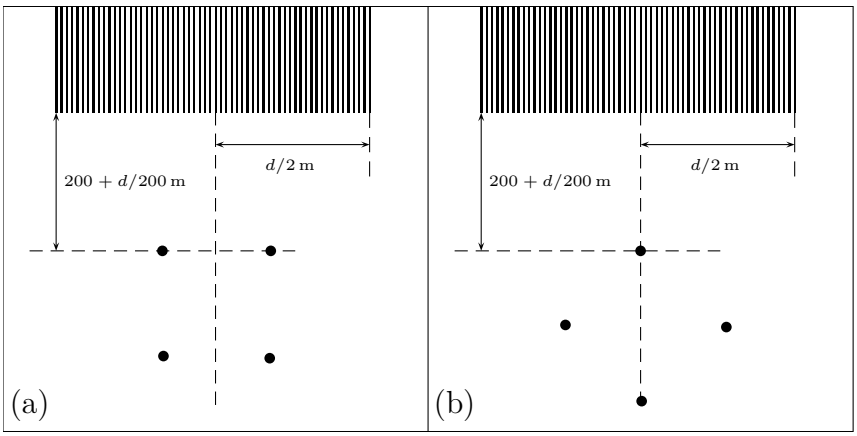


Figure 5.1: The two 100 m × 100 m receiving array configurations with respect to the simulated source region ($d \times d$): (a) standard and (b) rotated 45° (Not to scale).

The general method for simulation involves the application of the AIGL and

[1]Computational facilities are provided by ACENET, the regional high performance computing consortium for universities in Atlantic Canada. ACENET is funded by the Canada Foundation for Innovation, ACOA, and the provinces of Newfoundland and Labrador, Nova Scotia, and New Brunswick.

NLSL algorithms to an expanding sequence of source location regions. The region size will increase by a factor of 100, i.e. a factor of 10 in each dimension, in order to visualize the estimated position error of the algorithms for successively larger search areas. The simulation data set itself is maintained at a constant size. It consists of 40 000 points or source locations. The regions are classified as near, medium-near, medium and far field, see Table 5.1.

| | Scaling factor | Tx Region dimension | Approx. Rx Centreline loc. |
|---|---|---|---|
| Near | 1 | 200 m | 100 m |
| Medium-near | 10 | 2000 m | 1000 m |
| Medium | $10^2$ | 20 000 m | 10 000 m |
| Far | $10^3$ | 200 000 m | 100 000 m |

Table 5.1: Simulated source region designations and dimensions.

The position error will be plotted for both algorithms for visualization and comparison where:

$$Error_{position} = \sqrt{Error_x^2 + Error_y^2}.$$

Additionally, a statistical evaluation will be applied for both algorithms over the simulated source region. It is necessary to set several error thresholds within the computer code to determine when points are distinct or near zero. The same error thresholds are used for the evaluation of both algorithms ($\epsilon_{error} = 0.000001$) for consistency purposes. In the case of the NLSL this tolerance represents a 1 µm error. However, for AIGL $epsilon_{error}$ has no dimensions because it is being applied in the inversion space. The error was varied for both AIGL and NLSL during some limited preliminary investigatory simulations. There was not a significant improvement in the localization error but there was an increase in simulation run time.

Simulation times required to generate position estimates for both AIGL and

NLSL for this set of source locations can generally vary from approximately tens of minutes to tens of hours of processing time. There is variation in the pool of 32 processors being accessed for the simulations so the comprehensive comparison of processing times is not necessarily indicative of algorithm efficiency; however, CPU runtime is provided for each set of simulations to provide a sense of the computational effort as the scaling of the simulation increases. During initial simulations, slight improvements in code efficiency and a major change in code ordering translated into considerable time savings and improved results for the AIGL position estimates included in the thesis. The total CPU usage for simulations was 3.19 core years. A core year is the equivalent of running computation constantly on a CPU core for a period of one year.

## 5.1 Near field

The first simulation results for the near field region consist of source simulation in a $200\,\text{m} \times 200\,\text{m}$ region for a receiver array dimension of $100\,\text{m} \times 100\,\text{m}$. The minimum distance from the edge of the simulated source region to the nearest node in the receiver array is 201 m. The geometric centre of the receiver array coincides with a centreline for the source region. The corners of the array are slightly offset by at most a metre in longitude and/or a metre in latitude to ensure that the corners do not define a perfect square. The simulated position resolution is 1 m for the $200\,\text{m} \times 200\,\text{m}$ region.

The processing time for the near field source region was 39.84 min. The basic summary statistics regarding estimated position error are provided in Table 5.2 and Table 5.3. The frequency counts for different bounds of estimated position error is provided in Table 5.2.

The error threshold set for the software code the MATLAB `fsolve` function is

| | Estimated Position Error Frequency | | | | No |
|---|---|---|---|---|---|
| | $< 1\,\text{m}$ | $< 5\,\text{m}$ | $< 100\,\text{m}$ | $> 100\,\text{m}$ | Solution |
| *AIGL* | | | | | |
| Count | 39803 | 49 | 148 | 0 | 0 |
| | 99.51% | 0.12% | 0.37% | 0% | 0% |
| *NLSL* | | | | | |
| Count | 40000 | 0 | 0 | 0 | 0 |
| | 100 % | 0% | 0% | 0% | 0% |

Table 5.2: Near field position estimate error frequency counts.

arbitrarily set by the user to $\epsilon_{error} = 0.000001$. The effect within the code architecture is that the NLSL estimate position errors are generally forced to be less than $\epsilon_{error}$, but not exclusively. A comparable approach is applied to the `fsolve` function for solving the problem in inversion space in the context of AIGL. This does not strictly imply an AIGL estimate position with error less than $\epsilon_{error}$ post transformation from inversion space. It will be seen that as the source region increases in size, both algorithms suffer.

An overall implication is that the position estimate errors for both AIGL and NLSL can be very small relative to the size of the simulated source region, the receiver array dimension and the search resolution. A data transformation must be applied in order to reasonably visualize and apply descriptive statistics to the data set. For each data point $x_i$ in the simulated position error data set $X$, the transformation $z_i = \log(x_i/1\,\text{m})$ was applied.

A set of comprehensive three dimensional and two dimensional surface plots Figure 5.2 - 5.4 visualize the position error estimates for both AIGL, NLSL and their difference. Figures 5.2 and 5.3 show the error for AIGL and NLSL respectively. Figure 5.4 shows the relative difference in error for AIGL and NLSL.

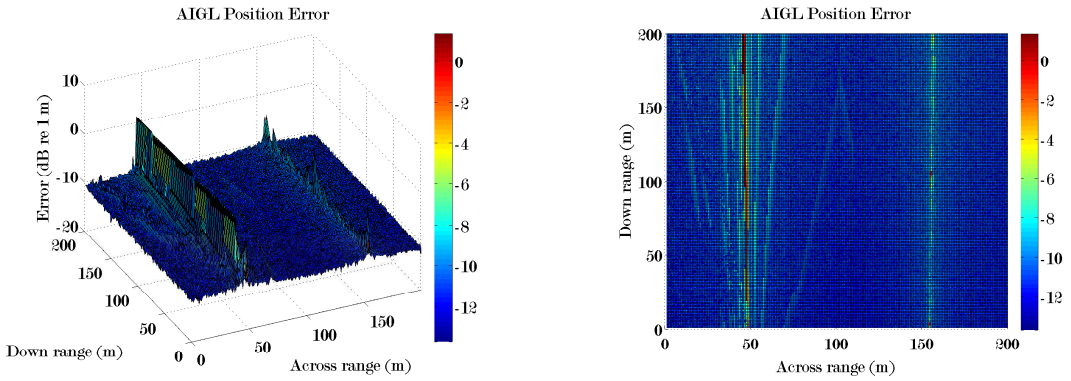


Figure 5.2: The positional estimate error for AIGL in the near field region.

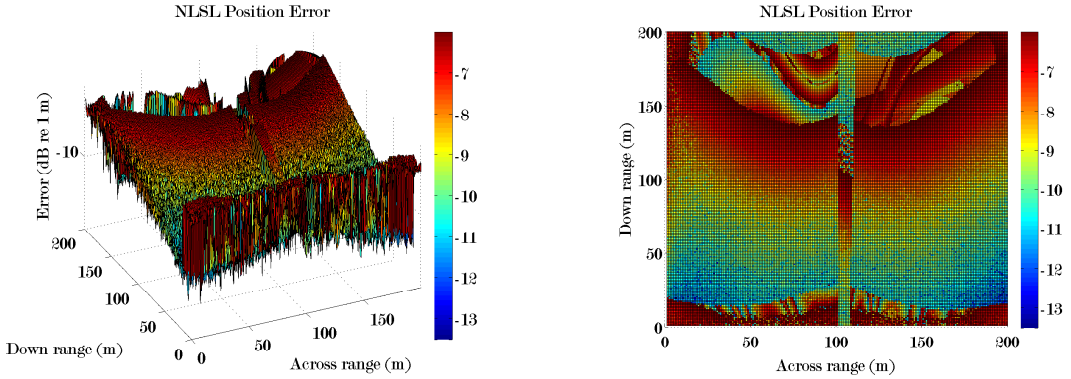


Figure 5.3: The positional estimate error for NLSL in the near field region.

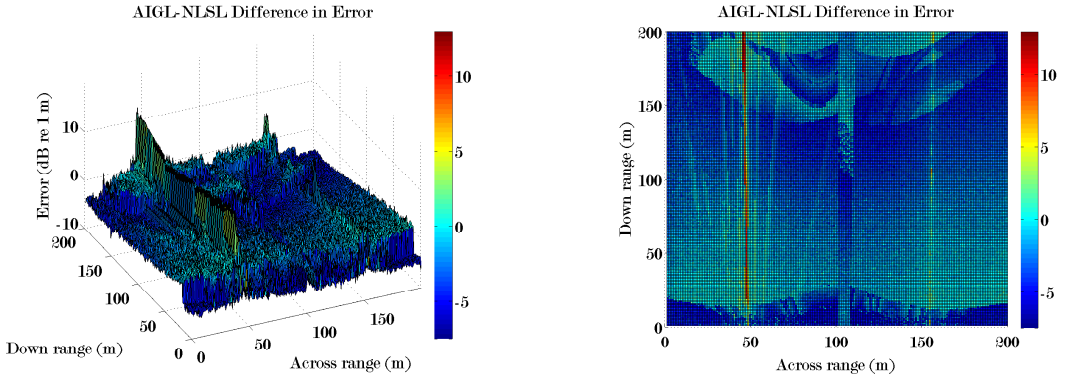


Figure 5.4: The positional estimate difference in error for AIGL and NLSL in the near field region.

The error statistics for AIGL and NLSL are summarized in Table 5.3. A histogram of the estimate error distributions is given in Figure 5.5.

| | Mean | Variance | Standard Deviation | Null Count |
|---|---|---|---|---|
| *AIGL* | -10.7558 | 1.4972 | 1.2236 | 0 |
| *NLSL* | -8.4618 | 2.5791 | 1.6060 | 0 |

Table 5.3: Near field AIGL and NLSL position estimate log error statistics.

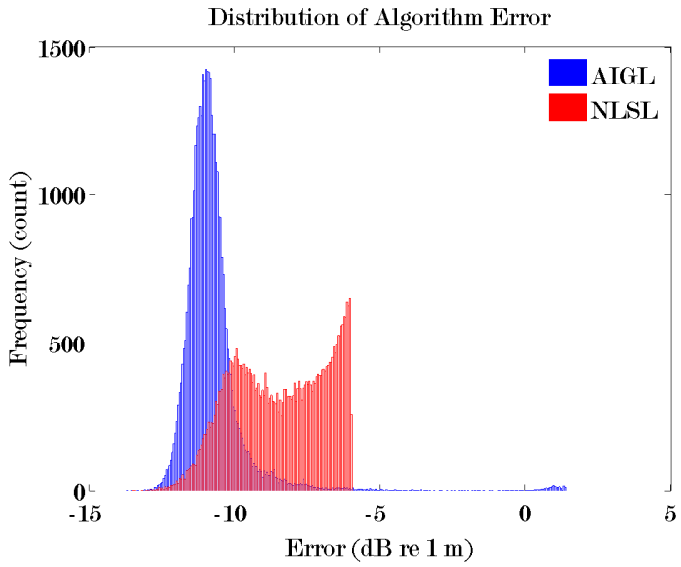


Figure 5.5: Distribution of the positional error for AIGL (blue) and NLSL (red) in the near field. The clipping of NLSL coincides with $\epsilon_{error}$.

The second set of near field simulations is configured with the receiver array rotated by 45° as shown in Figure 5.1 (b). Simulation runtime with the rotated array was 8.2 min. Summary statistics regarding estimated position error are provided in Table 5.4 and Table 5.5. The frequency counts for different bounds of estimated position error is provided in Table 5.4.

The set of comprehensive three dimensional and two dimensional surface plots Figure 5.6 - 5.8 visualize the position error estimates for both AIGL, NLSL and their

| | Estimated Position Error Frequency | | | | No |
|---|---|---|---|---|---|
| | $< 1\,\text{m}$ | $< 5\,\text{m}$ | $< 100\,\text{m}$ | $> 100\,\text{m}$ | Solution |
| *AIGL* | | | | | |
| Count | 40000 | 0 | 0 | 0 | 0 |
| | 100% | 0% | 0% | 0% | 0% |
| *NLSL* | | | | | |
| Count | 40000 | 0 | 0 | 0 | 0 |
| | 100% | 0% | 0% | 0% | 0% |

Table 5.4: Near field position estimate error frequency counts for rotated receiver array.

difference. Figures 5.6 and 5.7 show the error for AIGL and NLSL respectively. Figure 5.8 shows the relative difference in error for AIGL and NLSL.

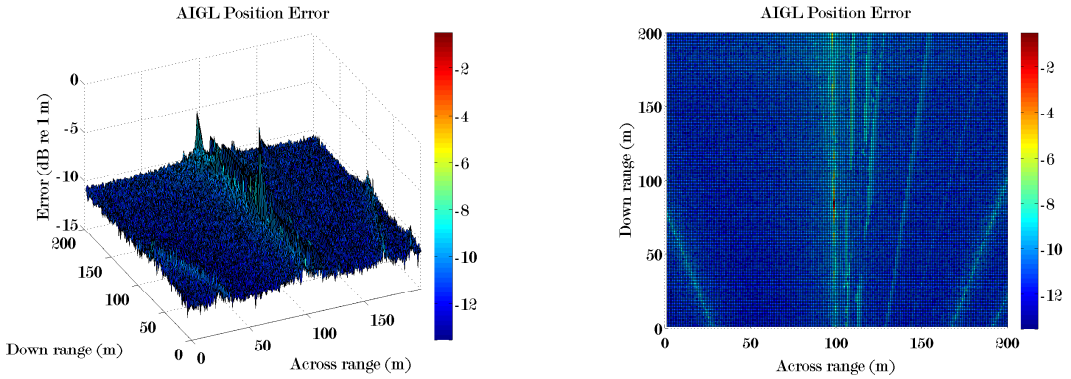


Figure 5.6: The positional estimate error for AIGL in the near field region with rotated receiver array.

The error statistics for AIGL and NLSL are summarized in Table 5.5. A histogram of the estimate error distributions is given in Figure 5.9.

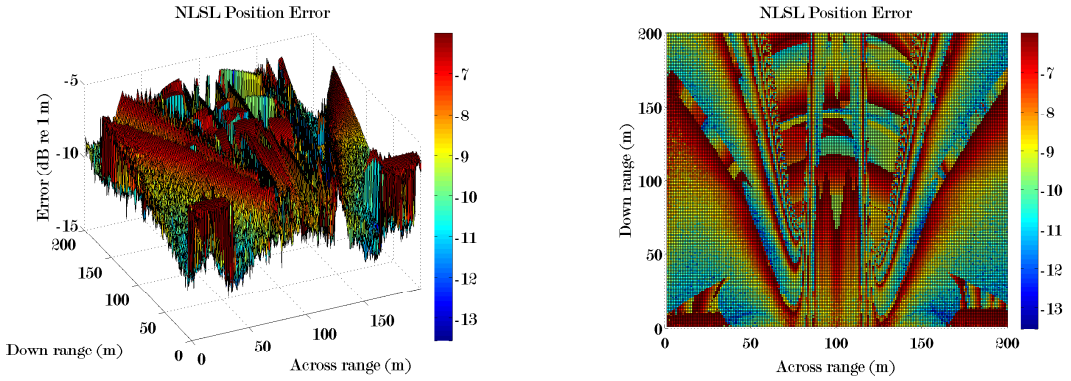


Figure 5.7: The positional estimate error for NLSL in the near field region with rotated receiver array.

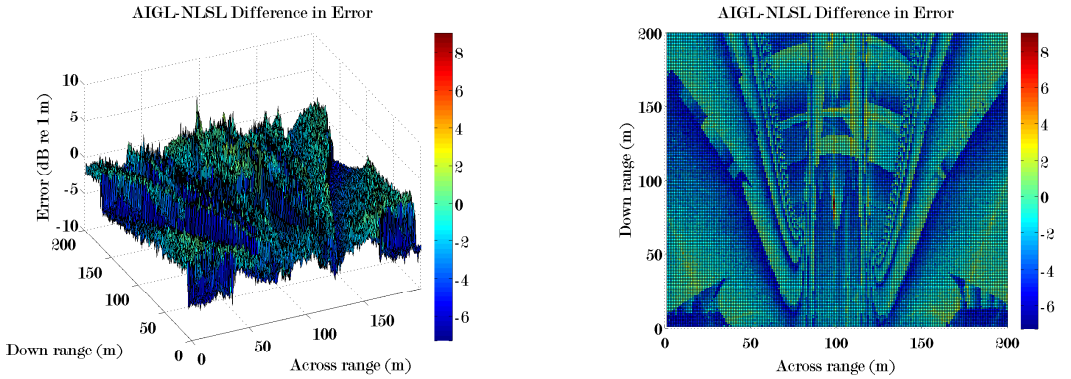


Figure 5.8: The positional estimate difference in error for AIGL and NLSL in the near field region with rotated receiver array.

| | Mean | Variance | Standard Deviation | Null Count |
|---|---|---|---|---|
| *AIGL* | -10.9583 | 0.4730 | 0.6878 | 0 |
| *NLSL* | -8.7129 | 2.5335 | 1.5917 | 0 |

Table 5.5: Near field AIGL and NLSL position estimate log error statistics for rotated receiver array.

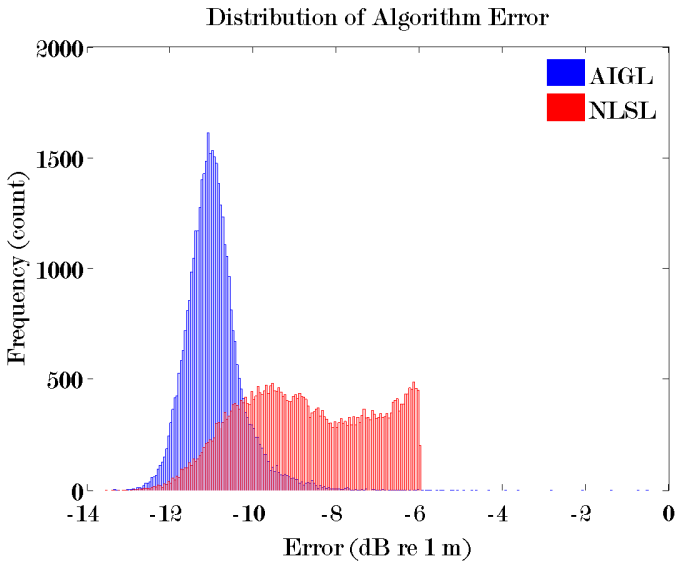


Figure 5.9: Distribution of the positional error for AIGL (blue) and NLSL (red) in the near field with rotated receiver array.

## 5.2 Medium-near field

The near field simulated source region dimensions are increased by an order in magnitude to 2000 m × 2000 m to represent the medium-near field source region. The receiver array dimension is maintained at 100 m × 100 m. The minimum distance from the edge of the simulated source region to the nearest node in the receiver array is 210 m. The geometric centre of the receiver array coincides with a centreline for the source region. The corners of the array are slightly offset by at most a metre in longitude and/or a metre in latitude to ensure that the corners do not define a perfect square. Generally, the arrangement is consistent with the configuration described in Figure 5.1. The simulated position resolution is 10 m for the medium-near field.

The processing time for the near field source region was 31.49 min. The basic summary statistics regarding estimated position error are provided in Table 5.6 and Table 5.7. The frequency counts for different bounds of estimated position error is provided in Table 5.6.

| | Estimated Position Error Frequency | | | | No |
|---|---|---|---|---|---|
| | $< 1\,\text{m}$ | $< 5\,\text{m}$ | $< 100\,\text{m}$ | $> 100\,\text{m}$ | Solution |
| *AIGL* | | | | | |
| Count | 39899 | 7 | 57 | 37 | 0 |
| | 99.748% | 0.018% | 0.143% | 0.093% | 0% |
| *NLSL* | | | | | |
| Count | 40000 | 0 | 0 | 0 | 0 |
| | 100 % | 0% | 0% | 0% | 0% |

Table 5.6: Medium-near field position estimate error frequency counts.

The set of comprehensive three dimensional and two dimensional surface plots Figure 5.10 - 5.12 visualize the position error estimates for both AIGL, NLSL and their difference for the medium field. Figures 5.10 and 5.11 show the error for AIGL and NLSL respectively. Figure 5.12 shows the relative difference in error for AIGL and NLSL.

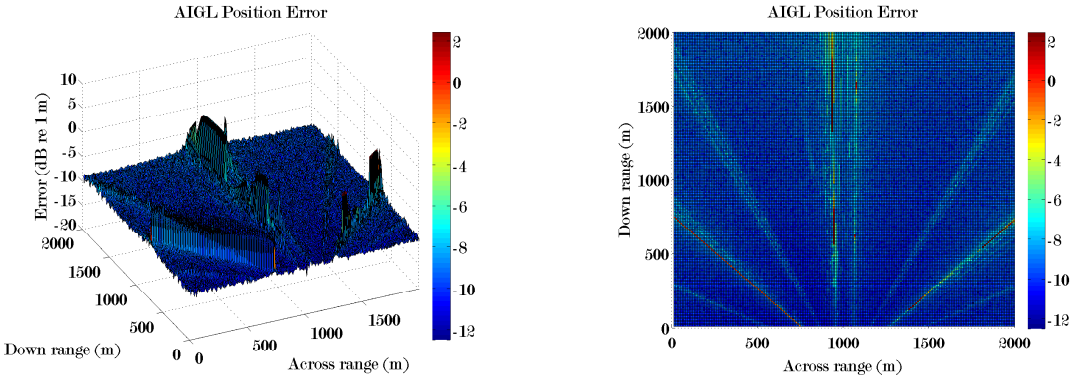


Figure 5.10: The positional estimate error for AIGL in the medium-near field region.

The error statistics for AIGL and NLSL are summarized in Table 5.7. A histogram of the estimate error distributions is given in Figure 5.13.

The second set of simulations for the medium-near field with a rotated receiver array show improved results for the AIGL similar to the near field simulations. Sim-

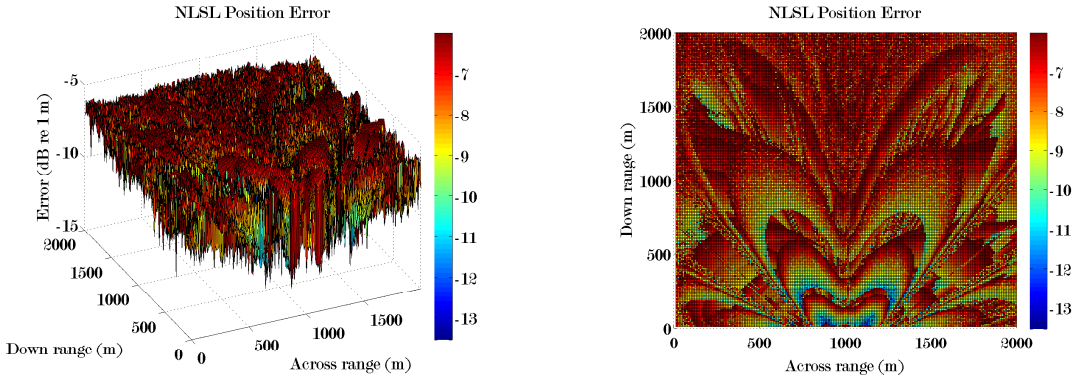


Figure 5.11: The positional estimate error for NLSL in the medium-near field region.

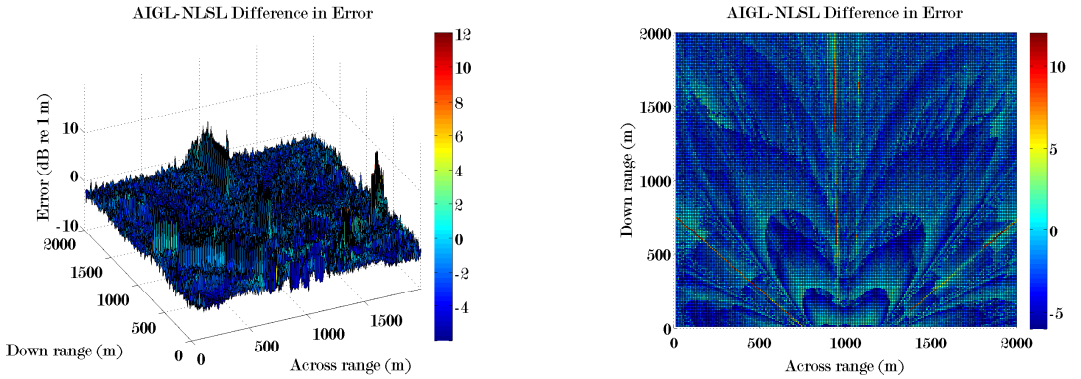


Figure 5.12: The positional estimate difference in error for AIGL and NLSL in the medium-near field region.

| | Mean | Variance | Standard Deviation | Null Count |
|---|---|---|---|---|
| *AIGL* | -9.4168 | 1.0914 | 1.0447 | 0 |
| *NLSL* | -7.4437 | 1.2855 | 1.1338 | 0 |

Table 5.7: Medium-near field AIGL and NLSL position estimate log error statistics.

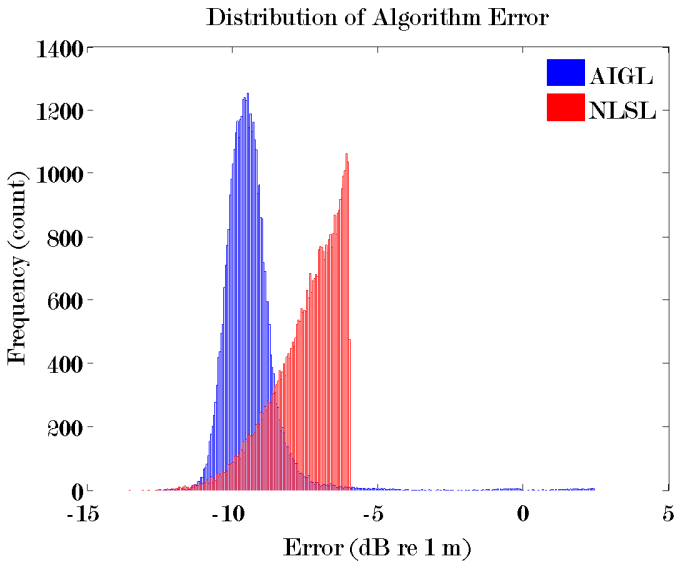


Figure 5.13: Distribution of the positional error for AIGL (blue) and NLSL (red) in the medium-near field.

ulation runtime with the rotated array was 29.06 min. The basic summary statistics regarding estimated position error are provided in Table 5.8 and Table 5.9. The frequency counts for different bounds of estimated position error is provided in Table 5.8.

The set of comprehensive three dimensional and two dimensional surface plots Figure 5.14 - 5.16 visualize the position error estimates for both AIGL, NLSL and their difference. Figures 5.14 and 5.15 show the error for AIGL and NLSL respectively. Figure 5.16 shows the relative difference in error for AIGL and NLSL.

The error statistics for AIGL and NLSL are summarized in Table 5.9. A histogram of the estimate error distributions is given in Figure 5.17.

| | Estimated Position Error Frequency | | | | No |
|---|---|---|---|---|---|
| | $< 1$ m | $< 5$ m | $< 100$ m | $> 100$ m | Solution |
| *AIGL* | | | | | |
| Count | 39966 | 3 | 21 | 10 | 0 |
| | 99.915 % | 0.008% | 0.053% | 0.025% | 0% |
| *NLSL* | | | | | |
| Count | 40000 | 0 | 0 | 0 | 0 |
| | 100 % | 0% | 0% | 0% | 0% |

Table 5.8: Medium-near field position estimate error frequency counts for rotated receiver array.

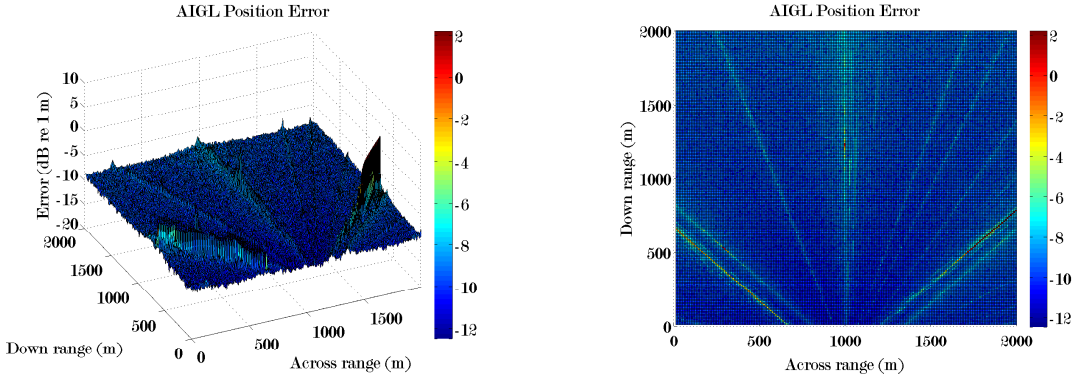


Figure 5.14: The positional estimate error for AIGL in the medium-near field region with rotated receiver array.

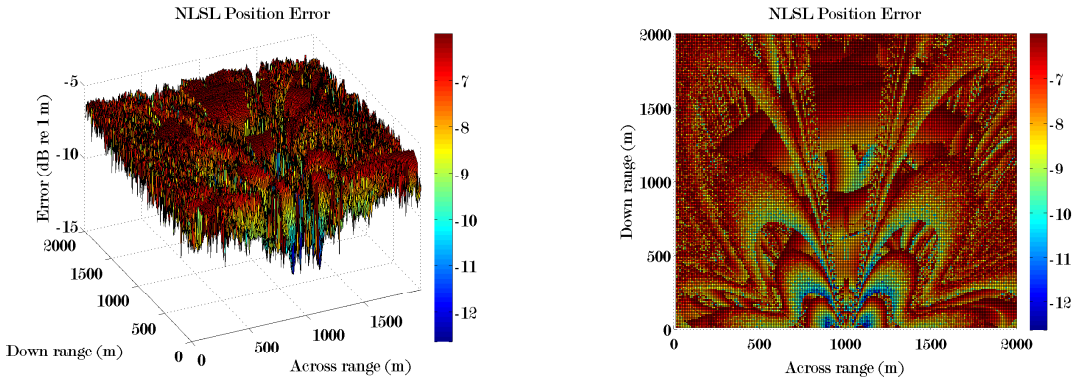


Figure 5.15: The positional estimate error for NLSL in the medium-near field region with rotated receiver array.

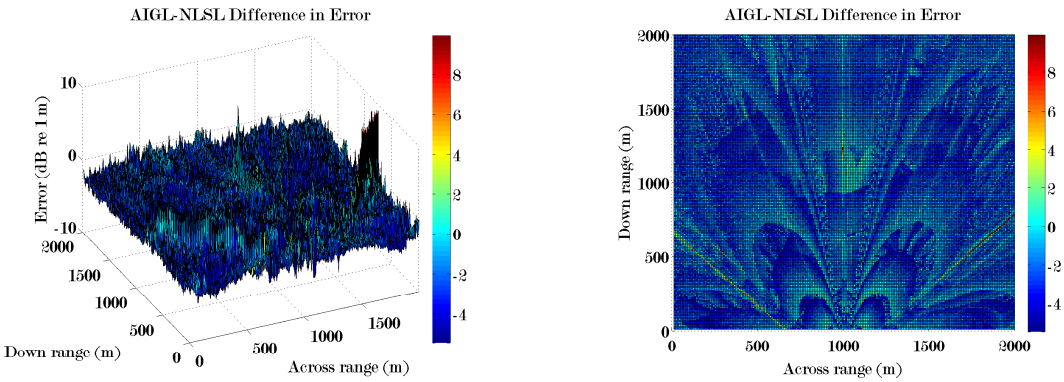


Figure 5.16: The positional estimate difference in error for AIGL and NLSL in the medium-near field region with rotated receiver array.

| | Mean | Variance | Standard Deviation | Null Count |
|---|---|---|---|---|
| *AIGL* | -9.4478 | 0.6642 | 0.8150 | 0 |
| *NLSL* | -7.3514 | 1.0620 | 1.0305 | 0 |

Table 5.9: Medium-near field AIGL and NLSL position estimate log error statistics for rotated receiver array.

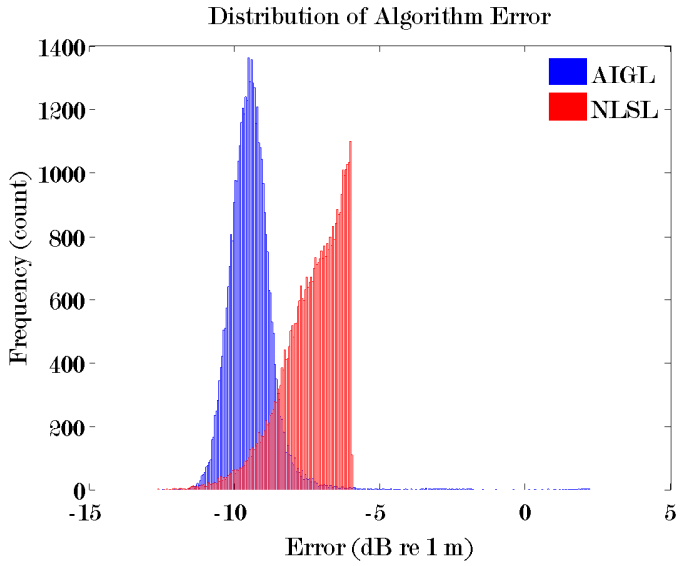


Figure 5.17: Distribution of the positional error for AIGL (blue) and NLSL (red) in the medium-near field with rotated receiver array.

## 5.3 Medium field

The simulated source region dimensions are increased by an order in magnitude to 20 km × 20 km. The receiver array dimension is maintained at 100 m × 100 m. The minimum distance from the edge of the simulated source region to the nearest node in the receiver array is 300 m. The geometric centre of the receiver array coincides with a centreline for the source region. The corners of the array slightly offset by at most a metre in longitude and/or a metre in latitude to ensure that the corners do not define a perfect square. Generally, the arrangement is consistent with the configuration described in Figure 5.1. The simulated position resolution is increased to 100 m for the medium field. The processing time for the medium field source region was 1.24 h. The statistics regarding estimated position error are provided in Table 5.10 and Table 5.11. The frequency counts for different bounds of estimated position error is provided in Table 5.10.

| | Estimated Postion Error Frequency | | | | No |
|---|---|---|---|---|---|
| | $< 1$ m | $< 5$ m | $< 100$ m | $> 100$ m | Solution |
| *AIGL* | | | | | |
| Count | 39861 | 6 | 6 | 21 | 106 |
| | 99.653% | 0.015% | 0.015% | 0.053% | 0.265% |
| *NLSL* | | | | | |
| Count | 40000 | 0 | 0 | 0 | 0 |
| | 100 % | 0% | 0% | 0% | 0% |

Table 5.10: Medium field position estimate error frequency counts.

The set of comprehensive three dimensional and two dimensional surface plots Figure 5.18 - 5.20 visualize the position error estimates for both AIGL, NLSL and their difference for the medium field. Figures 5.18 and 5.19 show the error for AIGL and NLSL respectively. Figure 5.20 shows the relative difference in error for AIGL

and NLSL.

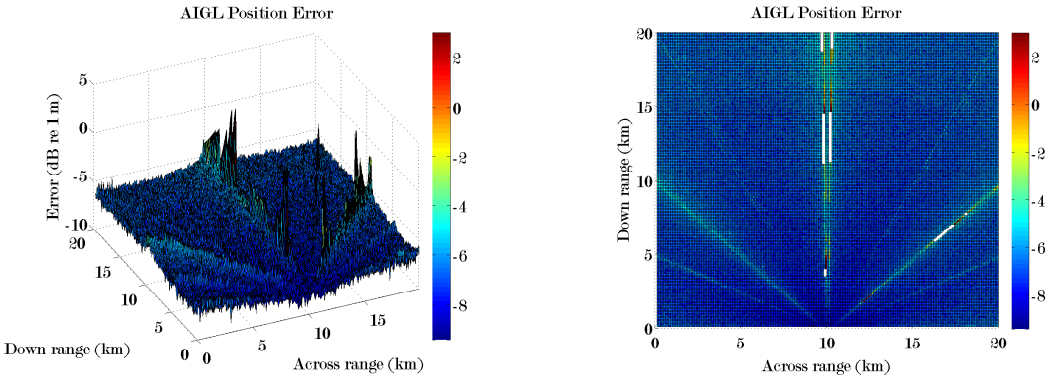


Figure 5.18: The positional estimate error for AIGL in the medium field region.

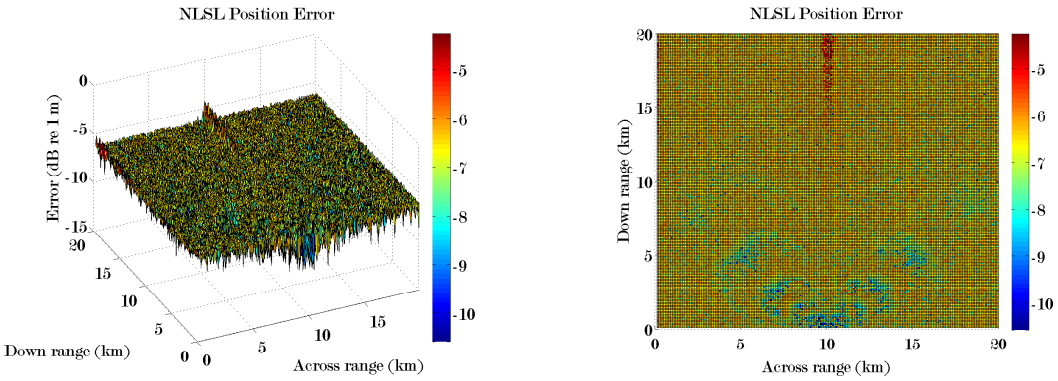


Figure 5.19: The positional estimate error for NLSL in the medium field region.

The error statistics for AIGL and NLSL are summarized in Table 5.11. A histogram of the estimate error distributions is given in Figure 5.21.

The second set of simulations for the medium field with a rotated receiver array show improved results for the AIGL much like the near field simulations. Simulation runtime with the rotated array was 1.16 h. The basic summary statistics regarding estimated position error are provided in Table 5.12 and Table 5.13. The frequency counts for different bounds of estimated position error is provided in Table 5.12.

The set of comprehensive three dimensional and two dimensional surface plots

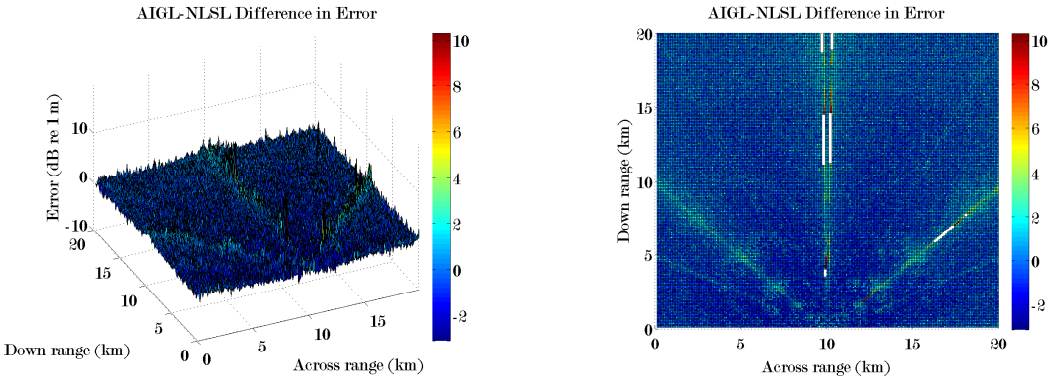


Figure 5.20: The positional estimate difference in error for AIGL and NLSL in the medium field region.

| | Mean | Variance | Standard Deviation | Null Count |
|---|---|---|---|---|
| *AIGL* | -6.7478 | 0.5805 | 0.7619 | 106 |
| *NLSL* | -6.5973 | 0.3359 | 0.5796 | 0 |

Table 5.11: Medium field AIGL and NLSL position estimate log error statistics.

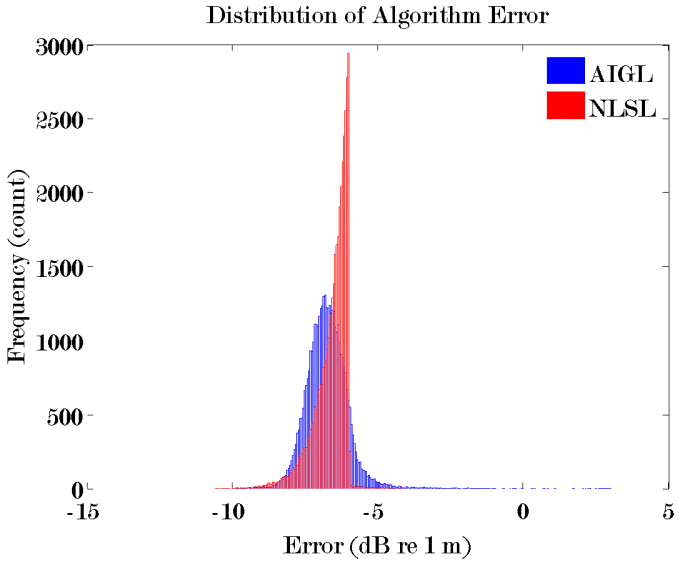


Figure 5.21: Distribution of the positional error for AIGL (blue) and NLSL (red) in the medium field.

| | Estimated Postion Error | | | | No |
|---|---|---|---|---|---|
| | $< 1\,\mathrm{m}$ | $< 5\,\mathrm{m}$ | $< 100\,\mathrm{m}$ | $> 100\,\mathrm{m}$ | Solution |
| *AIGL* | | | | | |
| Count | 39991 | 2 | 1 | 6 | 0 |
| | 99.978 % | 0.005% | 0.003% | 0.015% | 0% |
| *NLSL* | | | | | |
| Count | 40000 | 0 | 0 | 0 | 0 |
| | 100 % | 0% | 0% | 0% | 0% |

Table 5.12: Medium field position estimate error frequency counts for rotated receiver array.

Figure 5.22 - 5.24 visualize the position error estimates for both AIGL, NLSL and their difference for the medium field. Figures 5.22 and 5.23 show the error for AIGL and NLSL respectively. Figure 5.24 shows the relative difference in error for AIGL and NLSL.

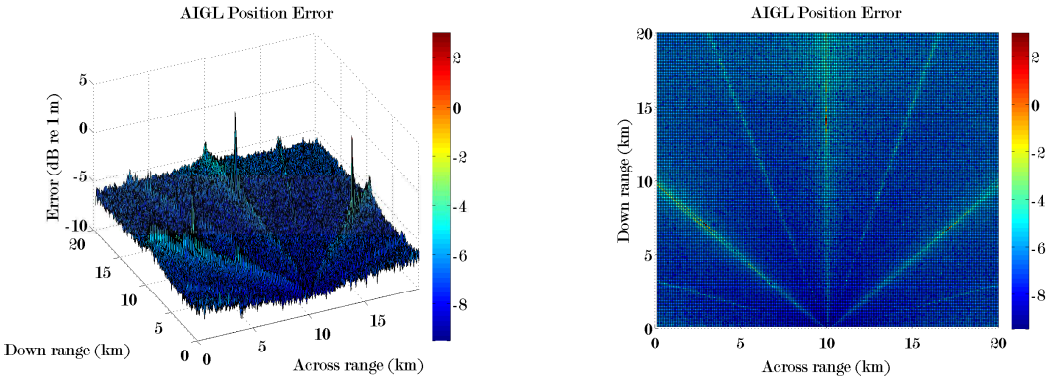


Figure 5.22: The positional estimate error for AIGL in the medium field region with rotated receiver array.

The error statistics for AIGL and NLSL are summarized in Table 5.13. A histogram of the estimate error distributions is given in Figure 5.25.

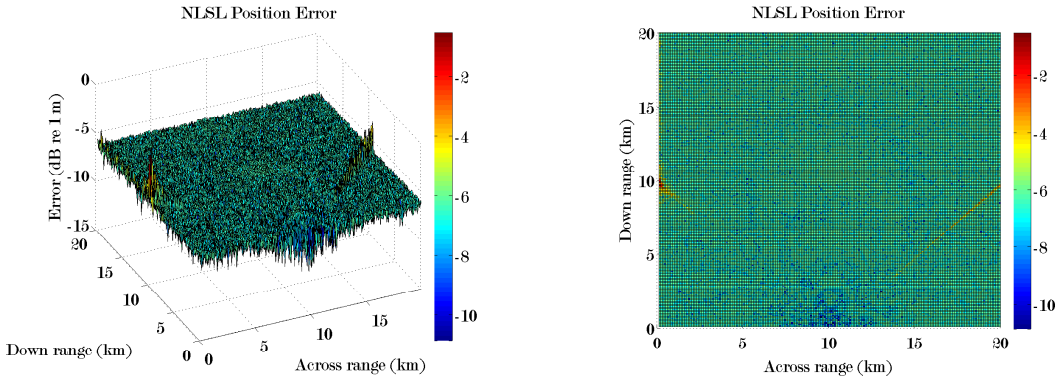


Figure 5.23: The positional estimate error for NLSL in the medium field region with rotated receiver array.

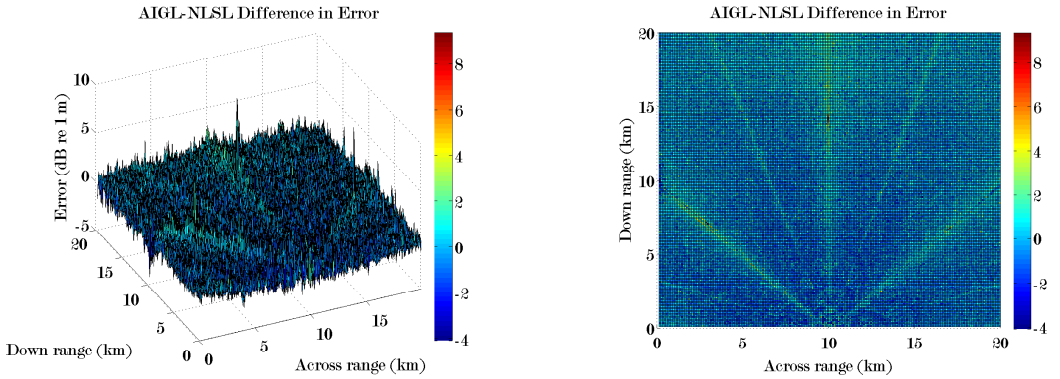


Figure 5.24: The positional estimate difference in error for AIGL and NLSL in the medium field region with rotated receiver array.

| | Mean | Variance | Standard Deviation | Null Count |
|---|---|---|---|---|
| *AIGL* | -6.7168 | 0.4766 | 0.6904 | 0 |
| *NLSL* | -6.5089 | 0.2713 | 0.5209 | 0 |

Table 5.13: Medium field AIGL and NLSL position estimate log error statistics for rotated receiver array.

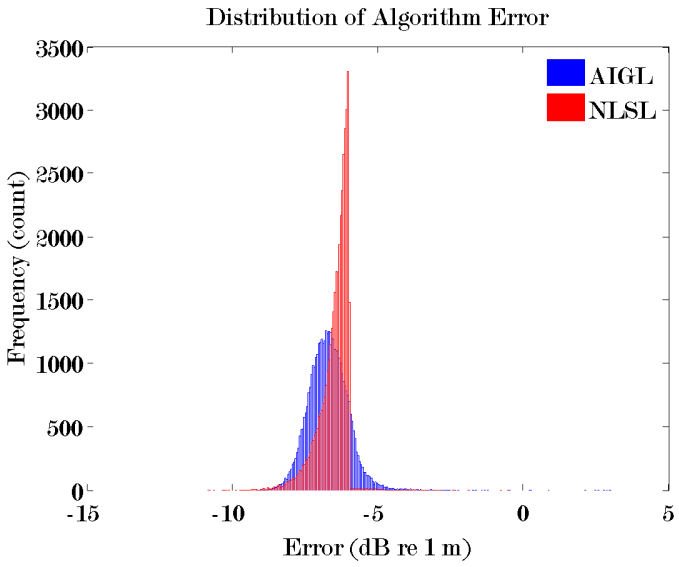


Figure 5.25: Distribution of the positional error for AIGL (blue) and NLSL (red) in the medium field with rotated receiver array.

## 5.4 Far field

The simulated source region dimensions are increased by an order in magnitude to 200 km × 200 km. The receiver array dimension is maintained at 100 m × 100 m. The minimum distance from the edge of the simulated source region to the nearest node in the receiver array is 1200 m. The geometric centre of the receiver array coincides with a centreline for the source region. The corners of the array slightly offset by at most a metre in longitude and/or a metre in latitude to ensure that the corners do not define a perfect square. Generally, the arrangement is consistent with the configuration described in Figure 5.1. The simulated position resolution is 1000 m for the far field.

The processing time for the far field source region was 11.07 h. The basic summary statistics regarding estimated position error are provided in Table 5.14 and Table 5.15. The frequency counts for different bounds of estimated position error is provided in Table 5.14.

| | Estimated Postion Error Frequency | | | | No |
|---|---|---|---|---|---|
| | $< 1\,\text{m}$ | $< 5\,\text{m}$ | $< 100\,\text{m}$ | $> 100\,\text{m}$ | Solution |
| *AIGL* | | | | | |
| Count | 39795 | 13 | 16 | 5 | 171 |
| | 99.488% | 0.033% | 0.040% | 0.013% | 0.428% |
| *NLSL* | | | | | |
| Count | 38038 | 635 | 877 | 438 | 12 |
| | 95.095% | 1.588% | 2.193% | 1.095% | 0.030% |

Table 5.14: Far field position estimate error frequency counts.

The set of comprehensive three dimensional and two dimensional surface plots Figure 5.26 - 5.28 visualize the position error estimates for both AIGL, NLSL and their difference for the far field. Figures 5.26 and 5.27 show the error for AIGL and NLSL respectively. Figure 5.28 shows the relative difference in error for AIGL and NLSL.

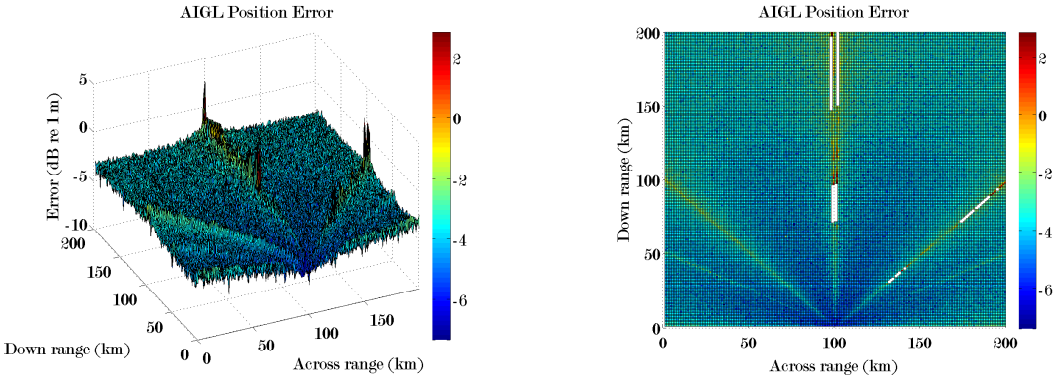


Figure 5.26: The positional estimate error for AIGL in the far field region.

The error statistics for AIGL and NLSL are summarized in Table 5.15. A histogram of the estimate error distributions is given in Figure 5.29.

The second set of simulations for the far field with a rotated receiver follow this section. Simulation runtime with the rotated array was 14.94 h. The basic statistics

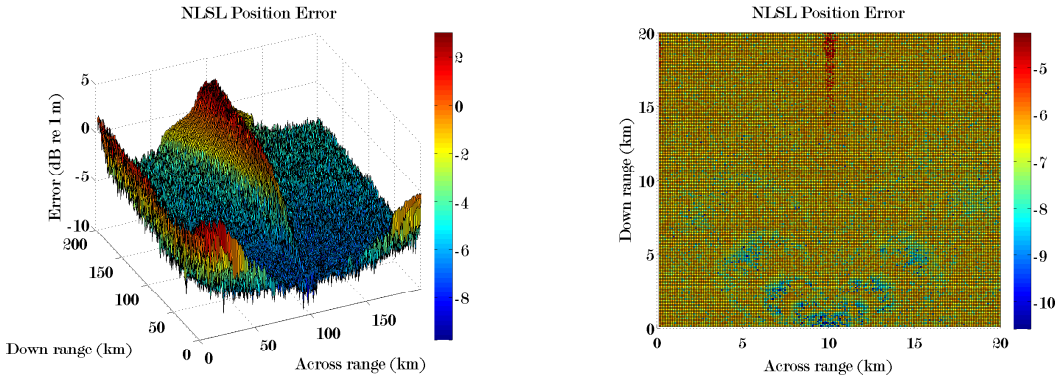


Figure 5.27: The positional estimate error for NLSL in the far field region.

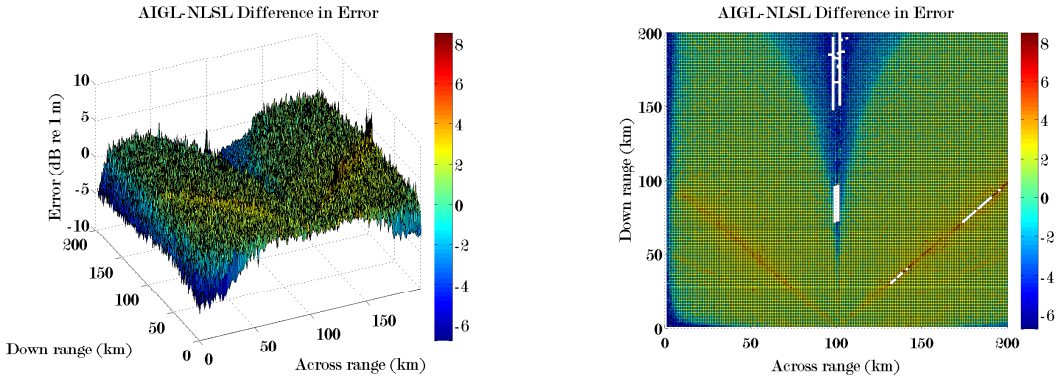


Figure 5.28: The positional estimate difference in error for AIGL and NLSL in the far field region.

| | Mean | Variance | Standard Deviation | Null Count |
|---|---|---|---|---|
| *AIGL* | -3.8360 | 0.4461 | 0.6679 | 171 |
| *NLSL* | -4.7006 | 4.0941 | 2.0234 | 12 |

Table 5.15: Far field AIGL and NLSL position estimate log error statistics.

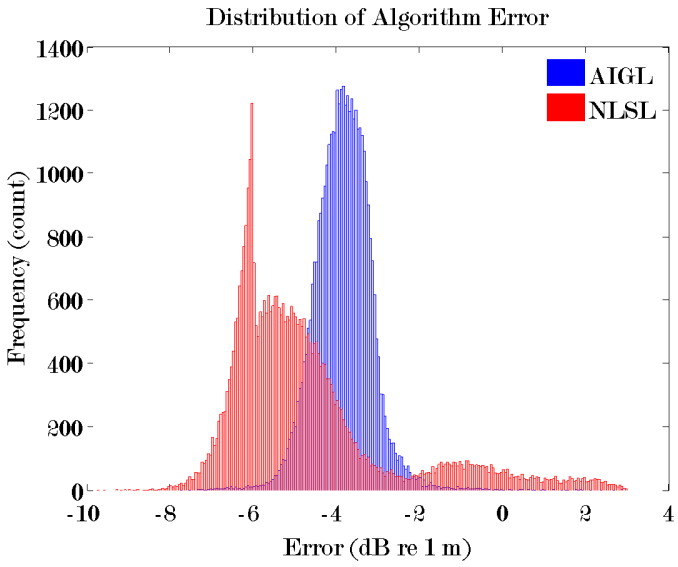


Figure 5.29: Distribution of the positional error for AIGL (blue) and NLSL (red) in the far field.

regarding estimated position error are provided in Table 5.16 and Table 5.17. The frequency counts for different bounds of estimated position error is provided in Table 5.16.

The set of comprehensive three dimensional and two dimensional surface plots Figure 5.30 - 5.32 visualize the position error estimates for both AIGL, NLSL and their difference for the far field. Figures 5.30 and 5.31 show the error for AIGL and NLSL respectively. Figure 5.32 shows the relative difference in error for AIGL and NLSL.

The error statistics for AIGL and NLSL are summarized in Table 5.17. A histogram of the estimate error distributions is given in Figure 5.33.

| | Estimated Postion Error | | | | No |
|---|---|---|---|---|---|
| | $< 1\,\text{m}$ | $< 5\,\text{m}$ | $< 100\,\text{m}$ | $> 100\,\text{m}$ | Solution |
| *AIGL* | | | | | |
| Count | 39965 | 4 | 8 | 3 | 20 |
| | 99.913% | 0.010% | 0.020% | 0.008% | 0.050% |
| *NLSL* | | | | | |
| Count | 38453 | 325 | 931 | 291 | 0 |
| | 96.133% | 0.813% | 2.328% | 0.728% | 0% |

Table 5.16: Far field position estimate error frequency counts for rotated receiver array.

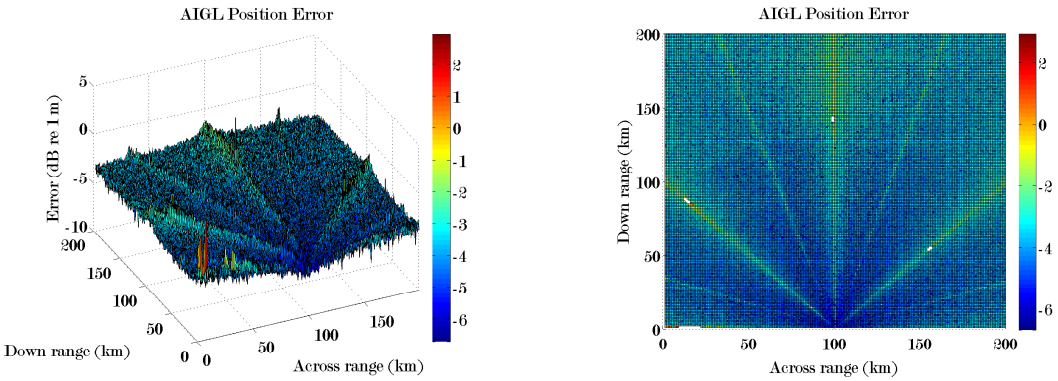


Figure 5.30: The positional estimate error for AIGL in the far field region with rotated receiver array.

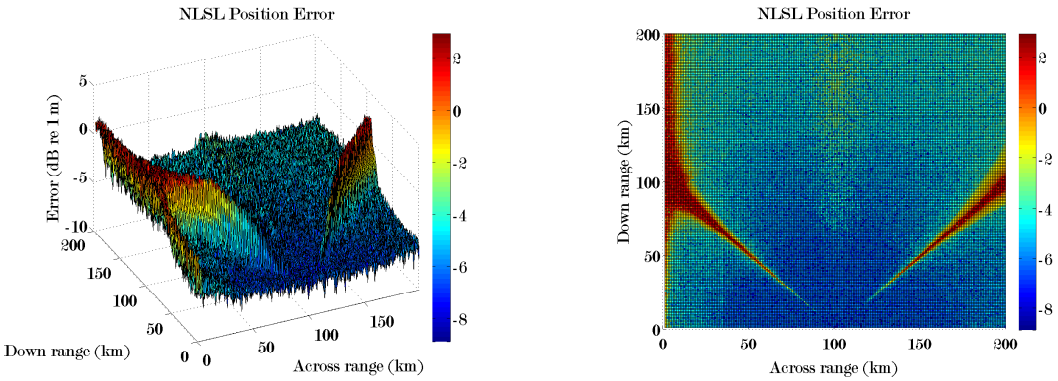


Figure 5.31: The positional estimate error for NLSL in the far field region with rotated receiver array.

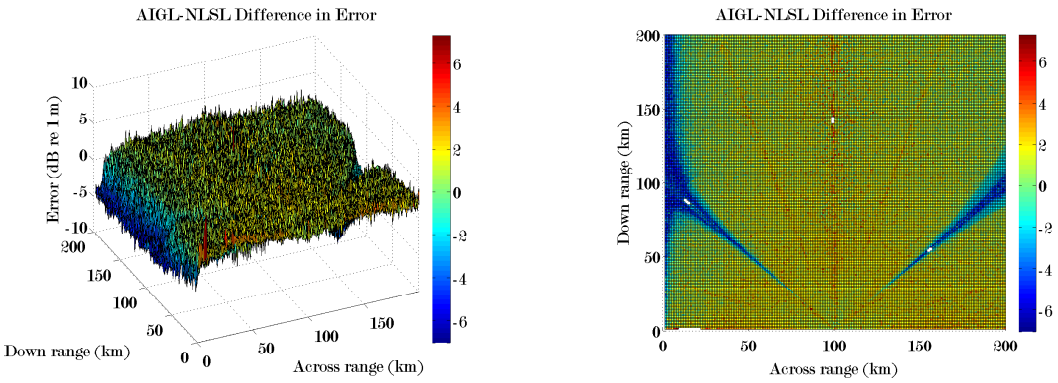


Figure 5.32: The positional estimate difference in error for AIGL and NLSL in the far field region with rotated receiver array.

| | Mean | Variance | Standard Deviation | Null Count |
|---|---|---|---|---|
| *AIGL* | -3.7882 | 0.4455 | 0.6675 | 20 |
| *NLSL* | -4.7273 | 3.0540 | 1.7476 | 0 |

Table 5.17: Far field AIGL and NLSL position estimate log error statistics for rotated receiver array.

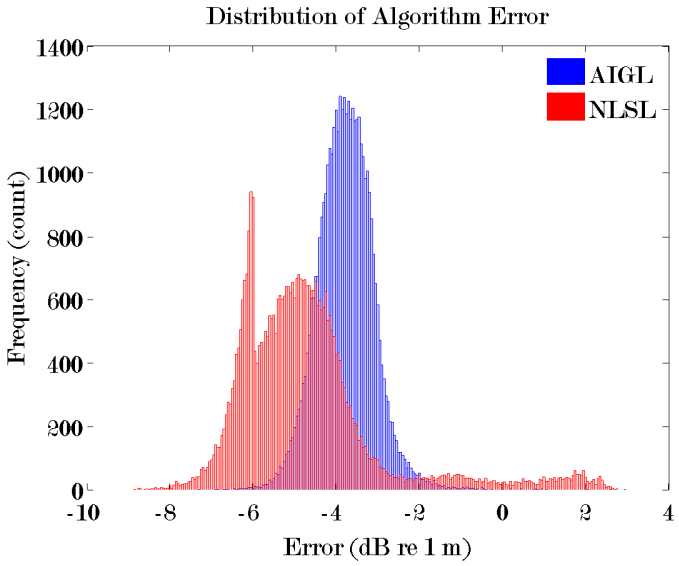


Figure 5.33: Distribution of the positional error for AIGL (blue) and NLSL (red) in the far field with rotated receiver array.

## 5.5 Discussion

The localization performance of each SBSH algorithm was evaluated for a set of 320 000 simulated source locations. In this section, no external error was included in simulation and only computational error inherent in the individual algorithm and its MATLAB implementation contribute to the localization error. Table 5.18 contains the position estimate separated into range frequency.

| | Simulation I Est. Postion Error Freq. | | | | No |
|---|---|---|---|---|---|
| | $< 1$ m | $< 5$ m | $< 100$ m | $> 100$ m | Solution |
| *AIGL* | | | | | |
| Count | 319280 | 84 | 257 | 82 | 297 |
| | 99.775% | 0.0263% | 0.0803% | 0.0256% | 0.0928% |
| *NLSL* | | | | | |
| Count | 316491 | 960 | 1808 | 729 | 12 |
| | 98.903% | 0.3000% | 0.5650% | 0.2278% | 0.0038% |

Table 5.18: Summary frequency counts of the position estimate error using simulated measurement error.

If we consider successful source location to be localizing the source to within 100 m, i.e. a practical distance to locate an AUV beneath ice using a low cost ROV then generally, both SBSH algorithm implementations, AIGL and NLSL, can successfully locate a simulated source in the absence of external error. These simulation results could be improved by decreasing the $\epsilon_{error} = 0.000001$ within the SBSH code. However, the cost of reducing $\epsilon_{error}$ is increased processing time. The given error level was adequate to provide quality localization results given the ACENET resources (CPU availability) and current simulation CPU run time.

On average, the AIGL algorithm has better localization results compared than the NLSL algorithm for the near field, medium-near field and medium field regions.

The AIGL has a lower mean error (log), see Tables 5.3, 5.5, 5.7, 5.9, 5.11 and 5.13. The NLSL has a lower mean error (log) for a simulated source in the far field region, see Tables 5.15 and 5.17.

In all regions except the medium region, the standard deviation of the AIGL error is less than the standard deviation of the NLSL error. The AIGL error exhibits a standard normal distribution bell shape in each histogram. The effect of the $\epsilon_{error}$ is visible in the NLSL error distribution histograms. As the field region increases in size, the error trends predictably to the right, i.e. it increases, but it concentrates just below the $\epsilon_{error}$ threshold. Within the Matlab code, if the `fsolve` function fails to solve the NLSL version of the localization problem with a total 400 000 iterations spanning 1000 different initialization points, then it accepts the solution (source location estimate) with the minimum error. This particular scenario, when the NLSL fails to yield a solution with error under $\epsilon_{error}$, the code processing time for the software is longer. There is an order of magnitude increase in simulation run time from the medium field times of 1.24 h and 1.11 h to the far field times of 14.10 h and 14.94 h. This is largely due to the additional iterations required for generating the NLSL error minimum. The AIGL implementation does not exhibit a similar behaviour due to the natural choice for solver initialization points along the certain axes, recall Figure 4.5.

The mean error for the AIGL and NLSL algorithms increase gradually as the source location region expands. There is a general lifting of the three dimensional position error associated with each algorithm for the increasingly larger regions. The respective surfaces for both are visibly different. The individual AIGL error surfaces exhibit a noticeable sensitivity and degraded performance along certain lines in the simulated source location region. Recall the receiver array layout in Figure 5.1. The sections of noticeably higher error correspond to lines defined by each pair of points in the receiver array. Two lines are visible in Figure 5.2 which correspond to the two

lines defined by the point pairs on the right and left sides of the array. The slight difference in the ridge height in Figure 5.2 is due to the misalignment of the array receiver nodes to avoid absolute symmetry.

In Figure 5.10, these two lines coincide due to the increased region spacing and lower search resolution. Two additional increased error ridges appear at 45° that correspond to the lines arising from the diagonals within the receiving array.

The sensitivity is due to the relative location of the reference point $H_0$ and circle of inversion when source locations are along the lines defined as discussed. If the reference point $H_0$ is near the centre of inversion and the radius of inversion is large, then it will transform to a point $H_0'$ far from the origin defined by the inverted TDOA circles - the lines $\ell_2$ and $\ell_3$. The resulting circle tangent to $H_0'$, $\ell_2$ and $\ell_3$ is large. The larger its radius of curvature then there is an increase in the error associated with determining the points tangent to $\ell_2$ and $\ell_3$. Consequently, once those tangent points are transformed, then that error carries through to the final localization solution.

There are also spikes visible along the increased error ridges such as in Figure 5.26. These spikes arise when the inverted reference signal point $H_0'$ lies very close to one of the inverted TDOA circle lines $\ell_2$ or $\ell_3$. Assume without loss of generality, that the point $H_0'$ is too close to $\ell_2$. The code implementation of `fsolve` determines a tangent circle solution on the wrong bisecting line (Figure 4.5). In other words, if $H_0'$ is too close, it can be treated computationally as either on $\ell_2$ or on the wrong side of $\ell_2$. This will lead to a tangent circle solution centred along the wrong bisecting line. The end result is a compromised source location solution.

The geometric interpretation of the NLSL surfaces is not as interesting until one considers the far field region which is where the first features appear on the surface. The surfaces for the NLSL are interesting to look at, but the patterns and minor irregularities correspond to the enforced error threshold, variations in solver

initialization point and the relative magnitude of the error, i.e. it is small. The NLSL error surface is interesting in the far field. Pronounced features are clear on Figure 5.27 and Figure 5.31.

Consider the geometric illustration of the NLSL method (Figure 4.11). The high error ridging corresponds with areas of points that are generally equidistant from opposite sides of the receiver array. Without loss of generality, assume the source location is such that $\delta_{01} = 0$ and $\delta_{02} = \delta_{03}$. Then the intersections of the circles centred at $H_0$ and $H_2$ are similar to tangent points. The same is true for the intersection of the circles centred at $H_1$ and $H_3$. The net result is that the source location solution which is a point that numerically satisfies the condition of lying on all four circles, can be far from the actual source location.

Moreover, for very large distances between the source and the receiver array, the individual receiver array nodes will appear to converge. This will cause the circles in Figure 4.11 to appear concentric resulting in a much larger set of numerically suitable source locations and a greater error in NLSL determined source location.

A summary of the statistics for the SBSH simulation results is shown in Table 5.19.

| | Results of External Error | | | |
|---|---|---|---|---|
| | AIGL | | NLSL | |
| | Standard | Rotated | Standard | Rotated |
| Near | | | | |
| Mean | -10.76 | -10.96 | -8.46 | -8.71 |
| Std. Dev | 1.22 | 0.69 | 1.61 | 1.59 |
| % Success | 100.000% | 100.000% | 100.000% | 100.000% |
| Null count | 0 | 0 | 0 | 0 |
| Med-near | | | | |
| Mean | -9.42 | -9.45 | -7.44 | -7.35 |
| Std. Dev | 1.04 | 0.82 | 1.13 | 1.03 |
| % Success | 99.908% | 99.975% | 100.000% | 100.000% |
| Null count | 0 | 0 | 0 | 0 |
| Medium | | | | |
| Mean | -6.75 | -6.72 | -6.60 | -6.51 |
| Std. Dev | 0.76 | 0.69 | 0.58 | 0.52 |
| % Success | 99.683% | 99.985% | 100.000% | 100.000% |
| Null count | 106 | 0 | 0 | 0 |
| Far | | | | |
| Mean | -3.84 | -3.79 | -4.70 | -4.73 |
| Std. Dev | 0.67 | 0.67 | 2.02 | 1.75 |
| % Success | 99.560% | 99.943% | 98.875% | 99.273% |
| Null count | 171 | 20 | 12 | 0 |

Table 5.19: Simulation statistics for differing source locations regions: near field, medium-near field, medium field and far field.

# Chapter 6

# Simulation II: Measurement Error

An external error is incorporated into simulations for the results contained within this chapter and the next chapter. The external error represents the error not attributed to the algorithm implementation itself but rather the hardware used for data collection (beacons, receiver, acoustic signal channel variability due to environmental factors such as sound speed changes, etc.). This measurement error is added to the relative range values, $\delta_{01}, \delta_{02}, \delta_{03}$, used to generate the TDOA circles at $H_1, H_2, H_3$ respectively. The error is generated from independent, identically distributed gaussian random variables for each $\delta_{0i}$, as in [91]. The magnitude of the error is based on the published specifications for current commercial state of the art for acoustic localization hardware as shown in Table 6.1. The rationale is that the SBSH system should be source independent. The superior error specification is used for simulations to determine the optimal simulated system performance using the best available beacon technology for the SBSH application. This is not an exhaustive manufacturer or product list. It indicates the current specified accuracies of commercially available USBL and LBL products and is used to justify the selection of error for simulation purposes.

The simulation error used is $error_{sim} = 0.02\,\text{m}$ which corresponds to the cNode

| Manufacturer | Product | System frequency | Range | Spec. error |
|---|---|---|---|---|
| Edgetech ORE | 4380 Multibeacon | 21 kHz to 28 kHz | 2500 m | 0.075 m [1] |
| Edgetech ORE | BATS | 16 kHz to 30 kHz | 3300 m | 0.3 m |
| LinkQuest | TL10000HA | 8.4 kHz to 11.7 kHz | 11 000 m | 0.4 m |
| LinkQuest | TL5000HA | 14.2 kHz to 19.8 kHz | 5000 m | 0.3 m |
| LinkQuest | TL1500HA | 31.0 kHz to 43.2 kHz | 1000 m | 0.2 m |
| Sonardyne | Ranger | 18.0 kHz to 36.0 kHz | 2000 m | 0.2 m |
| iXblue | GAPS | 20 kHz to 30 kHz | 4000 m | 2.4 m [2] |
| iXblue | Posidonia | 8 kHz to 16 kHz | 10 000 m | 2.0 m [3] |
| iXblue | RamsesLF | 8 kHz to 17.5 kHz | 10 000 m | 0.1 m |
| iXblue | RamsesMF | 20 kHz to 30 kHz | 4000 m | 0.1 m |
| Benthos | DAT | 9 kHz to 14 kHz | 6000 m | 0.3 m |
| Kongsberg | cNode | 15 kHz and 30 kHz | 4000 m | 0.02 m |

[1] Manufacturer specified ping accuracy 0.0005% of rate used to determine estimated error.
[2] Manufacturer specified position accuracy 0.06% of slant used to determine estimated error.
[3] Manufacturer specified position accuracy 0.02% of slant used to determine estimated error.

Table 6.1: Commercial positioning technology accuracies.

transponder system specified with $< 0.02$ m as the minimum error among popular, commercially available systems. A range error is randomly chosen from a normal distribution with standard deviation of 0.02 m and added to the relative range values used to derive the source location.

## 6.1 Near field with error

The first simulation results for this subsection represent the near field region which consists of source simulation in a 200 m $\times$ 200 m region for a receiver array dimension of 100 m $\times$ 100 m. The minimum distance from the edge of the simulated source region to the nearest node in the receiver array is 201 m. The geometric centre of the receiver array coincides with a centreline for the source region. The corners of the array slightly offset by at most a metre in longitude and/or a metre in latitude to ensure that the corners do not define a perfect square. The simulated position resolution is 1 m. The

constraints are the same as for the previous near field simulations, with the exception that an error is included.

The processing time for the near field source region was 16.48 h. The basic summary statistics regarding estimated position error are provided in Table 6.2 and Table 6.3. The frequency counts for different bounds of estimated position error is provided in Table 6.2.

| | Estimated Postion Error Frequency | | | | No |
|---|---|---|---|---|---|
| | $< 1$ m | $< 5$ m | $< 100$ m | $> 100$ m | Solution |
| *AIGL* | | | | | |
| Count | 4471 | 14000 | 19252 | 2277 | 0 |
| | 11.178% | 35.000% | 48.130% | 5.693% | 0% |
| *NLSL* | | | | | |
| Count | 14275 | 22321 | 3404 | 0 | 0 |
| | 35.688% | 55.803% | 8.510% | 0% | 0% |

Table 6.2: Near field position estimate error using simulated measurement error frequency counts.

The set of comprehensive three dimensional and two dimensional surface plots Figure 6.1 - 6.3 visualize the position error estimates for both AIGL, NLSL and their difference. Figures 6.1 and 6.2 show the error for AIGL and NLSL respectively. Figure 6.3 shows the relative difference in error for AIGL and NLSL.

The error statistics for AIGL and NLSL are summarized in Table 6.3. A histogram of the estimate error distributions is given in Figure 6.4.

The second set of near field simulations is configured with the receiver array rotated by 45° as shown in Figure 5.1 (b). Simulation runtime with the rotated array was 16.36 h. The basic summary statistics regarding estimated position error are provided in Table 6.4 and Table 6.5. The frequency counts for different bounds of estimated position error is provided in Table 6.4.

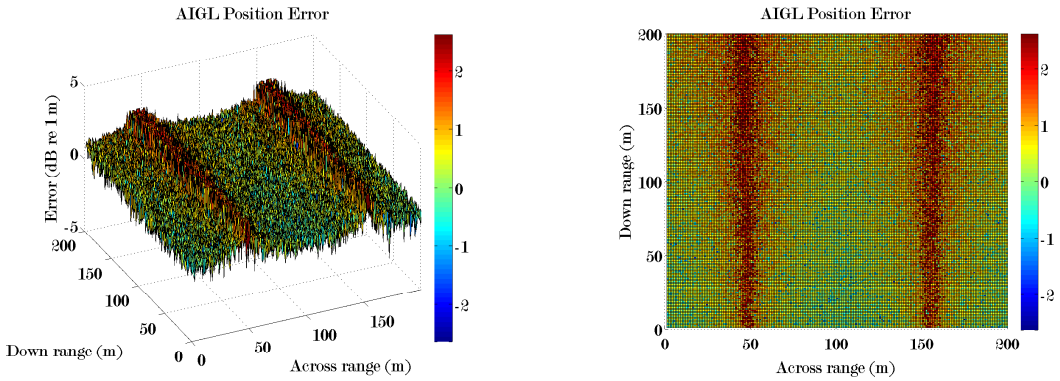


Figure 6.1: The positional estimate error for AIGL in the near field region using simulated measurement error.

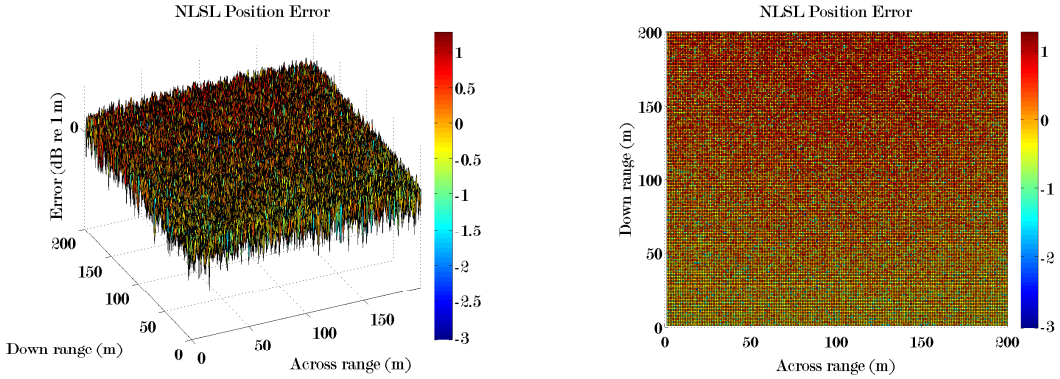


Figure 6.2: The positional estimate error for NLSL in the near field region using simulated measurement error.

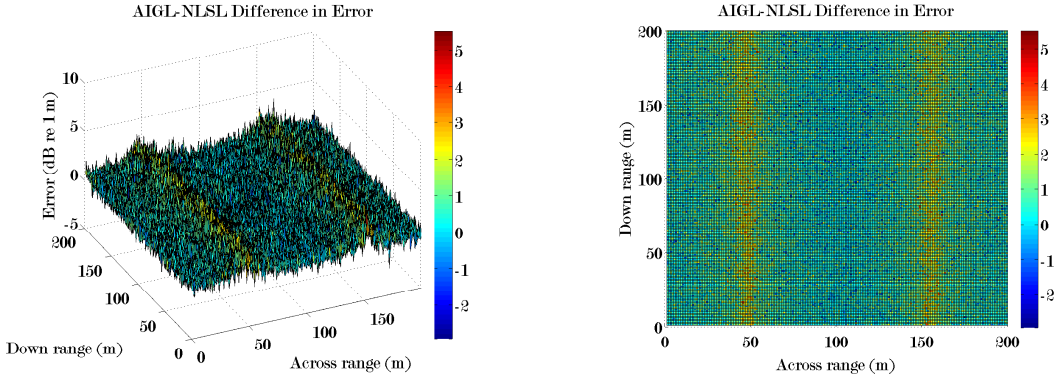


Figure 6.3: The positional estimate difference in error for AIGL and NLSL in the near field region using simulated measurement error.

| | Mean | Variance | Standard Deviation | Null Count |
|---|---|---|---|---|
| *AIGL* | 0.7692 | 0.4883 | 0.6988 | 0 |
| *NLSL* | 0.1045 | 0.2424 | 0.4924 | 0 |

Table 6.3: Near field AIGL and NLSL position estimate log error statistics using simulated measurement error.

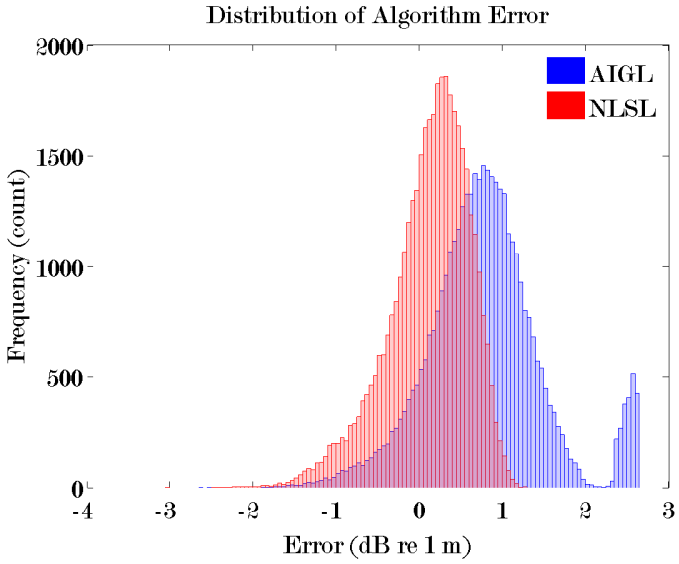


Figure 6.4: Distribution of the positional error for AIGL (blue) and NLSL (red) in the near field using simulated measurement error.

| | Estimated Postion Error Frequency | | | | No |
|---|---|---|---|---|---|
| | $< 1$ m | $< 5$ m | $< 100$ m | $> 100$ m | Solution |
| *AIGL* | | | | | |
| Count | 7862 | 18730 | 12360 | 1048 | 0 |
| | 19.655% | 46.825% | 30.900% | 2.620% | 0% |
| *NLSL* | | | | | |
| Count | 29341 | 10659 | 0 | 0 | 0 |
| | 73.353% | 26.648% | 0% | 0% | 0% |

Table 6.4: Near field position estimate error with rotated receiver array and using simulated measurement error frequency counts.

The set of comprehensive three dimensional and two dimensional surface plots Figure 6.5 - 6.7 visualize the position error estimates for both AIGL, NLSL and their difference. Figures 6.5 and 6.6 show the error for AIGL and NLSL respectively. Figure 6.7 shows the relative difference in error for AIGL and NLSL.

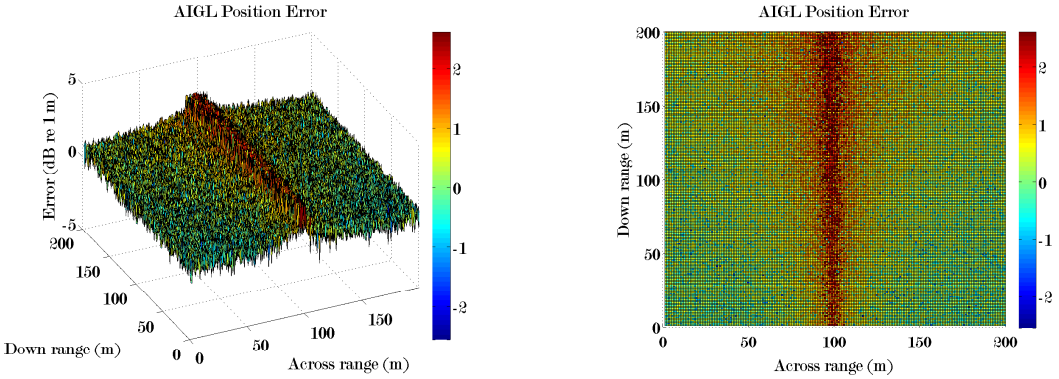


Figure 6.5: The positional estimate error for AIGL in the near field region with rotated receiver array using simulated measurement error.

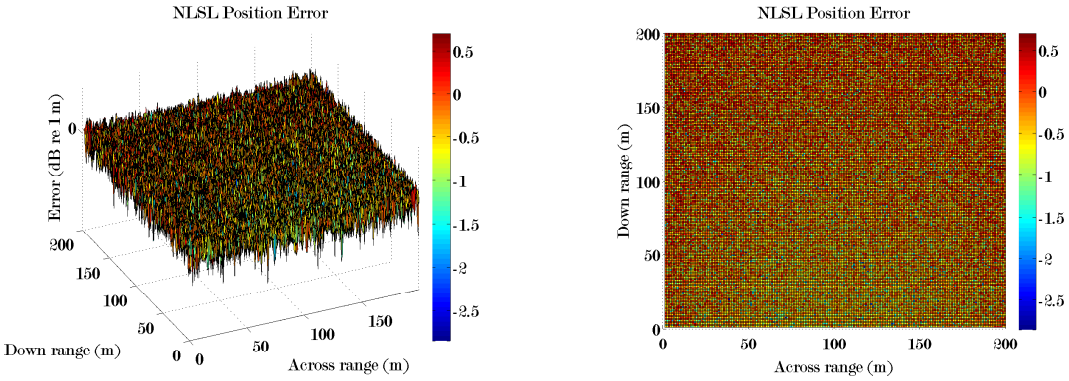


Figure 6.6: The positional estimate error for NLSL in the near field region with rotated receiver array using simulated measurement error.

The error statistics for AIGL and NLSL are summarized in Table 6.5. A histogram of the estimate error distributions is given in Figure 6.8.

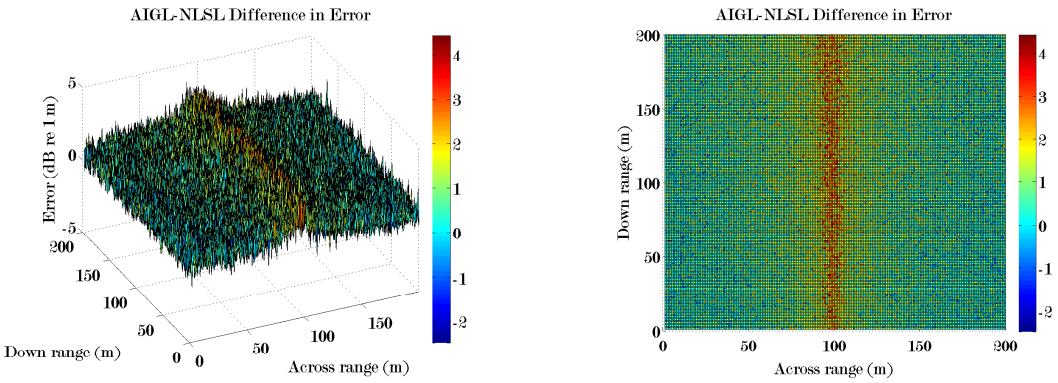


Figure 6.7: The positional estimate difference in error for AIGL and NLSL in the near field region with rotated receiver array using simulated measurement error.

| | Mean | Variance | Standard Deviation | Null Count |
|---|---|---|---|---|
| *AIGL* | 0.4916 | 0.4195 | 0.6477 | 0 |
| *NLSL* | -0.2945 | 0.1790 | 0.4230 | 0 |

Table 6.5: Near field AIGL and NLSL position estimate log error statistics for rotated receiver array using simulated measurement error.

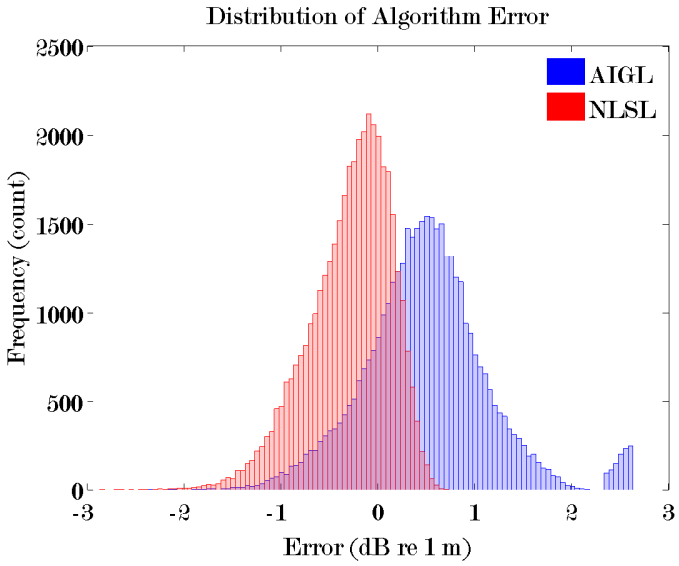


Figure 6.8: Distribution of the positional error for AIGL (blue) and NLSL (red) in the near field with rotated receiver array using simulated measurement error.

## 6.2 Medium-near field with error

The first simulation results for this subsection represent the medium-near field region which consists of source simulation in a 2000 m × 2000 m region for a receiver array dimension of 100 m × 100 m. The minimum distance from the edge of the simulated source region to the nearest node in the receiver array is 210 m. The geometric centre of the receiver array coincides with a centreline for the source region. The corners of the array slightly offset by at most a metre in longitude and/or a metre in latitude to ensure that the corners do not define a perfect square. The simulated source position resolution is 10 m for the medium-near field as opposed to 1 m for the near field.

The processing time for the near field source region was 17.51 h. The basic summary statistics regarding estimated position error are provided in Table 6.6 and Table 6.7. The frequency counts for different bounds of estimated position error is provided in Table 6.6.

| | Estimated Postion Error Frequency | | | | No |
|---|---|---|---|---|---|
| | $< 1$ m | $< 5$ m | $< 100$ m | $> 100$ m | Solution |
| *AIGL* | | | | | |
| Count | 1087 | 4372 | 26581 | 6911 | 1049 |
| | 2.718% | 10.930% | 66.453% | 17.278% | 2.623% |
| *NLSL* | | | | | |
| Count | 3315 | 9011 | 24481 | 3130 | 63 |
| | 8.288% | 22.528% | 61.203% | 7.825% | 0.158% |

Table 6.6: Medium-near field position estimate error using simulated measurement error frequency counts.

The set of comprehensive three dimensional and two dimensional surface plots Figure 6.9 - 6.11 visualize the position error estimates for both AIGL, NLSL and their difference. Figures 6.9 and 6.10 show the error for AIGL and NLSL respectively.

Figure 6.11 shows the relative difference in error for AIGL and NLSL.

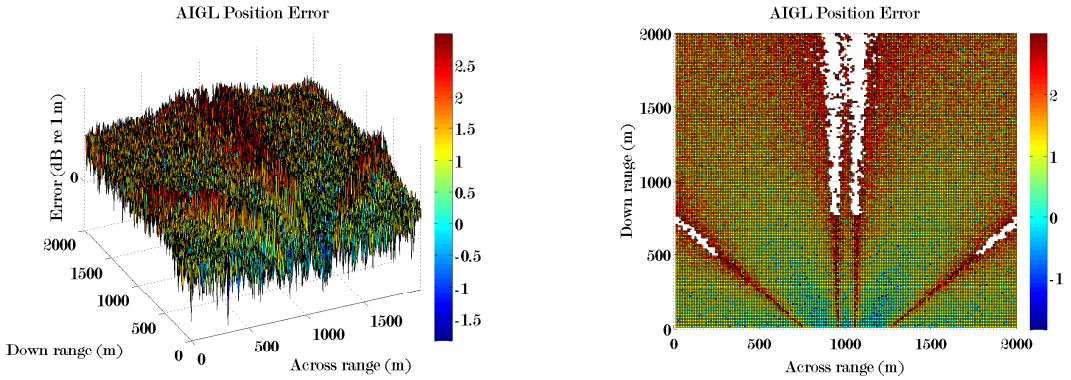


Figure 6.9: The positional estimate error for AIGL in the medium-near field region using simulated measurement error.

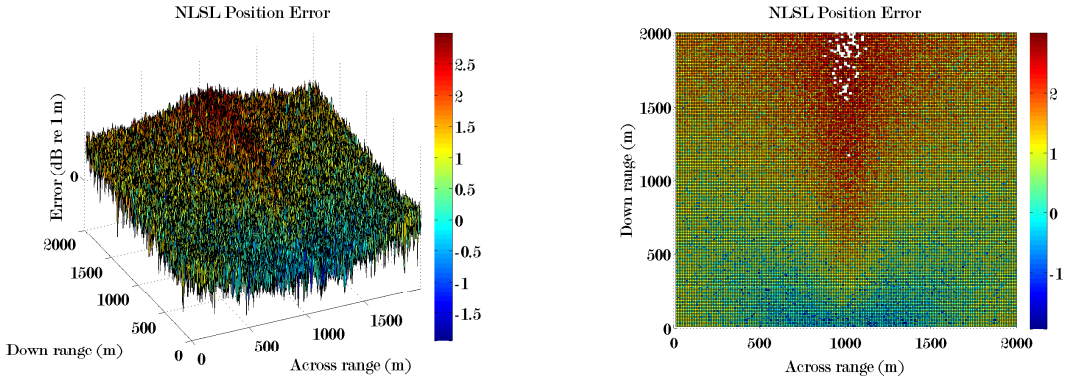


Figure 6.10: The positional estimate error for NLSL in the medium-near field region using simulated measurement error.

The error statistics for AIGL and NLSL are summarized in Table 6.7. A histogram of the estimate error distributions is given in Figure 6.12.

The second set of medium-near field simulations is configured with the receiver array rotated by 45° as shown in Figure 5.1 (b). Simulation runtime with the rotated array was 15.28 h. The basic summary statistics regarding estimated position error are provided in Table 6.8 and Table 6.9. The frequency counts for different bounds of estimated position error is provided in Table 6.8.

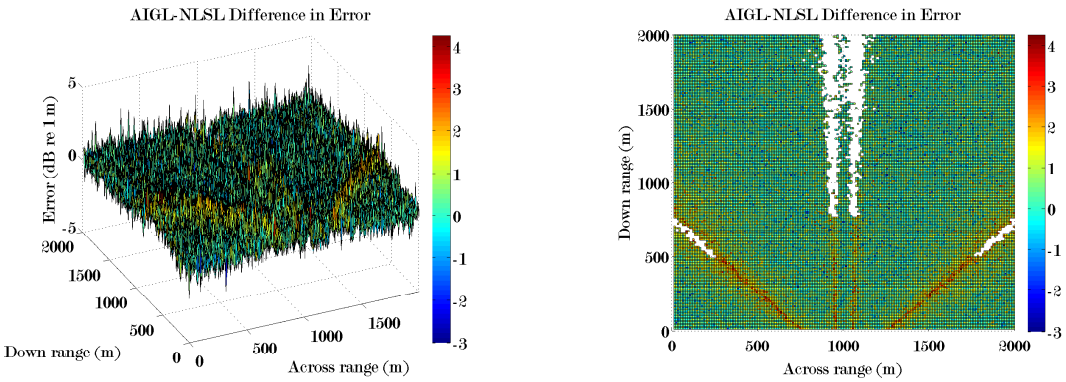


Figure 6.11: The positional estimate difference in error for AIGL and NLSL in the medium-near field region using simulated measurement error.

| | Mean | Variance | Standard Deviation | Null Count |
|---|---|---|---|---|
| *AIGL* | 1.4110 | 0.4480 | 0.6694 | 1049 |
| *NLSL* | 1.0248 | 0.5205 | 0.7214 | 63 |

Table 6.7: Medium-near field AIGL and NLSL position estimate log error statistics using simulated measurement error.

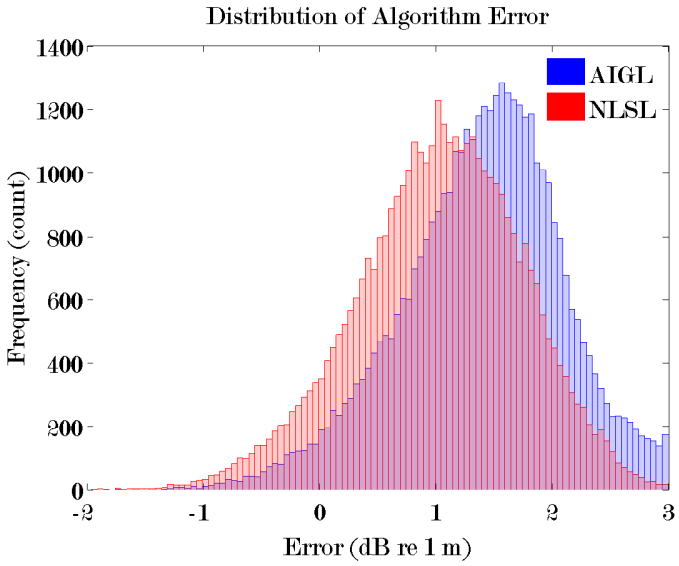


Figure 6.12: Distribution of the positional error for AIGL (blue) and NLSL (red) in the medium-near field using simulated measurement error.

| | Estimated Postion Error Frequency | | | | No |
|---|---|---|---|---|---|
| | $< 1\,\text{m}$ | $< 5\,\text{m}$ | $< 100\,\text{m}$ | $> 100\,\text{m}$ | Solution |
| *AIGL* | | | | | |
| Count | 1032 | 3939 | 27597 | 6730 | 702 |
| | 2.580% | 9.848% | 68.993% | 16.825% | 1.755% |
| *NLSL* | | | | | |
| Count | 2740 | 8495 | 27947 | 817 | 1 |
| | 6.850% | 21.238% | 69.868% | 2.043% | 0.003% |

Table 6.8: Medium-near field position estimate error with rotated receiver array and using simulated measurement error frequency counts.

The set of comprehensive three dimensional and two dimensional surface plots Figure 6.13 - 6.15 visualize the position error estimates for both AIGL, NLSL and their difference. Figures 6.13 and 6.14 show the error for AIGL and NLSL respectively. Figure 6.15 shows the relative difference in error for AIGL and NLSL.

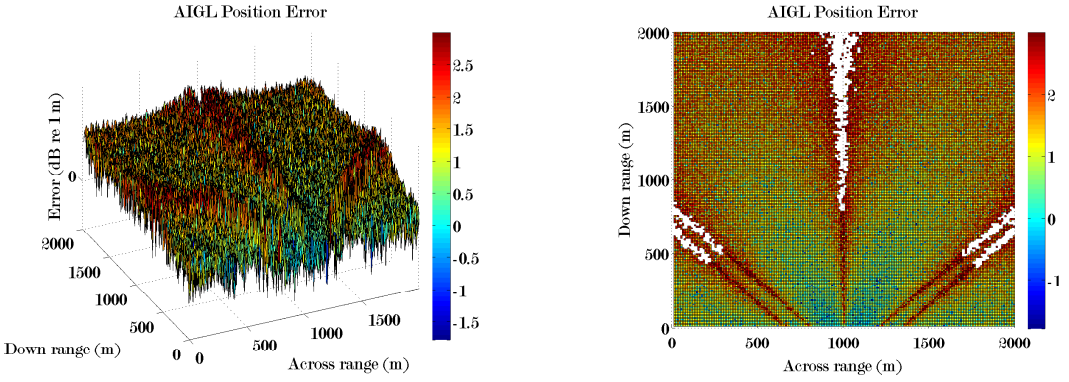


Figure 6.13: The positional estimate error for AIGL in the medium-near field region with rotated receiver array using simulated measurement error.

The error statistics for AIGL and NLSL are summarized in Table 6.9. A histogram of the estimate error distributions is given in Figure 6.16.

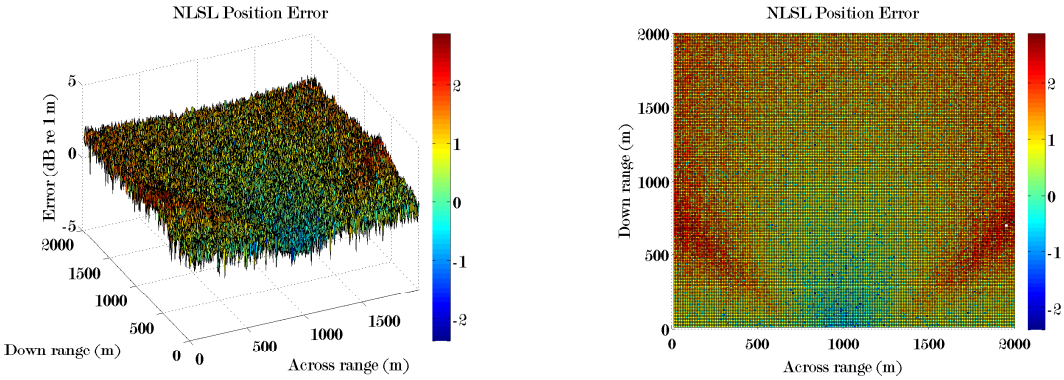


Figure 6.14: The positional estimate error for NLSL in the medium-near field region with rotated receiver array using simulated measurement error.

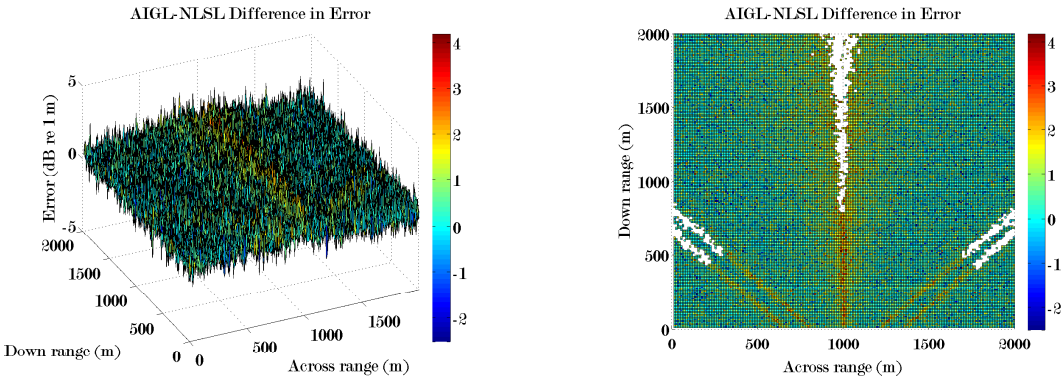


Figure 6.15: The positional estimate difference in error for AIGL and NLSL in the medium-near field region with rotated receiver array using simulated measurement error.

| | Mean | Variance | Standard Deviation | Null Count |
|---|---|---|---|---|
| *AIGL* | 1.4275 | 0.4186 | 0.6470 | 702 |
| *NLSL* | 0.9880 | 0.3707 | 0.6088 | 1 |

Table 6.9: Medium-near field AIGL and NLSL position estimate log error statistics for rotated receiver array using simulated measurement error.

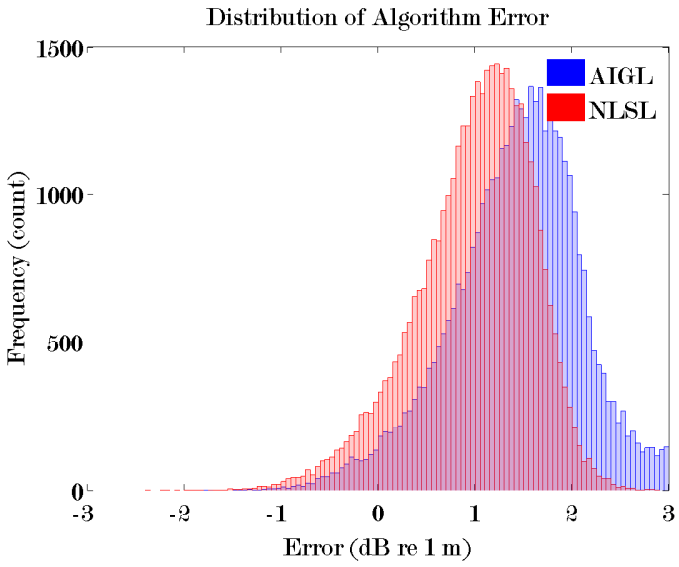


Figure 6.16: Distribution of the positional error for AIGL (blue) and NLSL (red) in the medium-near field with rotated receiver array using simulated measurement error.

## 6.3 Medium field with error

The first simulation results for this subsection represent the medium field region which consists of source simulation in a 20 km × 20 km region for a receiver array dimension of 100 m × 100 m. The minimum distance from the edge of the simulated source region to the nearest node in the receiver array is 300 m. The geometric centre of the receiver array coincides with a centreline for the source region. The corners of the array slightly offset by at most a metre in longitude and/or a metre in latitude to ensure that the corners do not define a perfect square. The simulated position resolution is 100 m.

The processing time for the near field source region was 15.92 h. The basic summary statistics regarding estimated position error are provided in Table 6.10 and Table 6.11. The frequency counts for different bounds of estimated position error is provided in Table 6.10.

The set of comprehensive three dimensional and two dimensional surface plots

| | Estimated Postion Error Frequency | | | | No |
|---|---|---|---|---|---|
| | $< 1\,\text{m}$ | $< 5\,\text{m}$ | $< 100\,\text{m}$ | $> 100\,\text{m}$ | Solution |
| *AIGL* | | | | | |
| Count | 17 | 123 | 2347 | 11124 | 26389 |
| | 0.043% | 0.308% | 5.868% | 27.810% | 65.973% |
| *NLSL* | | | | | |
| Count | 102 | 402 | 4829 | 17288 | 17379 |
| | 0.255% | 1.005% | 12.073% | 43.220% | 43.448% |

Table 6.10: Medium field position estimate error using simulated measurement error frequency counts.

Figure 6.17 - 6.19 visualize the position error estimates for both AIGL, NLSL and their difference. Figures 6.17 and 6.18 show the error for AIGL and NLSL respectively. Figure 6.19 shows the relative difference in error for AIGL and NLSL.

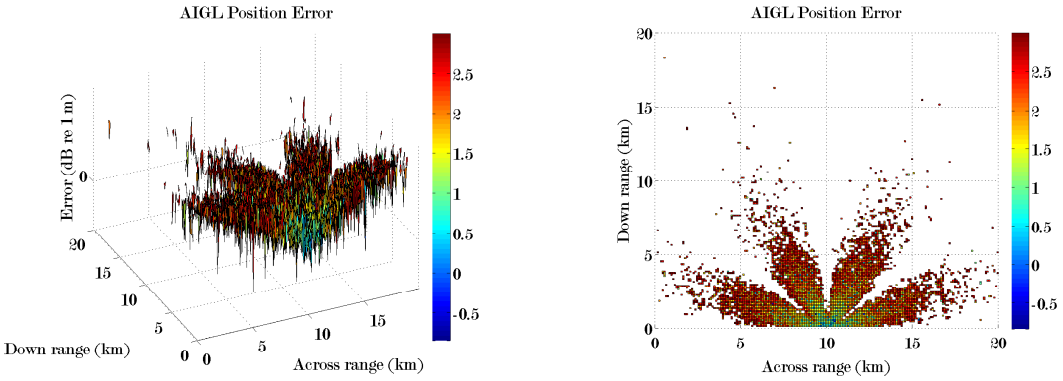


Figure 6.17: The positional estimate error for AIGL in the medium field region using simulated measurement error.

The error statistics for AIGL and NLSL are summarized in Table 6.11. A histogram of the estimate error distributions is given in Figure 6.20.

The second set of medium field simulations is configured with the receiver array rotated by 45° as shown in Figure 5.1 (b). Simulation runtime with the rotated array was 13.65 h. The basic summary statistics regarding estimated position error are

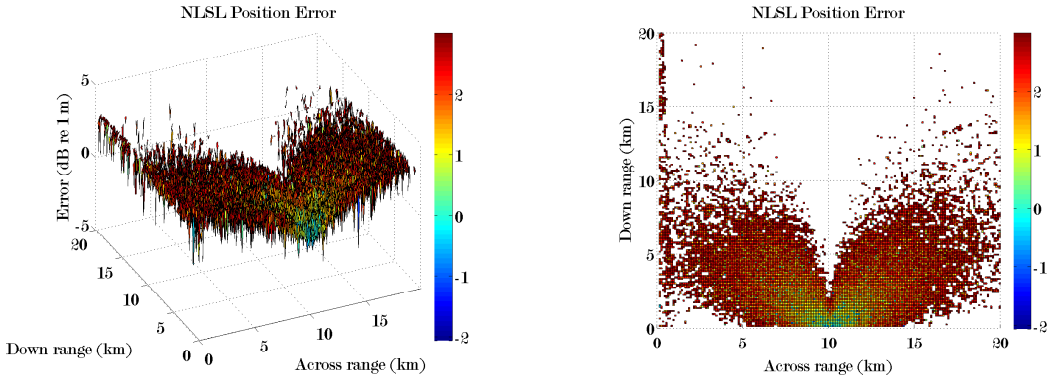


Figure 6.18: The positional estimate error for NLSL in the medium field region using simulated measurement error.

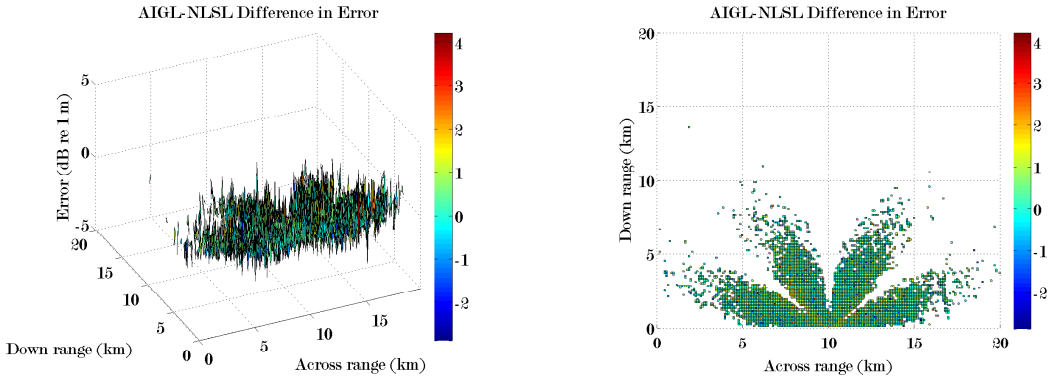


Figure 6.19: The positional estimate difference in error for AIGL and NLSL in the medium field region using simulated measurement error.

| | Mean | Variance | Standard Deviation | Null Count |
|---|---|---|---|---|
| *AIGL* | 2.4148 | 0.2750 | 0.5244 | 26389 |
| *NLSL* | 2.3096 | 0.5783 | 0.7604 | 17379 |

Table 6.11: Medium field AIGL and NLSL position estimate log error statistics using simulated measurement error.

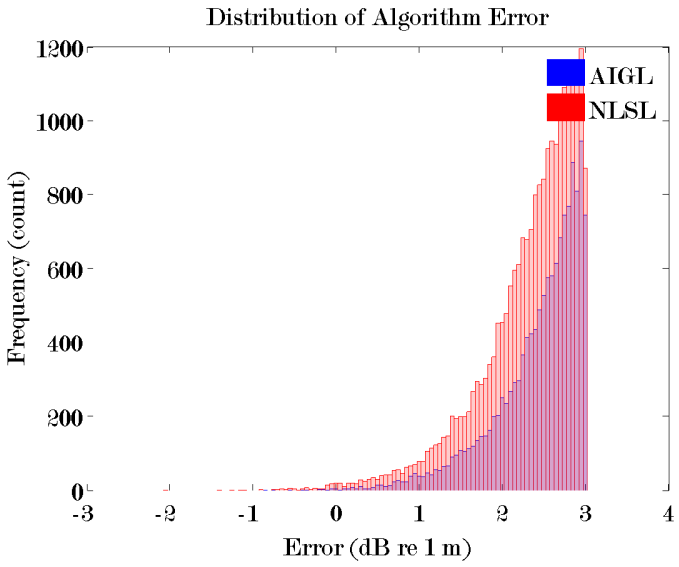


Figure 6.20: Distribution of the positional error for AIGL (blue) and NLSL (red) in the medium field using simulated measurement error.

provided in Table 6.12 and Table 6.13. The frequency counts for different bounds of estimated position error is provided in Table 6.12.

The set of comprehensive three dimensional and two dimensional surface plots Figure 6.21 - 6.23 visualize the position error estimates for both AIGL, NLSL and their difference. Figures 6.21 and 6.22 show the error for AIGL and NLSL respectively. Figure 6.23 shows the relative difference in error for AIGL and NLSL.

The error statistics for AIGL and NLSL are summarized in Table 6.13. A histogram of the estimate error distributions is given in Figure 6.24.

| | Estimated Postion Error Frequency | | | | No |
|---|---|---|---|---|---|
| | $< 1\,\text{m}$ | $< 5\,\text{m}$ | $< 100\,\text{m}$ | $> 100\,\text{m}$ | Solution |
| *AIGL* | | | | | |
| Count | 17 | 138 | 2281 | 11201 | 26363 |
| | 0.043% | 0.345% | 5.703% | 28.003% | 65.908% |
| *NLSL* | | | | | |
| Count | 87 | 364 | 4641 | 17666 | 17242 |
| | 0.218% | 0.910% | 11.603% | 44.165% | 43.105% |

Table 6.12: Medium field position estimate error with rotated receiver array and using simulated measurement error frequency counts.

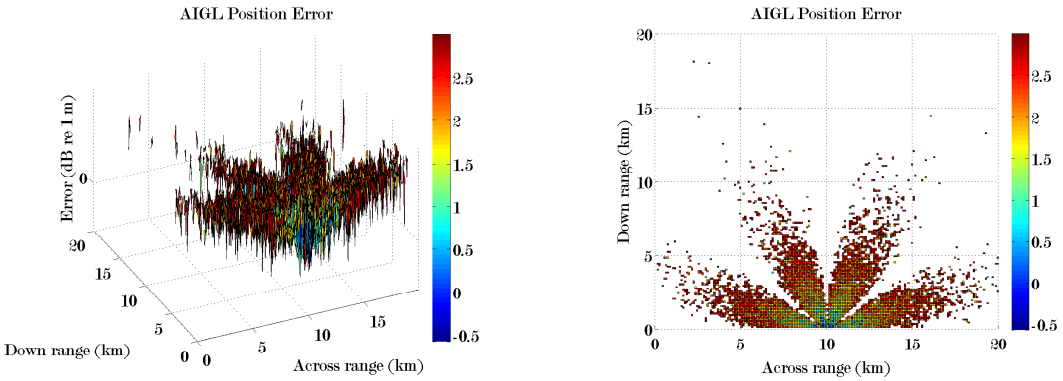


Figure 6.21: The positional estimate error for AIGL in the medium field region with rotated receiver array using simulated measurement error.

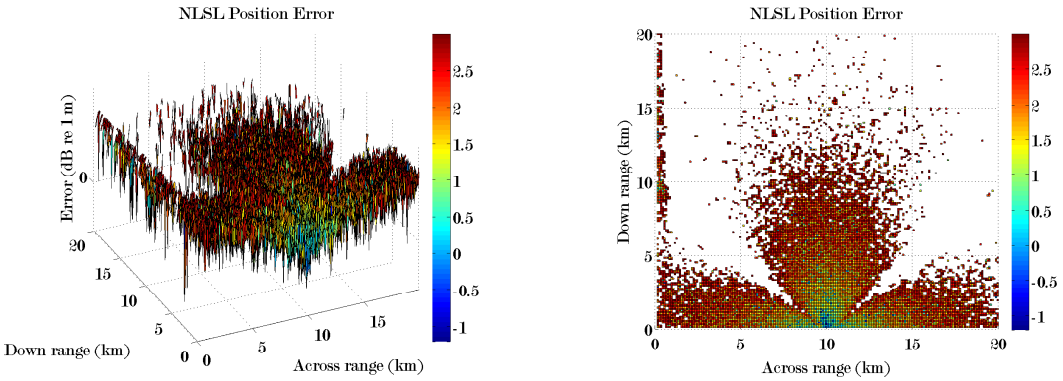


Figure 6.22: The positional estimate error for NLSL in the medium field region with rotated receiver array using simulated measurement error.

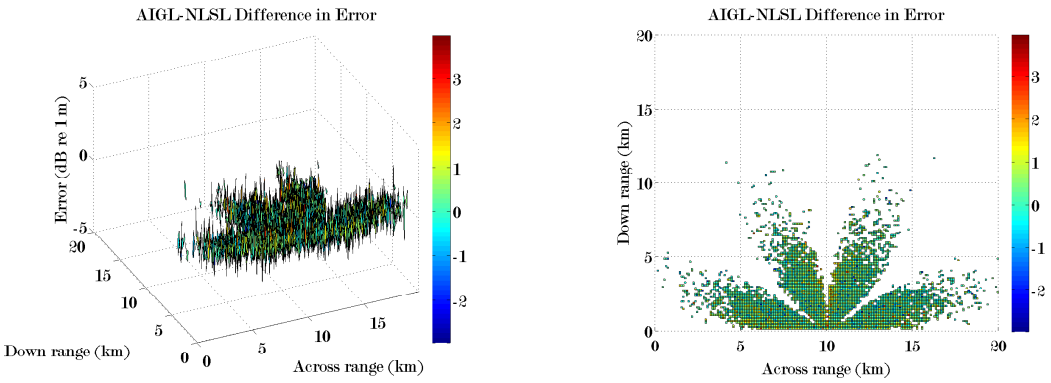


Figure 6.23: The positional estimate difference in error for AIGL and NLSL in the medium field region with rotated receiver array using simulated measurement error.

| | Mean | Variance | Standard Deviation | Null Count |
|---|---|---|---|---|
| *AIGL* | 2.4164 | 0.2712 | 0.5208 | 26363 |
| *NLSL* | 2.3322 | 0.5498 | 0.7415 | 17242 |

Table 6.13: Medium field AIGL and NLSL position estimate log error statistics for rotated receiver array using simulated measurement error.

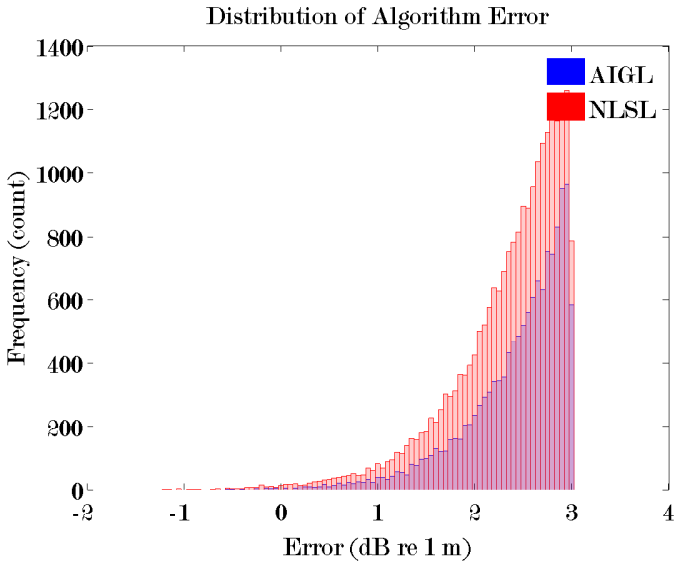


Figure 6.24: Distribution of the positional error for AIGL (blue) and NLSL (red) in the medium field with rotated receiver array using simulated measurement error.

## 6.4 Far field with error

The simulation results for this subsection represent the far field region which consists of source simulation in a 200 km × 200 km region for a receiver array dimension of 100 m × 100 m. The minimum distance from the edge of the simulated source region to the nearest node in the receiver array is 1200 m. The geometric centre of the receiver array coincides with a centreline for the source region. The corners of the array slightly offset by at most a metre in longitude and/or a metre in latitude to ensure that the corners do not define a perfect square. The simulated position resolution is 1 km.

The processing time for the far field source region was 13.31 h. The basic summary statistics regarding estimated position error are provided in Table 6.14 and Table 6.15. The frequency counts for different bounds of estimated position error is provided in Table 6.14.

| | Estimated Postion Error Frequency | | | | No |
|---|---|---|---|---|---|
| | $< 1$ m | $< 5$ m | $< 100$ m | $> 100$ m | Solution |
| *AIGL* | | | | | |
| Count | 0 | 1 | 54 | 325 | 39620 |
| | 0% | 0.003% | 0.135% | 0.813% | 99.050% |
| *NLSL* | | | | | |
| Count | 6 | 87 | 3501 | 5300 | 31106 |
| | 0.015% | 0.218% | 8.753% | 13.250% | 77.765% |

Table 6.14: Far field position estimate error using simulated measurement error frequency counts.

The set of comprehensive three dimensional and two dimensional surface plots for the far field simulated with error do not contain many data points. Predictably, the set of solutions corresponding to reasonable error is congregated in the vicinity of receiver. The error statistics for AIGL and NLSL are summarized in Table 6.15. A

histogram of the estimate error distributions is given in Figure 6.25.

| | Mean | Variance | Standard Deviation | Null Count |
|---|---|---|---|---|
| *AIGL* | 2.4990 | 0.1939 | 0.4404 | 39620 |
| *NLSL* | 2.1114 | 7.5542 | 2.7485 | 31106 |

Table 6.15: Far field AIGL and NLSL position estimate log error statistics using simulated measurement error.

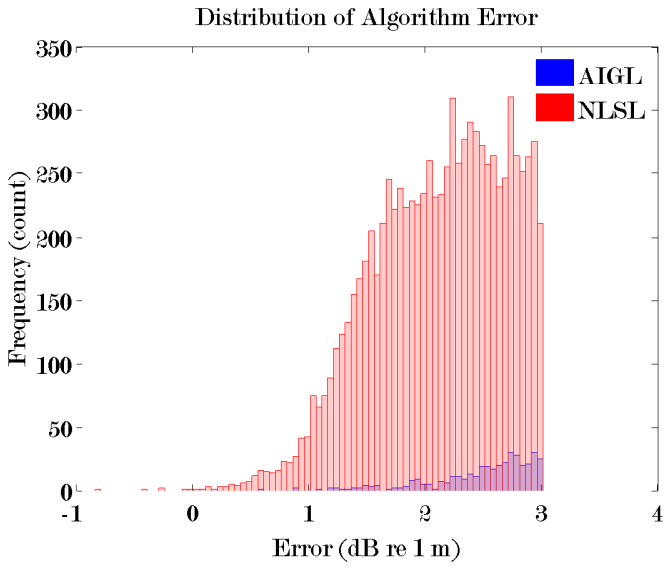


Figure 6.25: Distribution of the positional error for AIGL (blue) and NLSL (red) in the far field using simulated measurement error.

The second set of far field simulations is configured with the receiver array rotated by 45° as shown in Figure 5.1 (b). Simulation runtime with the rotated array was 16.77 h. The basic summary statistics regarding estimated position error are provided in Table 6.16 and Table 6.17. The frequency counts for different bounds of estimated position error is provided in Table 6.16.

The set of comprehensive three dimensional and two dimensional surface plots for the far field simulations with measurement error are sparse. Surface plots and

| | Estimated Postion Error Frequency | | | | No |
|---|---|---|---|---|---|
| | $< 1\,\mathrm{m}$ | $< 5\,\mathrm{m}$ | $< 100\,\mathrm{m}$ | $> 100\,\mathrm{m}$ | Solution |
| *AIGL* | | | | | |
| Count | 0 | 0 | 35 | 332 | 39633 |
| | 0% | 0% | 0.088% | 0.830% | 99.083% |
| *NLSL* | | | | | |
| Count | 18 | 104 | 3825 | 4503 | 31550 |
| | 0.045% | 0.260% | 9.563% | 11.258% | 78.875% |

Table 6.16: Far field position estimate error with rotated receiver array and using simulated measurement error frequency counts.

colour maps do not convey much information. The error statistics for AIGL and NLSL are summarized in Table 6.17. A histogram of the estimate error distributions is given in Figure 6.26.

| | Mean | Variance | Standard Deviation | Null Count |
|---|---|---|---|---|
| *AIGL* | 2.5529 | 0.1472 | 0.3837 | 39633 |
| *NLSL* | 2.0371 | 7.4111 | 2.7223 | 31550 |

Table 6.17: Far field AIGL and NLSL position estimate log error statistics for rotated receiver array using simulated measurement error.

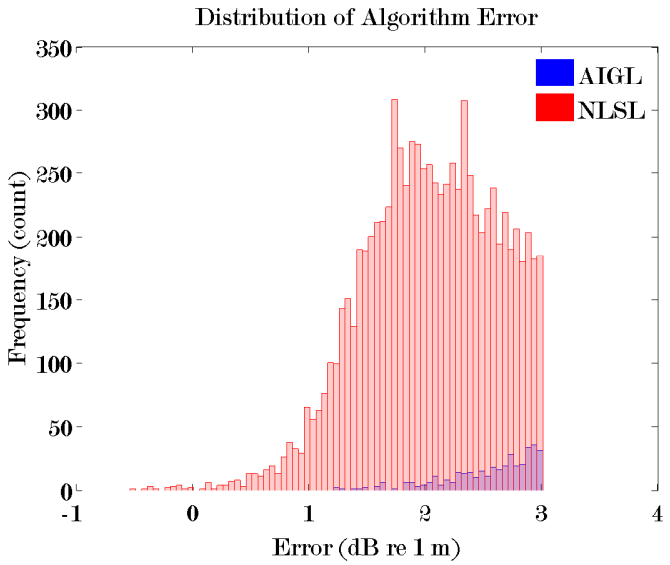


Figure 6.26: Distribution of the positional error for AIGL (blue) and NLSL (red) in the far field with rotated receiver array using simulated measurement error.

## 6.5 Discussion

Random error based on current commercial acoustic ranging systems has been added to the individual relative ranges (recall $\delta_{0i}$ in Figure 3.3) for each of the 320 000 simulated source positions. The SBSH algorithms are applied to determine the source location. There is a noticeable effect on the performance of the both SBSH algorithms. Simulation processing times increase significantly once external error is introduced to simulations. Run times for all regions ranged from 13.31 to 17.51 h indicating a greater number of iterative searches occurring within processing before convergence on an acceptable solution. Table 6.18 contains the frequency counts for different error ranges.

Successful location occurs approximately 45% of the time for the AIGL algorithm and 54% of the time for the NLSL. The number of instances where no solution is found has increased with the inclusion of external error. The frequency for localization error over 1000 m is almost 42% for the AIGL algorithm and just over 30% for the NLSL

| | Simulation II Est. Postion Error Freq. | | | | No |
|---|---|---|---|---|---|
| | $< 1\,\text{m}$ | $< 5\,\text{m}$ | $< 100\,\text{m}$ | $> 100\,\text{m}$ | Solution |
| *AIGL* | | | | | |
| Count | 14486 | 41303 | 90507 | 39948 | 133756 |
| | 4.527% | 12.907% | 28.283% | 12.483% | 41.799% |
| *NLSL* | | | | | |
| Count | 49884 | 51443 | 72628 | 48704 | 97341 |
| | 15.589% | 16.076% | 22.696% | 15.220% | 30.419% |

Table 6.18: Far field position estimate error using simulated measurement error frequency counts.

algorithm.

The general tendency for the error to increase as the source moves further from the array is more noticeable in the second simulation set. Consider the error plots for the medium near region, Figure 6.9, Figure 6.10, Figure 6.13 and Figure 6.13. First, note that the increased error features and ridges identified in the first set of simulations tend to be softened, but are still visible. A general increasing trend in error as source distance from receiver array is present. This is evidenced by the predominance of the blue-green colour close to the receiver array transitioning to the red as range from the receiver increases.

A review of the difference in error plots and the histograms indicates that the NLSL algorithm performs slightly better than the AIGL algorithm in most cases. The NLSL error distribution adheres to a bell shape which was not the case for the "no external error" simulation set. The AIGL error distribution generally maintains its normal shape, but there is an edge peak on the right hand tail for the near field due to the number of location errors in the 100 m to 1000 m range.

The NLSL error distribution has a higher peak in the near field region. The standard deviation is 0.2 less for both cases (standard and rotated receiver array)

compared to the AIGL error distribution. The distributions closely resemble each other in the medium-near field region. Generally, the standard deviation for the AIGL error, even with external error, is consistent with the first set of simulations with no external error.

For the medium field region and far field there is an obvious clipping of the histograms due to the 1000 m "no solution" threshold. It is difficult to infer any sound conclusions other than most of the time, for these regions, clearly neither SBSH algorithm performs well. The number of positive solutions for both algorithms is limited, the AIGL algorithm has 55 successful localization estimates with the standard receiver array configuration and the NLSL algorithm has 3947 successful localization estimates with a rotated receiver array.

A summary of the statistics for the SBSH simulation results with external error is shown in Table 6.19.

| | Results of External Error | | | |
|---|---|---|---|---|
| | AIGL | | NLSL | |
| | Standard | Rotated | Standard | Rotated |
| Near | | | | |
| Mean | 0.77 | 0.49 | 0.10 | -0.29 |
| Std. Dev | 0.70 | 0.65 | 0.49 | 0.42 |
| % Success | 94.308% | 97.380% | 100.000% | 100.000% |
| Null count | 0 | 0 | 0 | 0 |
| Med-near | | | | |
| Mean | 1.41 | 1.43 | 1.02 | 0.99 |
| Std. Dev | 0.67 | 0.65 | 0.72 | 0.61 |
| % Success | 80.100% | 81.420% | 92.018% | 97.955% |
| Null count | 1049 | 702 | 63 | 1 |
| Medium | | | | |
| Mean | 2.41 | 2.42 | 2.31 | 2.33 |
| Std. Dev | 0.52 | 0.68 | 0.52 | 0.74 |
| % Success | 6.218% | 6.090% | 13.332% | 12.730% |
| Null count | 26389 | 26363 | 17379 | 17242 |
| Far | | | | |
| Mean | 2.50 | 2.55 | 2.11 | 2.04 |
| Std. Dev | 0.44 | 0.38 | 2.75 | 2.72 |
| % Success | 0.138% | 0.088% | 8.985% | 9.868% |
| Null count | 39620 | 39633 | 31106 | 31550 |

Table 6.19: Simulation statistics for differing source location regions: near field, medium-near field, medium field and far field.

# Chapter 7

# Simulation III: Extending Receiver Array Dimension

Simulations with increased receiver array spacing have an understandable effect on the magnitude of the position estimate error and the number of null solutions. Both are reduced. Two sets of simulations are undertaken: the medium field with 1000 m receiver array spacing and the far field with 10 km receiver array spacing.

## 7.1 Medium field with error and larger receiver array dimension

The first simulation results for this subsection represent the medium field region which consists of source simulation in a 20 km × 20 km region for a receiver array dimension of 1000 m × 1000 m. The minimum distance from the edge of the simulated source region to the nearest node in the receiver array is 300 m. The geometric centre of the receiver array coincides with a centreline for the source region. The corners of the array slightly offset by at most a metre in longitude and/or a metre in latitude

to ensure that the corners do not define a perfect square. The simulated position resolution is 100 m.

The processing time for the medium field source region was 11.61 h. The basic summary statistics regarding estimated position error are provided in Table 7.1 and Table 7.2. The frequency counts for different bounds of estimated position error is provided in Table 7.1.

| | Estimated Postion Error Frequency | | | | No |
|---|---|---|---|---|---|
| | $< 1$ m | $< 5$ m | $< 100$ m | $> 100$ m | Solution |
| *AIGL* | | | | | |
| Count | 1802 | 5430 | 26604 | 5355 | 809 |
| | 4.505% | 13.575% | 66.510% | 13.388% | 2.023% |
| *NLSL* | | | | | |
| Count | 4692 | 10149 | 22902 | 2240 | 17 |
| | 11.730% | 25.373% | 57.255% | 5.600% | 0.043% |

Table 7.1: Medium field position estimate error using simulated measurement error frequency counts.

The set of comprehensive three dimensional and two dimensional surface plots Figure 7.1 - 7.3 visualize the position error estimates for both AIGL, NLSL and their difference. Figures 7.1 and 7.2 show the error for AIGL and NLSL respectively. Figure 7.3 shows the relative difference in error for AIGL and NLSL.

The error statistics for AIGL and NLSL are summarized in Table 7.2. A histogram of the estimate error distributions is given in Figure 7.4.

The second set of medium field simulations is configured with the receiver array rotated by 45° as shown in Figure 5.1 (b). Simulation runtime with the rotated array was 11.18 h. Summary statistics regarding estimated position error are provided in Table 7.3 and Table 7.4. The frequency counts for different bounds of estimated position error is provided in Table 7.3.

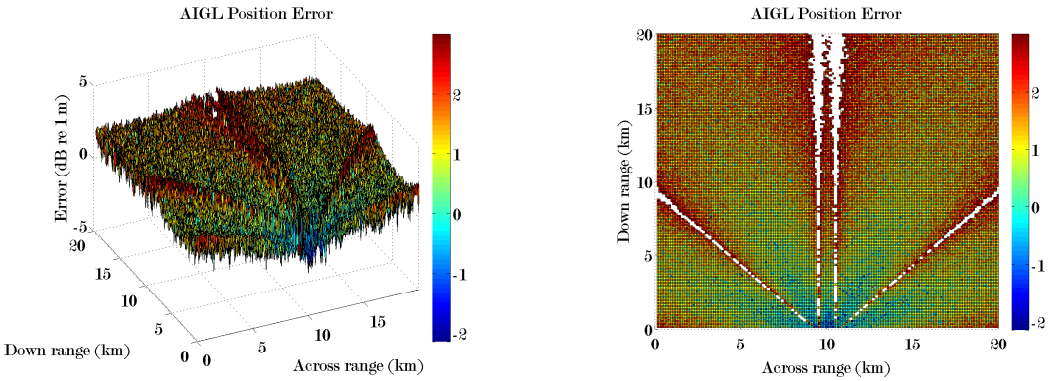


Figure 7.1: The positional estimate error for AIGL in the medium field region using simulated measurement error and wider receiver spacing.

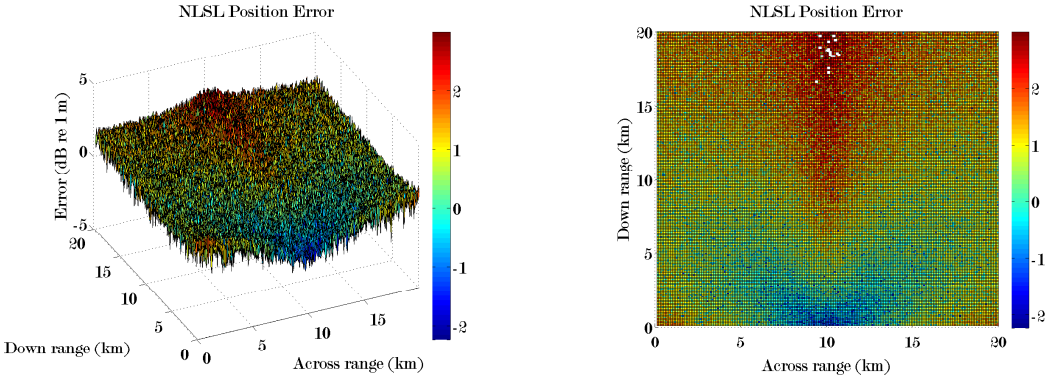


Figure 7.2: The positional estimate error for NLSL in the medium field region using simulated measurement error and wider receiver spacing.

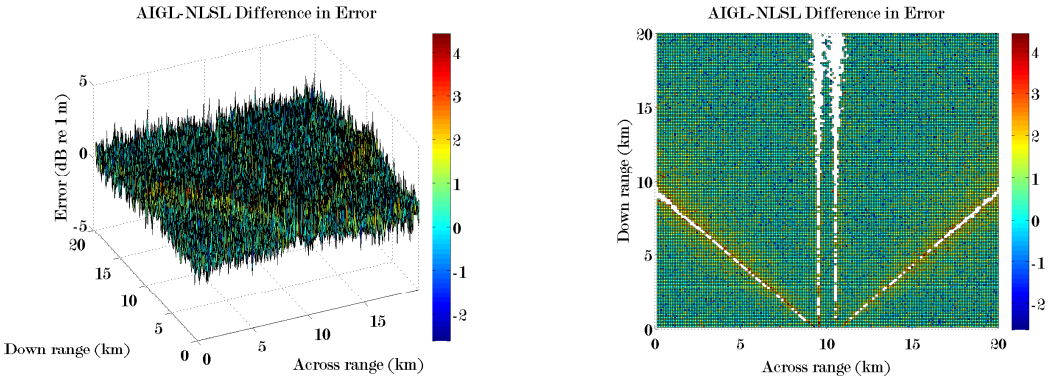


Figure 7.3: The positional estimate difference in error for AIGL and NLSL in the medium field region using simulated measurement error and wider receiver spacing.

| | Mean | Variance | Standard Deviation | Null Count |
|---|---|---|---|---|
| *AIGL* | 1.2937 | 0.4853 | 0.6966 | 809 |
| *NLSL* | 0.8943 | 0.5537 | 0.7441 | 17 |

Table 7.2: Medium field AIGL and NLSL position estimate log error statistics with measurement error and wider receiver spacing.

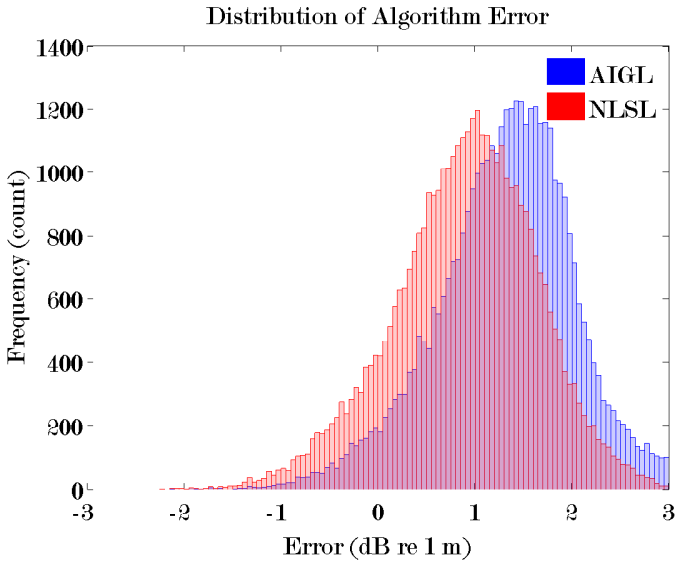


Figure 7.4: Distribution of the positional error for AIGL (blue) and NLSL (red) in the medium field using simulated measurement error and wider receiver spacing.

| | Estimated Postion Error Frequency | | | | No |
|---|---|---|---|---|---|
| | $< 1$ m | $< 5$ m | $< 100$ m | $> 100$ m | Solution |
| *AIGL* | | | | | |
| Count | 1561 | 5326 | 27024 | 5425 | 664 |
| | 3.903% | 13.315% | 67.560% | 13.563% | 1.660% |
| *NLSL* | | | | | |
| Count | 4006 | 9829 | 25410 | 755 | 0 |
| | 10.015% | 24.573% | 63.525% | 1.888% | 0% |

Table 7.3: Medium field position estimate error with rotated receiver array, measurement error and wider receiver spacing.

The set of comprehensive three dimensional and two dimensional surface plots Figure 7.5 - 7.7 visualize the position error estimates for both AIGL, NLSL and their difference. Figures 7.5 and 7.6 show the error for AIGL and NLSL respectively. Figure 7.7 shows the relative difference in error for AIGL and NLSL.

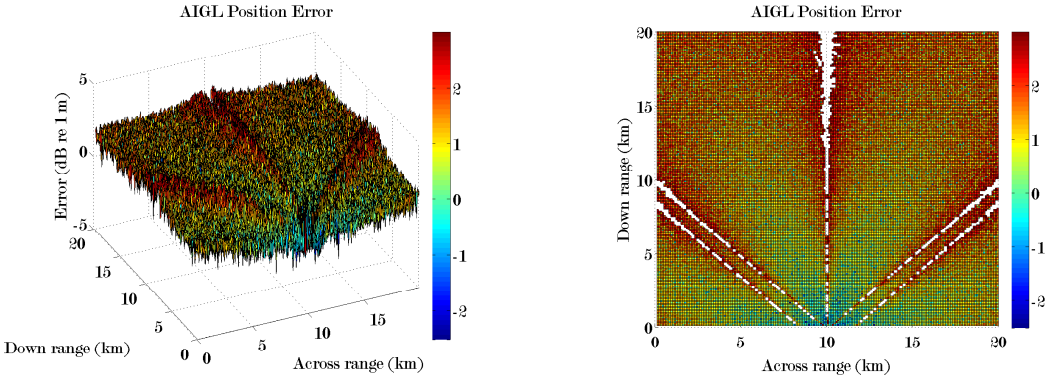


Figure 7.5: The positional estimate error for AIGL in the medium field region with rotated receiver array using simulated measurement error and wider receiver spacing.

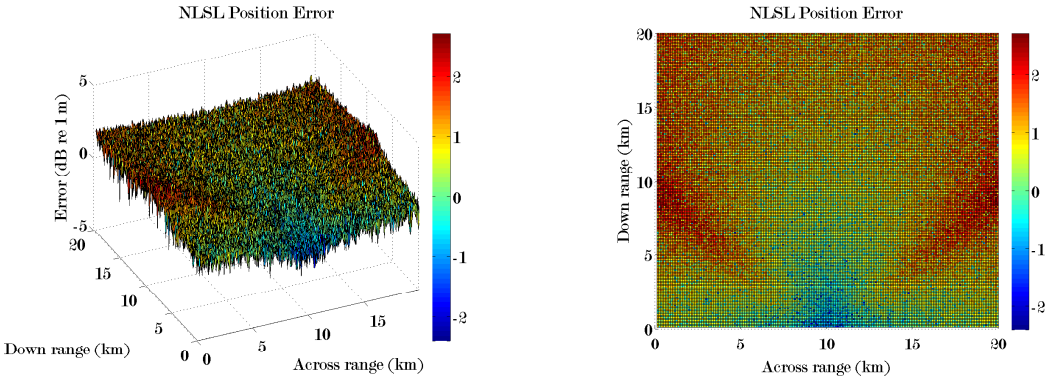


Figure 7.6: The positional estimate error for NLSL in the medium field region with rotated receiver array using simulated measurement error and wider receiver spacing.

The error statistics for AIGL and NLSL are summarized in Table 7.4. A histogram of the estimate error distributions is given in Figure 7.8.

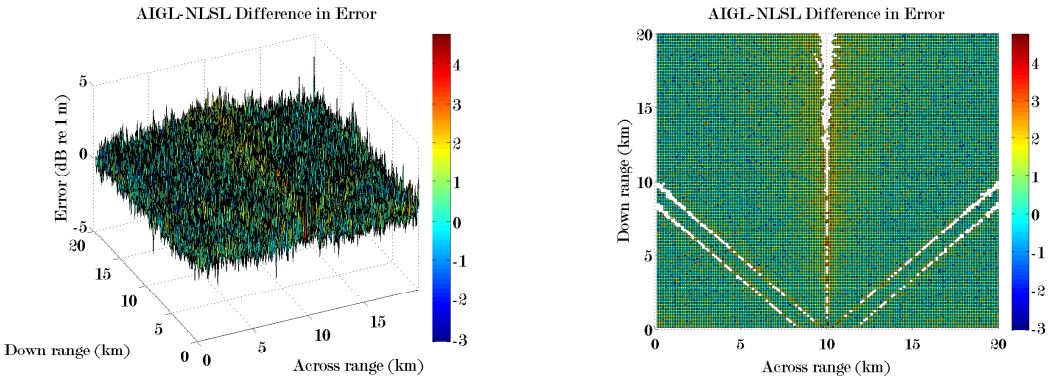


Figure 7.7: The positional estimate difference in error for AIGL and NLSL in the medium field region with rotated receiver array using simulated measurement error and wider receiver spacing.

| | Mean | Variance | Standard Deviation | Null Count |
|---|---|---|---|---|
| *AIGL* | 1.3138 | 0.4613 | 0.6792 | 664 |
| *NLSL* | 0.8816 | 0.4341 | 0.6588 | 0 |

Table 7.4: Medium field AIGL and NLSL position estimate log error statistics for rotated receiver array with measurement error and wider receiver spacing.

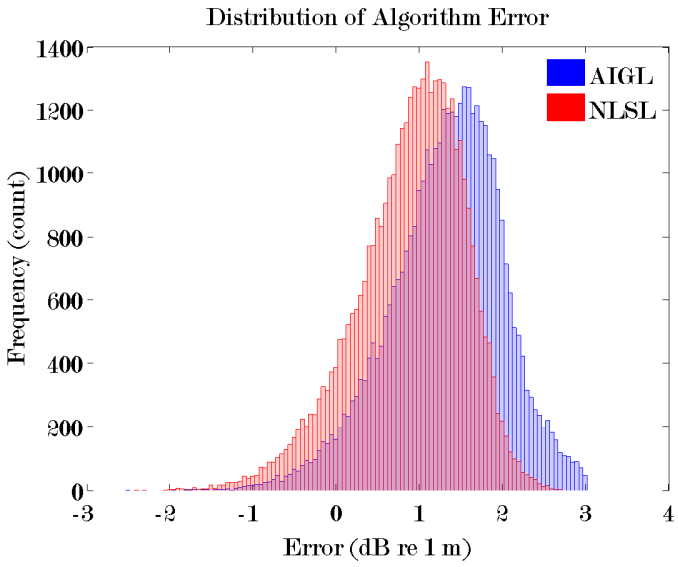


Figure 7.8: Distribution of the positional error for AIGL (blue) and NLSL (red) in the medium field with rotated receiver array, measurement error and wider receiver spacing.

## 7.2 Far field with error and larger receiver array dimension

The simulation results for this subsection represent the far field region which consists of source simulation in a 200 km × 200 km region for a receiver array dimension of 10 km × 10 km. The minimum distance from the edge of the simulated source region to the nearest node in the receiver array is 1200 m. The geometric centre of the receiver array coincides with a centreline for the source region. The corners of the array slightly offset by at most a metre in longitude and/or a metre in latitude to ensure that the corners do not define a perfect square. The simulated position resolution is 1000 m.

The processing time for the far field source region was 19.97 h. The basic summary statistics regarding estimated position error are provided in Table 7.5 and Table 7.6. The frequency counts for different bounds of estimated position error is provided

in Table 7.5.

| | Estimated Postion Error Frequency | | | | No |
|---|---|---|---|---|---|
| | $< 1\,\text{m}$ | $< 5\,\text{m}$ | $< 100\,\text{m}$ | $> 100\,\text{m}$ | Solution |
| *AIGL* | | | | | |
| Count | 1907 | 5507 | 26503 | 5296 | 787 |
| | 4.768% | 13.768% | 66.258% | 13.240% | 1.968% |
| *NLSL* | | | | | |
| Count | 5128 | 10241 | 22556 | 2065 | 10 |
| | 12.820% | 25.603% | 56.390% | 5.163% | 0.025% |

Table 7.5: Far field position estimate error using simulated measurement error frequency counts.

The set of comprehensive three dimensional and two dimensional surface plots Figure 7.9 - 7.11 visualize the position error estimates for both AIGL, NLSL and their difference. Figures 7.9 and 7.10 show the error for AIGL and NLSL respectively. Figure 7.11 shows the relative difference in error for AIGL and NLSL.

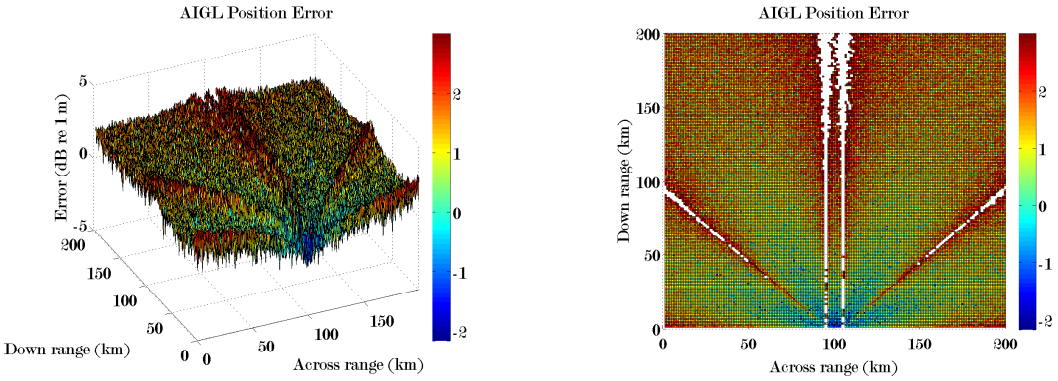


Figure 7.9: The positional estimate error for AIGL in the far field region using simulated measurement error and wider receiver spacing.

The error statistics for AIGL and NLSL are summarized in Table 7.6. A histogram of the estimate error distributions is given in Figure 7.12.

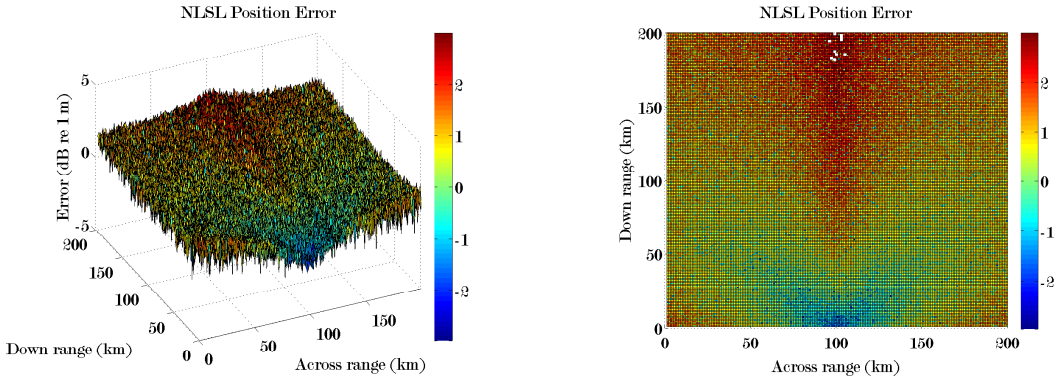


Figure 7.10: The positional estimate error for NLSL in the far field region using simulated measurement error and wider receiver spacing.

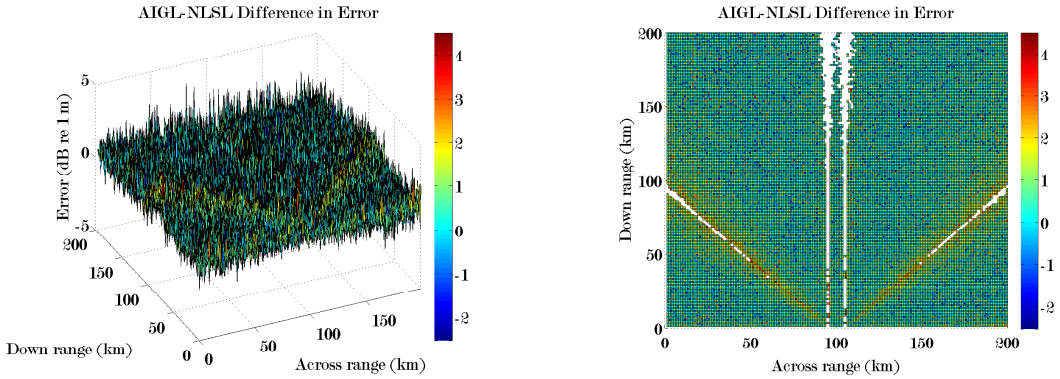


Figure 7.11: The positional estimate difference in error for AIGL and NLSL in the far field region using simulated measurement error and wider receiver spacing.

| | Mean | Variance | Standard Deviation | Null Count |
|---|---|---|---|---|
| *AIGL* | 1.2867 | 0.4947 | 0.7034 | 787 |
| *NLSL* | 0.8605 | 0.5803 | 0.7618 | 10 |

Table 7.6: Far field AIGL and NLSL position estimate log error statistics with measurement error and wider receiver spacing.

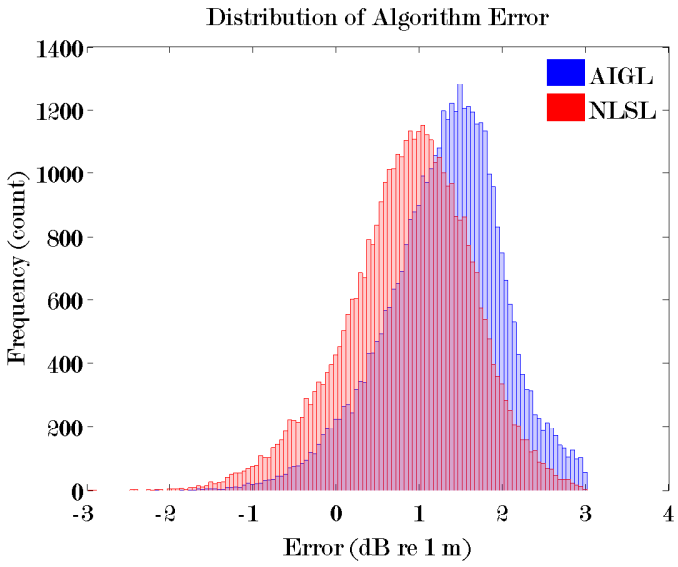


Figure 7.12: Distribution of the positional error for AIGL (blue) and NLSL (red) in the far field using simulated measurement error and wider receiver spacing.

The second set of medium field simulations is configured with the receiver array rotated by 45° as shown in Figure 5.1 (b). Simulation runtime with the rotated array was 14.14 h. The basic summary statistics regarding estimated position error are provided in Table 7.7 and Table 7.8. The frequency counts for different bounds of estimated position error is provided in Table 7.7.

The set of comprehensive three dimensional and two dimensional surface plots Figure 7.13 - 7.15 visualize the position error estimates for both AIGL, NLSL and their difference. Figures 7.13 and 7.14 show the error for AIGL and NLSL respectively. Figure 7.15 shows the relative difference in error for AIGL and NLSL.

The error statistics for AIGL and NLSL are summarized in Table 7.8. A histogram of the estimate error distributions is given in Figure 7.16.

| | Estimated Postion Error Frequency | | | | No |
|---|---|---|---|---|---|
| | $< 1\,\text{m}$ | $< 5\,\text{m}$ | $< 100\,\text{m}$ | $> 100\,\text{m}$ | Solution |
| *AIGL* | | | | | |
| Count | 600 | 3200 | 29246 | 6270 | 684 |
| | 1.500% | 8.000% | 73.115% | 15.675% | 1.710% |
| *NLSL* | | | | | |
| Count | 3786 | 8841 | 26987 | 386 | 0 |
| | 9.465% | 22.103% | 67.468% | 0.965% | 0% |

Table 7.7: Far field position estimate error with rotated receiver array, measurement error and wider receiver spacing.

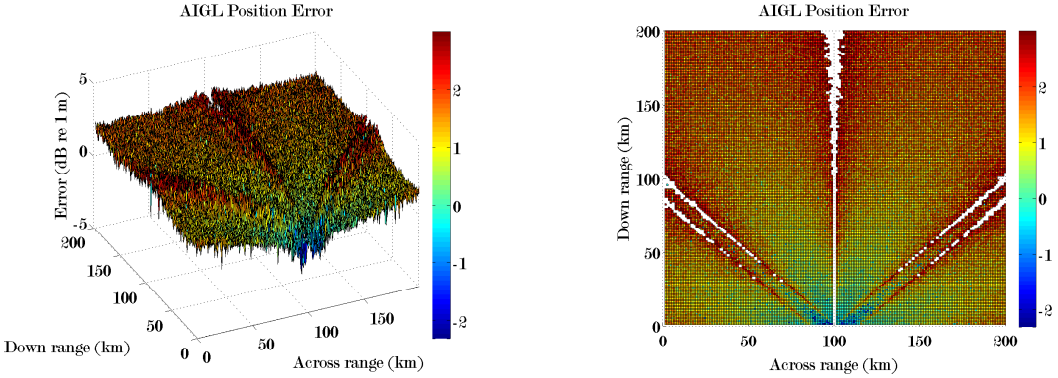


Figure 7.13: The positional estimate error for AIGL in the far field region with rotated receiver array using simulated measurement error and wider receiver spacing.

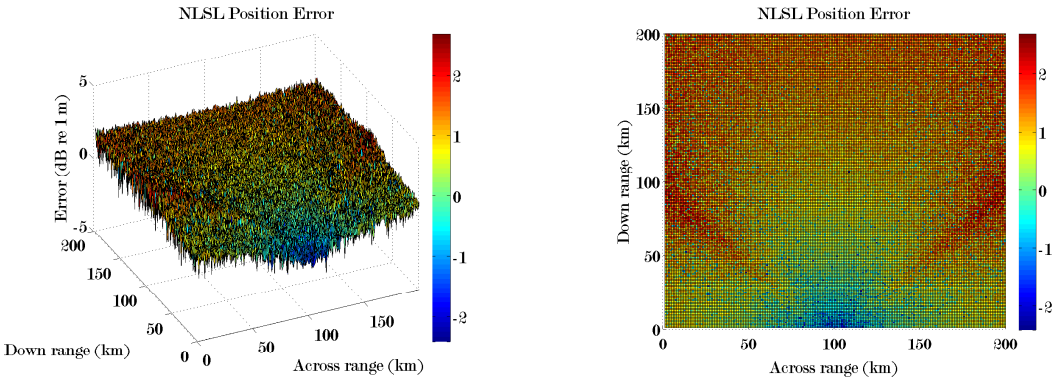


Figure 7.14: The positional estimate error for NLSL in the far field region with rotated receiver array using simulated measurement error and wider receiver spacing.

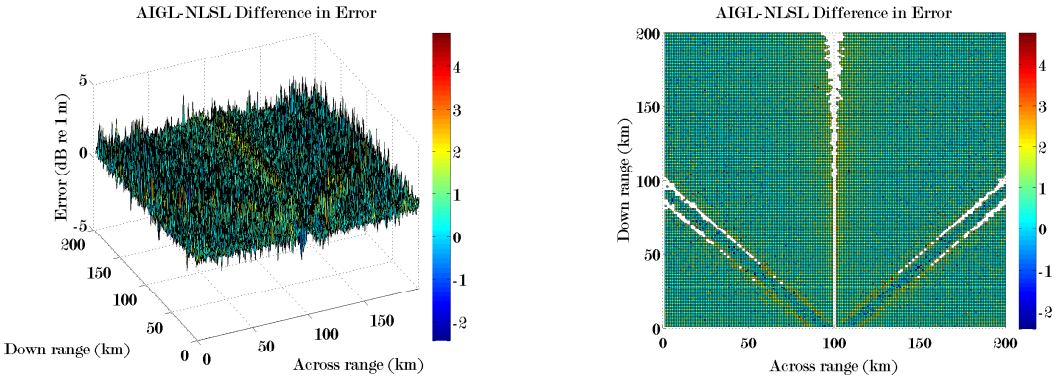


Figure 7.15: The positional estimate difference in error for AIGL and NLSL in the far field region with rotated receiver array using simulated measurement error and wider receiver spacing.

| | Mean | Variance | Standard Deviation | Null Count |
|---|---|---|---|---|
| *AIGL* | 1.4679 | 0.3439 | 0.5864 | 684 |
| *NLSL* | 0.9033 | 0.4134 | 0.6429 | 0 |

Table 7.8: Far field AIGL and NLSL position estimate log error statistics for rotated receiver array with measurement error and wider receiver spacing.

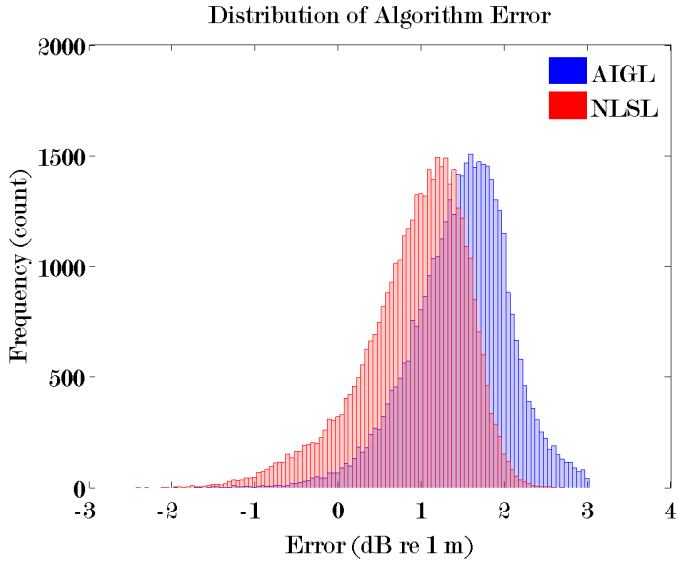


Figure 7.16: Distribution of the positional error for AIGL (blue) and NLSL (red) in the far field with rotated receiver array, measurement error and wider receiver spacing.

## 7.3 Discussion

The diminished performance of the localization algorithms for the larger regions can be rectified by widening the receiver array spacing. Table 7.9 contains statistics for three sets of simulation with external error that have the same simulated source field dimension to receiver spacing dimension ratio.

| | Results of Wider Array Spacing | | | |
|---|---|---|---|---|
| | AIGL | | NLSL | |
| | Standard | Rotated | Standard | Rotated |
| Med-near, Rx 100 m | | | | |
| Mean | 1.41 | 1.43 | 1.02 | 0.99 |
| Std. Dev | 0.67 | 0.65 | 0.72 | 0.61 |
| % Success | 80.1% | 81.4% | 92.0% | 98.0% |
| Null count | 1049 | 702 | 63 | 1 |
| Medium, Rx 1 km | | | | |
| Mean | 1.29 | 1.31 | 0.89 | 0.88 |
| Std. Dev | 0.70 | 0.68 | 0.74 | 0.66 |
| % Success | 84.6% | 84.8% | 94.4% | 98.1% |
| Null count | 809 | 664 | 17 | 0 |
| Far, Rx 10 km | | | | |
| Mean | 1.29 | 1.47 | 0.86 | 0.90 |
| Std. Dev | 0.70 | 0.59 | 0.76 | 0.64 |
| % Success | 84.8% | 82.6% | 94.8% | 99.0% |
| Null count | 787 | 684 | 10 | 0 |

Table 7.9: Simulation statistics for differing source location regions and larger receiver array spacing: Medium-near field with 100 m spacing, medium field with 1 km spacing and far field with 10 km.

The six histograms of the AIGL and NLSL error distributions for the simulated

regions/array combinations included in Table 7.9 are similar. AIGL is always to the right of NLSL which is consistent with the relative mean error in each case. The AIGL and NLSL error distributions have similar shapes and generally the same peak frequency count for all of the source region and array combinations. This indicates that the SBSH algorithms achieve the same level of performance for larger search regions when one is able to increase the spacing on the receiver array. The receiver array dimension used for the far field simulation is quite practical. Typical helicopter assets utilized for AUV operations in polar environments have an endurance of 4 h, cruising speed of 245 km/h and maximum range of 660 km [21]. Given these specifications, a receiver array with spacing on the order of 100 km is possible. Such a receiver array could theoretically support localization in a region 2000 km $\times$ 2000 km which is nearly basin scale.

The localization error remains highest at the fringes where the simulated source is furthest from the receiving array. This fact warrants consideration when determining the ideal spacing for a receiver array for a given region of operations.

The successful location percentage shows a slight increasing trend for the progressively wider spaced receiver arrays because the external error was not changed. By increasing the receiver array and the source location region dimensions, the external error is made smaller relative to those dimensions. The result is improved algorithm performance and a slight reduction in the number of null solutions, i.e. localization with over 1000 m error.

# Chapter 8

# Field Results

## 8.1 General details

Through-ice acoustic data was collected to validate the SBSH algorithms in Prydz Bay, Antarctica near Davis Station, in November of 2010 during the week of station resupply from the *RV Aurora Australis* (Voyage 1-2010). A series of SBSH measurements were staged on land fastened ice in the vicinity of S 68°33′35″, E 77°53′42″. In this chapter, the results of the field data collection were analyzed using the SBSH algorithms. The algorithms were applied with the actual geographic coordinates to evaluate reliability with GPS alone for the geometric layout used for the source and receiver locations. A ping detection software was applied to the acoustic data. This is correlated to the geographic coordinates and the SBSH algorithms were applied to determine the actual source location in the GPS coordinate frame.

### 8.1.1 Test location

During the first station resupply of each season in November, the *RV Aurora Australis* moors in land fastened ice within 3 km of Davis Station to facilitate a multi-day

operation including transfer of cargo, fuel and water. This is a rare and very limited opportunity to conduct data collection on stable Antarctic ice without reliance on considerable assets such as helicopters, flight crews, and avoid interference with resupply activities. Acoustic measurements were staged through ice in water depths of approximately 35 m to 45 m (Figure 8.1). Background acoustic measurements were obtained to ensure that the ship noise from the *RV Aurora Australis*, stationed at S 68°34′1″, E 77°53′58″, would not compromise acoustic data measurements.

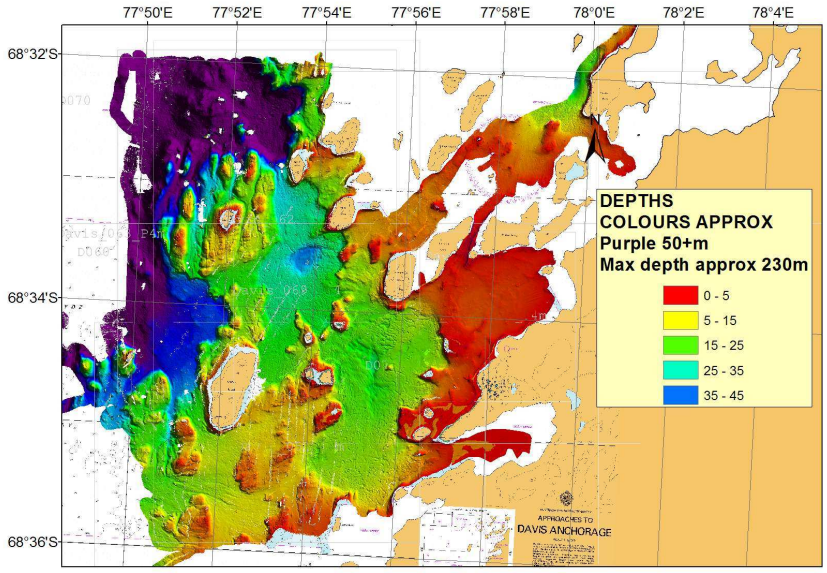


Figure 8.1: Bathymetry in the vicinity of Davis Station, Antarctica. A series of acoustic measurements were conducted in the vicinity of S 68°33′35″, E 77°53′42″.

### 8.1.2 Hardware

The hardware used for data collection was a free-running acoustic beacon and a portable receiver system, i.e. hydrophone. The acoustic beacon, RJE International model number ULB-364/10-PL, was deployed at a set location and stationed until the measurement sequence was concluded. The beacon has a period of 40 s, an operating

frequency of 10 kHz, an omni-directional beam pattern, a power output of 183 dB re 1 µPa and a 5 ms pulse length. The beacon measures 32.20 cm and has a maximum diameter of 6.35 cm across the transducer face. The beacon was customized to emit a short pulse at the start of a relatively long blanking period to enable measurement of the time difference of arrival of a ping without aliasing.

The Portable Receiver System (PRS), RJE International model number PRS-300, utilizes an omni-directional hydrophone and pre-amplifier tuneable to receive frequencies from 5 kHz to 80 kHz with a resolution of 100 Hz. The PRS employs a superheterodyne receiver with a carrier frequency of 1650 Hz. The receiver bandwidth is 1 kHz and hydrophone sensitivity is −196 dB re 1 µPa. An audio output on the PRS was connected to a laptop running a digital audio editor/recording software, Audacity, to record the audio signal.

### 8.1.3 Methods

The data collection procedure consisted of drilling a series of holes through the land fastened ice, approximately 2 m thick. The acoustic beacon was deployed to a depth of 15 m through the first hole, typically the hole closest to potential sources of background acoustic noise, i.e. the *RV Aurora Australis*, unloading activity and airstrip. Then acoustic measurements for the beacon were conducted at subsequent receiving locations using the PRS. Data sets generally consisted of a set of approximately five or more pings so the time of arrival of a ping could be established at successive receiver locations and the difference in time of arrival could be determined. Recording was continuous for the duration of the acoustic measurement exercise. The PRS hydrophone was suspended to a recording depth of 15 m, an operator ensured the required number of pings were recorded, and then hydrophone and system was moved to the next location. The system was not turned off and recording was not stopped

to ensure time difference of arrival reconciliation in post-processing. The hardware was pulled by sledge over the ice to the next receiving location and the process was repeated.

Two complete acoustic localization data sets were collected on different days.

### 8.1.4 Detection

The acoustic ping detection software developed by P. Alexander [131] was extended to incorporate timing information for pings. The ping detection software was applied to the acoustic data collected at each receiving location to determine a ping arrival time that could eventually be used to determine a signal time difference of arrival for each location.

### 8.1.5 Sound speed

Both the acoustic beacon and receiver were deployed through holes in the ice to a depth of 15 m. The depth to pressure conversion using [132] with corrections for the circumpolar Antarctic region determined a pressure of 11.8974 kPa for 15 m depth. The speed of sound was calculated using an updated Chen and Milero equation [133]. It is determined to be $c = 1439.7625\,\mathrm{m/s}$ for a recorded temperature of $-1.8332\,^{\circ}\mathrm{C}$, salinity of 34.4157 PSU and depth of 14.987 m using a Seabird SBE19 CTD.

Given the relatively shallow water in the test area (depths ranged from approximately 35 m to 45 m) there is cylindrical spreading of the acoustic signal. So the influence of acoustic multipath, as shown in Figure 1.1, on the localization result is limited. It would be a consideration in deeper water when spherical spreading will occur.

## 8.2 Field results I

An acoustic localization data set was collected on November 17, 2010: Day One. The general layout of the receiver locations for test Day One is shown in Figure 8.2. The source was stationed at a depth of 15 m and four receiving locations were established north east of the source location. The test layout is not the box style used for the simulation in the previous chapters. The field data collection predated the simulation and the examination of the impact of receiver array configuration on source localization.

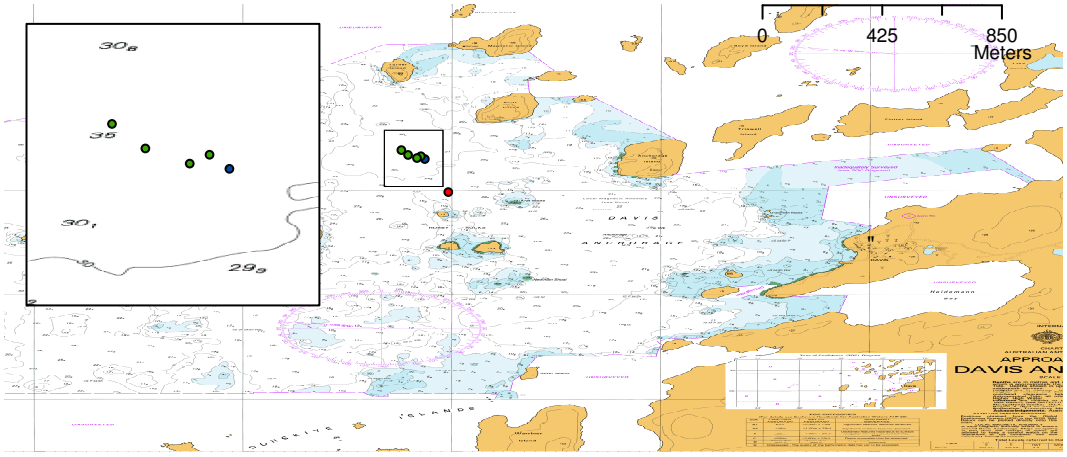


Figure 8.2: Location of source (blue), four sampling locations (green) and the *RV Aurora Australis* (red).

### 8.2.1 Geographic localization

The geographic coordinates for the source and receiving locations are provided in Table 8.1.

The SBSH algorithms were applied to the geographic coordinates alone to determine the source location. The algorithms were evaluated in this manner to isolate the localization performance for actual GPS coordinates, i.e. before acoustic measure-

| | Locations in different coordinate systems | |
|---|---|---|
| | $(latitude, longitude)$ | UTM |
| Source | S 68°33.700′ E 77°53.742′ | (618 083.1748 m, 2 391 535.6176 m) |
| $H_0$ | S 68°33.673′ E 77°53.704′ | (618 059.7241 m, 2 391 586.9626 m) |
| $H_1$ | S 68°33.690′ E 77°53.666′ | (618 032.4277 m, 2 391 556.6142 m) |
| $H_2$ | S 68°33.661′ E 77°53.581′ | (617 977.2260 m, 2 391 613.1739 m) |
| $H_3$ | S 68°33.614′ E 77°53.517′ | (617 937.8577 m, 2 391 702.4816 m) |

Table 8.1: World Geodetic System (WGS 84) and Universal Transverse Mercator (UTM 42D) for the source and receiving locations on November 17, 2010.

ments and timing information were incorporated.

| | Relative distance to $H_0$ |
|---|---|
| $H_1$ | $-1.5275$ m |
| $H_2$ | 74.8548 m |
| $H_3$ | 164.8238 m |

Table 8.2: Difference in radial distance from source relative to reference signal receiver location (Day One).

The geographic positions for $H_0$, $H_1$, $H_2$ and $H_3$ (Table 8.1) and the radial distance difference relative to $H_0$ (Table 8.2) were used to generate an estimate for the source location. The position errors for both SBSH algorithms are given in Table 8.3.

| Position error for SBSH algorithms | |
|---|---|
| $AIGL$ | $6.7577 \times 10^{-4}$ m |
| $NLSL$ | $1.2183 \times 10^{-5}$ m |

Table 8.3: Position estimate error for AIGL and NLSL applied to GPS data for Day One.

### 8.2.2 Acoustic localization

The set of ping times from the acoustic measurements collected on test Day One in Davis are found in Table 8.4.

| | | Ping time (s) | | | |
|---|---|---|---|---|---|
| Source | $H_0$ | $H_1$ | $H_2$ | $H_3$ | $H_3$ |
| 7.63335417 | 638.2049688 | 1226.729958 | 1857.355438 | 2530.034719 | 2992.462344 |
| 49.66828125 | 680.2417396 | 1268.767802 | 1899.393938 | 2572.07349 | 3034.501375 |
| 91.70273958 | 722.279 | 1310.805563 | 1941.432094 | 2614.112188 | 3076.540375 |
| 133.738125 | 764.3159688 | 1352.843625 | 1983.47074 | 2656.150823 | 3118.579573 |
| 175.7737396 | 806.35325 | 1394.881823 | 2025.509531 | 2698.189563 | 3160.618531 |
| 217.8092813 | 848.3905104 | 1436.920094 | 2067.547813 | 2740.228615 | 3202.657708 |
| 259.844875 | 890.4279688 | 1478.958552 | 2109.586531 | 2782.26726 | 3244.696729 |
| 301.8806771 | 932.4652604 | 1520.996719 | 2151.624969 | 2824.306 | 3286.735552 |
| 343.91675 | 974.5029688 | 1563.035198 | 2193.663563 | 2866.344844 | 3328.77426 |
| 385.9528021 | | 1605.073094 | 2235.702375 | 2908.384094 | 3370.812604 |
| | | | 2277.740958 | 2950.423 | |

Table 8.4: Ping detection times at each location for the acoustic localization data (Day One).

Table 8.5 consists of the set of times between pings, i.e. the signal period. The average time between pings was 42.037 928 39 s and has a standard deviation of 0.001 241 286 s.

| | | Signal period (s) | | | |
|---|---|---|---|---|---|
| Source | $H_0$ | $H_1$ | $H_2$ | $H_3$ | $H_3$ cont'd |
| 42.03492708 | 42.03677083 | 42.03784375 | 42.0385 | 42.03877083 | 42.03934375 |
| 42.03445833 | 42.03726042 | 42.03776042 | 42.03815625 | 42.03869792 | 42.03903125 |
| 42.03538542 | 42.03696875 | 42.0380625 | 42.03864583 | 42.03863542 | 42.039 |
| 42.03561458 | 42.03728125 | 42.03819792 | 42.03879167 | 42.03873958 | 42.03919792 |
| 42.03554167 | 42.03726042 | 42.03827083 | 42.03828125 | 42.03905208 | 42.03895833 |
| 42.03559375 | 42.03745833 | 42.03845833 | 42.03871875 | 42.03864584 | 42.03917708 |
| 42.03580208 | 42.03729167 | 42.03816667 | 42.0384375 | 42.03873958 | 42.03902084 |
| 42.03607292 | 42.03770833 | 42.03847917 | 42.03859375 | 42.03884375 | 42.03882291 |
| 42.03605208 | | 42.03789583 | 42.0388125 | 42.03925 | 42.03870834 |
| | | | 42.03858333 | 42.03890625 | 42.03834375 |

Table 8.5: Derived signal period at each receiver location (Day One).

A closer examination of the signal period suggests that there was a drift in the

period which increases slightly over time as clearly shown in Figure 8.3.

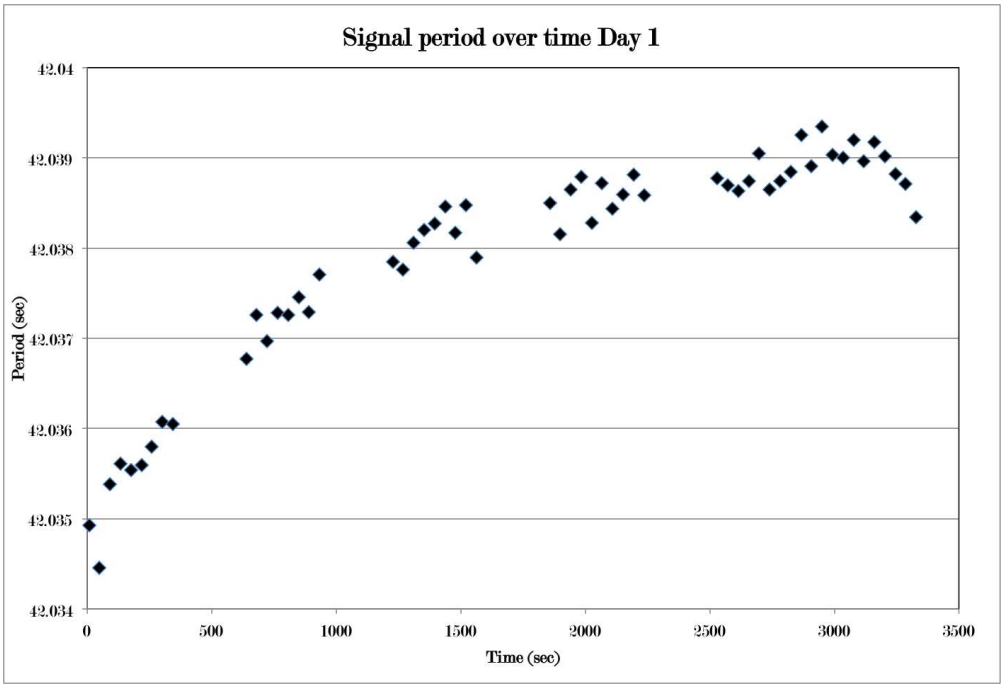


Figure 8.3: The signal period over time. Point clusters (left-right) correspond to sampling locations: source, $H_0$, $H_1$, $H_2$ and $H_3$ respectively. Generally, the period is increasing over time.

Ideally, the period should have been constant and determining the difference in arrival time for the sampled signal ping sequence relative to a reference signal is straightforward. The reference signal is collected at location $H_0$ and the signal period is determined. Measurements are made at the next receiver location $H_1$, then if $H_1$ is further away from the source location, one can subtract the projected ping arrival time based on measurements for $H_0$ (the reference signal) from the actual ping arrival time as measured at $H_1$. In this way, the difference in ping time of arrival can be determined and consequently, a relative difference in distance from the source between $H_0$ and $H_1$ is calculated. After several iterations of this process for the remaining receiver locations, there are sufficient number of values to apply the SBSH algorithms and generate a position estimate for the source location.

For example, the last known ping time for $H_0$ was 974.502 968 8 s. The first ping time recorded at $H_1$ is 1226.729 958 s. A total of six signal periods occurred in the interval between data collection at $H_0$ and $H_1$. Assume that the signal period was constant and was 42.037 928 39 s, then the ping arrival time at $H_0$ corresponding to the ping arrival time 1226.729 958 s at $H_1$ is

$$974.502\,968\,8\,\mathrm{s} + 6 \times 42.037\,928\,39\,\mathrm{s} = 1226.730\,539\,\mathrm{s}.$$

Then the difference in arrival time between $H_1$ and $H_0$ is

$$1226.729\,958\,\mathrm{s} - 1226.730\,539\,\mathrm{s} = -0.000\,580\,732\,\mathrm{s}.$$

The negative time indicates that the first ping recorded at $H_1$ actually arrives before it arrives at $H_0$. This suggests that the distance from $H_1$ to the source location was less than the distance from $H_0$ to the source, i.e. $H_1$ was closer. The relative difference in arrival times for $H_2$ to $H_1$ and $H_3$ to $H_2$ were determined in a similar manner:

$$\begin{aligned} H_2 \text{ rel. to } H_1: \quad & 1605.073\,094\,\mathrm{s} + 6 \times 42.037\,928\,39\,\mathrm{s} = 1857.300\,664\,\mathrm{s} \\ & 1857.355\,438\,\mathrm{s} - 1857.300\,664\,\mathrm{s} = 0.054\,773\,938\,\mathrm{s}, \\ H_3 \text{ rel. to } H_2: \quad & 2277.740\,958\,\mathrm{s} + 6 \times 42.037\,928\,39\,\mathrm{s} = 2529.968\,529\,\mathrm{s} \\ & 2530.034\,719\,\mathrm{s} - 2529.968\,529\,\mathrm{s} = 0.066\,190\,108\,\mathrm{s}. \end{aligned} \tag{8.1}$$

The difference in signal arrival time of $H_2$ relative to $H_0$ was determined by summing $H_2$ relative to $H_1$ and $H_1$ relative to $H_0$

$$0.054\,773\,938\,\mathrm{s} + -0.000\,580\,732\,\mathrm{s} = 0.054\,192\,706\,\mathrm{s}.$$

The time difference of arrival for $H_3$ relative to $H_0$ was found similarly. It was determined to be 0.120 382 814 s. Multiplying the time difference of arrival by the speed of sound $c = 1439.7625\,\mathrm{m/s}$ yields the difference in radial distance from the source relative to $H_0$:

$$\begin{aligned} H_0: \quad \delta_{00} &= 0\,\mathrm{m}; \\ H_1: \quad \delta_{01} &= -0.836\,116\,368\,\mathrm{m}; \\ H_2: \quad \delta_{02} &= 78.024\,626\,\mathrm{m}; \\ H_3: \quad \delta_{03} &= 173.322\,661\,8\,\mathrm{m}. \end{aligned} \tag{8.2}$$

There is a difference in the values of the relative distance in Table 8.3 and the distance values determined in (8.2). The localization result using the (8.2) values is in Table 8.6.

| Position error for SBSH algorithms | |
|---|---|
| $AIGL$ | 54.730 m |
| $NLSL$ | 32.530 m |

Table 8.6: Initial position estimate error for AIGL and NLSL (Day One).

The positional error was large compared to the dimensions of the test. The assumption of a constant period was not appropriate. Instead of using the global average for the period (Table 8.5), a local average was used to project the ping timings between receiver locations. The local averages are determined from the two adjacent locations corresponding to the interval in time for which the projection was required. So, the average of the $H_0$ column and the $H_1$ column of ping times will be applied to determine the time difference of arrival for these two locations. This local average was 42.037 713 85 s. The resultant time difference of arrival for $H_1$ relative to $H_0$ was 0.000 706 491 s. Then the derived relative distances used to determine source location

| | Calculated values using local average | | |
|---|---|---|---|
| | Local avg. | TDOA | Rel. dist |
| $H_1, H_0$ | 42.037 713 85 s | 0.000 706 491 s | 1.017 178 662 m |
| $H_2, H_1$ | 42.038 350 33 s | 0.052 241 776 s | 75.215 750 99 m |
| $H_3, H_2$ | 42.038 780 21 s | 0.061 079 17 s | 87.939 499 11 m |

Table 8.7: Difference in arrival values determined using a local average (Day One).

estimates were:

$$\begin{aligned} H_0: \quad \delta_{00} &= 0\,\text{m}; \\ H_1: \quad \delta_{01} &= 1.0172\,\text{m}; \\ H_2: \quad \delta_{02} &= 76.2329\,\text{m}; \\ H_3: \quad \delta_{03} &= 164.1724\,\text{m}. \end{aligned} \tag{8.3}$$

The source location estimate based on the values in (8.3) is contained in Table 8.8. There was an improvement over the source location determined using the global av-

| Position error using local average | |
|---|---|
| $AIGL$ | 30.461 m |
| $NLSL$ | 13.024 m |

Table 8.8: Position estimate error for AIGL and NLSL using local average (Day One).

erage to determine the difference in ping arrival times (Table 8.6). However, the assumption of a constant period was only slightly relaxed. Applying a local average was treating the signal period as locally constant. This was still contrary to the observed variability in ping periods.

Regression analysis was used to improve the ping time prediction during the interval between signal recordings. Multiple models were employed:

**Linear:** $y = ax + b$

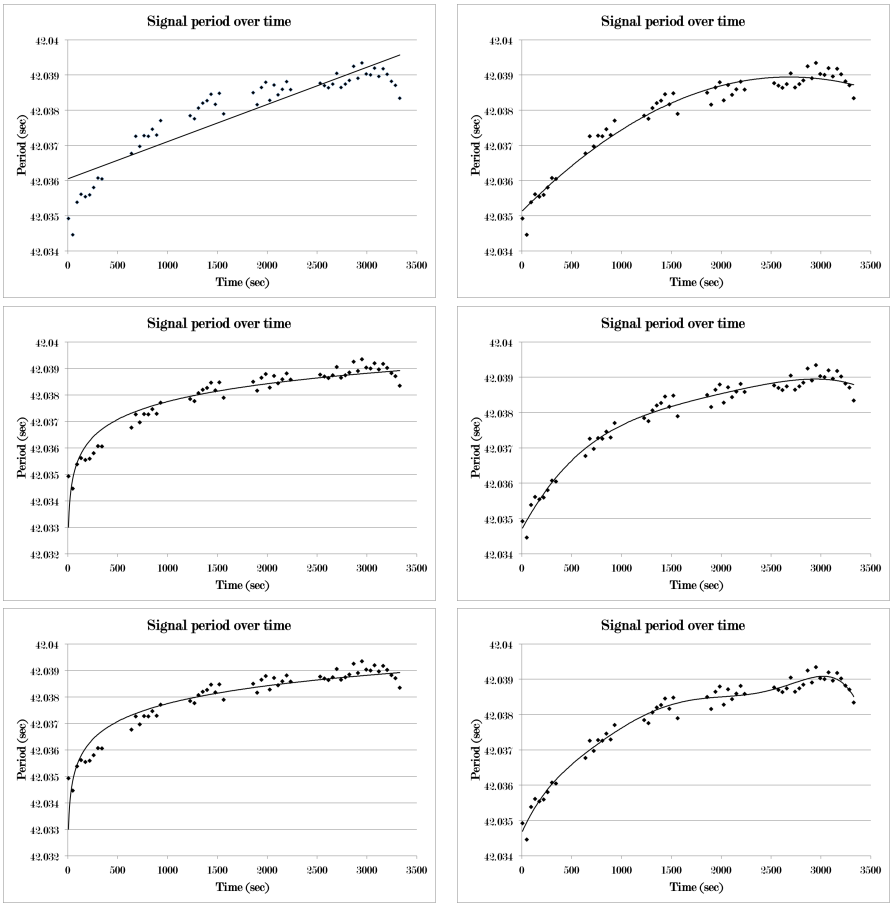


Figure 8.4: Regression models applied to the signal period. Clockwise from bottom-left: power, logarithmic, linear, polynomial degree 2, polynomial degree 4 and polynomial degree 6.

**Logarithmic:** $y = a\ln(x) + b$

**Power:** $y = ax^b$

**Polynomial (Order $n$):** $y = a_n x^n + a_{n-1}x^{n-1} + \cdots + a_1 x + a_0$

Figure 8.4 contains the regression curves determined using various models overlaid on the signal period plotted over time, Figure 8.3.

The equations in Table 8.9 were applied to the acoustic ping data set to generate time difference of arrival values suitable for processing with the SBSH algorithms. The

| Signal period regression models | | |
|---|---|---|
| Type | Equation | $R^2$ |
| linear | $y = 1.0576 \times 10^{-6}x + 42.0360$ | 0.8070723 |
| logarithmic | $y = 9.7322 \times 10^{-4} \ln x + 42.0310$ | 0.8967380 |
| power | $y = 42.0310x^{2.3152\times10^{-5}}$ | 0.8967482 |
| poly (deg. 2) | $y = -5.3156 \times 10^{-10}x^2 + 2.8505 \times 10^{-6} + \ldots$ | |
| | $\ldots + 42.03512$ | 0.9583118 |
| poly (deg. 4) | $y = -1.3182 \times 10^{-16}x^4 + 1.0518 \times 10^{-12}x^3 + \ldots$ | |
| | $\ldots - 3.2587 \times 10^{-9}x^2 + 5.2893 \times 10^{-6}x + 42.0347$ | 0.9729343 |
| poly (deg. 6) | $y = -1.5531 \times 10^{-22}x^6 + 1.4514 \times 10^{-18}x^5 + \ldots$ | |
| | $\ldots - 5.1297 \times 10^{-15}x^4 + 8.7692 \times 10^{-12}x^3 + \ldots$ | |
| | $\ldots - 8.4008 \times 10^{-9}x^2 + 6.4371 \times 10^{-6}x + 42.0346$ | 0.9781246 |

Table 8.9: Regression equations and coefficients of determination for signal period regression models. Note that values are rounded for presentation purposes.

method of projecting the ping period was slightly different than adding a constant number of periods as was done previously for the local average ping projection. The linear regression equation was used to illustrate the method used to project the ping time when the regression models were used.

Consider the last known ping time for $H_0$, 974.502 968 8 s. The linear equation was evaluated with this time to determine the projected period,

$$1.0576 \times 10^{-6} \times (974.502\,968\,8\,\text{s}) + 42.0360\,\text{s} = 42.037\,080\,45\,\text{s}.$$

Then this period was summed with the last known ping time to determine the subsequent ping time,

$$974.502\,968\,8\,\text{s} + 42.037\,080\,45\,\text{s} = 1016.540\,049\,\text{s}.$$

The process was then repeated for this new ping time estimate to determine the next ping time,

$$1016.540\,049\,\text{s} + 1.0576 \times 10^{-6} \times (1016.540\,049\,\text{s}) + 42.0360\,\text{s} = 1058.577\,174\,\text{s}.$$

Four additional iterations of this process resulted in a ping time estimate of 1226.726 118 s. The time difference of arrival for the signal ping was determined to be 0.003 840 036 s, equivalent to a calculated distance of 5.5287 m (using the given sound speed). The same procedure was repeated twice more to determine the set of relative distances for $H_2$ relative to $H_1$ and $H_3$ relative to $H_2$ in order to seed the SBSH algorithm. This mirrored the approach when the local average was employed.

This procedure was followed to determine a source location estimate using each of the ping time regression models. The results are in Table 8.10.

| Type | Localization results using acoustic data | | |
|---|---|---|---|
| | Rel. dist | Error | |
| *linear* | | | |
| | $\delta_{01} = 5.5287\,\mathrm{m}$ | | |
| | $\delta_{02} = 84.9935\,\mathrm{m}$ | **AIGL**: | $46.3296\,\mathrm{m}$ |
| | $\delta_{03} = 174.7502\,\mathrm{m}$ | **NLSL**: | $28.7349\,\mathrm{m}$ |
| *logarithmic* | | | |
| | $\delta_{01} = 0.0986\,\mathrm{m}$ | | |
| | $\delta_{02} = 76.0154\,\mathrm{m}$ | **AIGL**: | $4.8502\,\mathrm{m}$ |
| | $\delta_{03} = 165.5773\,\mathrm{m}$ | **NLSL**: | $2.9853\,\mathrm{m}$ |
| *power* | | | |
| | $\delta_{01} = 0.0987\,\mathrm{m}$ | | |
| | $\delta_{02} = 76.0156\,\mathrm{m}$ | **AIGL**: | $4.8488\,\mathrm{m}$ |
| | $\delta_{03} = 165.5773\,\mathrm{m}$ | **NLSL**: | $2.9794\,\mathrm{m}$ |
| *poly (deg. 2)* | | | |
| | $\delta_{01} = 2.192\,081\,8\,\mathrm{m}$ | | |
| | $\delta_{02} = 76.631\,743\,\mathrm{m}$ | **AIGL**: | $39.7817\,\mathrm{m}$ |
| | $\delta_{03} = 163.587\,61\,\mathrm{m}$ | **NLSL**: | $18.6165\,\mathrm{m}$ |
| *poly (deg. 4)* | | | |
| | $\delta_{01} = 0.7929\,\mathrm{m}$ | | |
| | $\delta_{02} = 76.1476\,\mathrm{m}$ | **AIGL**: | $29.3163\,\mathrm{m}$ |
| | $\delta_{03} = 164.2022\,\mathrm{m}$ | **NLSL**: | $12.2734\,\mathrm{m}$ |
| *poly (deg. 6)* | | | |
| | $\delta_{01} = 0.7084\,\mathrm{m}$ | | |
| | $\delta_{02} = 75.4007\,\mathrm{m}$ | **AIGL**: | $12.5395\,\mathrm{m}$ |
| | $\delta_{03} = 164.6755\,\mathrm{m}$ | **NLSL**: | $12.0431\,\mathrm{m}$ |

Table 8.10: Position estimate error for AIGL and NLSL using ping time regression models (Day One).

## 8.3 Discussion: Field results I

The SBSH algorithms performed well on the GPS data alone. It appeared in this case, the GPS error does not degrade the source location estimate significantly. However, it was clear that accurate characterization of the signal period was critical for determining source location from acoustic data. The processed ping timing data collected from the Day One tests determined a signal period that was not constant. When a constant period was used to derive the relative time difference in arrival times for the receiver locations the result was 54.730 m for AIGL and 32.530 for NLSL. Such a result qualifies as a successful localization, but was not impressive given the relative proximity to the receiver locations.

The local average ping time was used to estimate the signal period between successive receivers and improved the localization result. The localization error was reduced to 30.461 m using AIGL and 13.024 m using NLSL. The effort to improve the signal's period characterization was extended further by applying a series of regression analysis models to the ping time data for the acoustic data set for Day One. The models used were linear, logarithmic, power and polynomial with various orders. Coefficient of determination values ranged from 0.807 to 0.978 for the different models.

Of the regression models, the linear and second order polynomial performed worse than the local average method for signal period estimation. The other polynomial models generated a slightly improved result. However, it was the logarithmic and power regression models that returned the best acoustic localization solution. The AIGL and NLSL error for both models were approximately 4.85 m and 2.98 m respectively.

The regression model that best fits the ping time data does not result in the best localization solution. The polynomial models had the highest coefficient of determination values (Table 8.9), yet it was the logarithmic and power models that yielded a

superior localization result. It might be the case that the optimal localization result was not derived from the regression model that fits best on a ping by ping basis but rather the model that optimally exemplified the behaviour of the period and 'tracked' it best. The radial ranges from $H_0$ to the other receiver locations $H_i$ relative to the source location are shown in Table 8.11.

| | Relative radial range to $H_0$ | |
|---|---|---|
| | Est. range | Actual range |
| $\delta_{01}$: | 0.099 m to 5.528 m | −1.528 m |
| $\delta_{02}$: | 75.401 m to 84.994 m | 74.855 m |
| $\delta_{03}$: | 163.588 m to 174.750 m | 164.824 m |

Table 8.11: Radial distance to $H_0$ relative to source location using regression model estimate and actual (GPS) on Day One

The ranges determined by logarithmic and power models were consistently higher than the actual ranges by approximately 2.5 m or less. Each polynomial model overestimated $\delta_{02}$ and underestimated $\delta_{03}$. The former behaviour was more desirable for the SBSH algorithms. Essentially, the SBSH algorithms relied on recreating the curve front corresponding to the pressure wave for the acoustic signal in order to determine a source location. If the curvature was underestimated by the TDOA circle (at every $H_i$) or overestimated by the TDOA circle (at every $H_i$), then the localization solution does not deviate as far from the actual source compared to situation where the curvature was overestimated and underestimated. A consistent error in curvature primarily resulted in an error increase radially with respect to the source location and receiver array, whereas a mix of curvature overestimates and underestimates shifted the solution tangentially as well. This will be further exacerbated when the source location is further from the receiver array.

## 8.4 Field results II

A second localization data set was collected on November 18, 2010: Day Two. This set differed from the Day One set in several ways. The same source location placement was used and the layout of $H_0$ to $H_3$ was similar; however, the radial distance for each $H_i$ from the source was greater. For example, the new $H_0$ coincided with $H_3$ from the previous set. Additionally, there was one more receiving location, $H_4$ in the receiving array. It was positioned on the side opposite $H_0 - H_3$ relative to the source location. Figure 8.5 describes the layout for the second day of acoustic localization data collection in Antarctica.

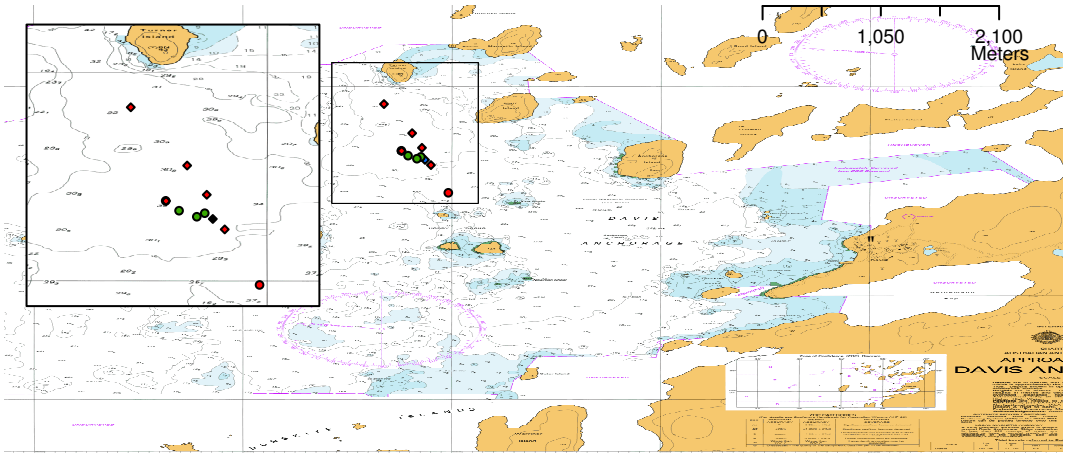


Figure 8.5: Location of source (blue), four sampling locations from Day One (green), five sampling locations from Day Two (red) and the *RV Aurora Australis* (dark red).

Data collection for this data set is similar to the description in Section 8.1.3. The first receiving location sampled was $H_4$ on the southern extent of the receiver array followed by $H_0$, $H_1$, $H_2$, and $H_3$ because of the continuous recording constraint. It was noticed at $H_2$ that data recording had ceased prematurely. The northernmost extent of the receiver array was closer at that point, so the recording procedure was restarted at $H_3$. The data collection order was $H_3$ followed by $H_2, H_1, H_0$ and $H_4$.

### 8.4.1 Geographic localization

Geographic coordinates for the source and receiving locations are provided in Table 8.1

| | Locations in different coordinate systems | |
|---|---|---|
| | $(latitude, longitude)$ | UTM |
| Source | S 68°33.700′ E 77°53.741′ | (618 083.1748 m, 2 391 535.6176 m) |
| $H_0$ | S 68°33.614′ E 77°53.518′ | (617 938.5369 m, 2 391 702.4497 m) |
| $H_1$ | S 68°33.584′ E 77°53.713′ | (618 073.6160 m, 2 391 751.9177 m) |
| $H_2$ | S 68°33.444′ E 77°53.619′ | (618 021.9930 m, 2 392 014.8554 m) |
| $H_3$ | S 68°33.165′ E 77°53.349′ | (617 862.9007 m, 2 392 541.4888 m) |
| $H_4$ | S 68°33.750′ E 77°53.799′ | (618 117.5182 m, 2 391 440.9615 m) |

Table 8.12: World Geodetic System (WGS 84) and Universal Transverse Mercator (UTM 42D) for the source and receiving locations on November 18, 2010.

The SBSH algorithms were applied to the geographic coordinates alone to determine the source location.

| | Relative distance to $H_0$ |
|---|---|
| $\delta_{01}$ | −3.8821 m |
| $\delta_{02}$ | 262.6778 m |
| $\delta_{03}$ | 809.1988 m |
| $\delta_{04}$ | −119.3749 m |

Table 8.13: Difference in radial distance from source relative to reference signal receiver location (Day Two).

The geographic positions for $H_0$, $H_1$, $H_2$, $H_3$ and $H_4$ (Table 8.12) and the radial distance difference relative to $H_0$ (Table 8.13) are used to generate an estimate for the source location. The position errors for both SBSH algorithms are given in Table 8.14.

| Position error for SBSH algorithms | |
|---|---|
| $AIGL$ | $8.0902 \times 10^{-4}\,\mathrm{m}$ |
| $NLSL$ | $1.3281 \times 10^{-5}\,\mathrm{m}$ |

Table 8.14: Position estimate error for AIGL and NLSL applied to GPS data for Day Two.

### 8.4.2 Acoustic localization

The set of ping times from the acoustic measurements collected on Day Two are contained in Table 8.15.

| | | Ping time (s) | | | |
|---|---|---|---|---|---|
| $H_3$ | $H_2$ | $H_2$ | $H_1$ | $H_0$ | $H_4$ |
| 38.07967708 | 920.50875 | 1256.816396 | 1845.170396 | 2391.668896 | 3064.194813 |
| 80.11809375 | 962.5474375 | 1298.854771 | 1887.209042 | 2433.707104 | 3106.232594 |
| 122.1564271 | 1004.585719 | 1340.893135 | 1929.247031 | 2475.7454277 | 3148.270917 |
| 164.1950833 | 1046.624125 | 1382.931188 | 1971.28549 | 2517.783469 | 3190.309094 |
| 206.2336563 | 1088.662656 | 1424.969365 | 2013.323948 | 2559.82174 | 3232.347521 |
| 248.2721771 | 1130.700958 | 1467.007729 | 2055.3625527 | 2601.859594 | 3274.385198 |
| 290.3106042 | 1172.739479 | 1509.04625 | 2097.400958 | 2643.897958 | 3316.42325 |
| 332.3492917 | 1214.77801 | 1551.0845 | 2139.439354 | 2685.935958 | 3358.461604 |
| 374.3879375 | | 1593.122604 | 2181.47776 | 2727.973927 | 3400.499125 |
| 416.4266146 | | | 2223.5161875 | 2770.01222917 | 3442.53736458 |
| 458.4646979 | | | | | |

Table 8.15: Ping detection times at each location for the second acoustic localization data (Day Two).

Table 8.16 consists of the set of times between pings, i.e. the signal period. The average time between pings was 42.038 312 30 s and had a standard deviation of 0.000 258 942 s.

A closer examination of the signal period suggested that there was a drift in the period which decreased slightly over time as shown in Figure 8.6.

The relative time difference of arrival times at each receiver relative to $H_0$ were constructed similar as before. A linear fit for the period was determined between two adjacent recording locations to determine the difference in arrival time for adjacent

| | | Signal period (s) | | | |
|---|---|---|---|---|---|
| $H_3$ | $H_2$ | $H_2$ | $H_1$ | $H_0$ | $H_4$ |
| 42.03841667 | 42.0386875 | 42.038375 | 42.03864584 | 42.03820834 | 42.03778125 |
| 42.03833333 | 42.03828125 | 42.03836459 | 42.03798958 | 42.03832291 | 42.03832292 |
| 42.03865625 | 42.03840625 | 42.03805208 | 42.03845833 | 42.03804167 | 42.03817708 |
| 42.03857292 | 42.03853125 | 42.03817708 | 42.03845834 | 42.03827083 | 42.03842708 |
| 42.03852083 | 42.03830208 | 42.03836459 | 42.03860416 | 42.03785417 | 42.03767709 |
| 42.03842709 | 42.03852084 | 42.03852083 | 42.03840625 | 42.03836458 | 42.03805208 |
| 42.0386875 | 42.03853125 | 42.03825 | 42.03839584 | 42.038 | 42.03835417 |
| 42.03864583 | 42.03838541 | 42.03810417 | 42.03840625 | 42.03796875 | 42.03752083 |
| 42.03867708 | | | 42.03842708 | 42.03830209 | 42.03823958 |
| 42.03808334 | | | | | |

Table 8.16: Derived signal period at each receiver location (Day Two).

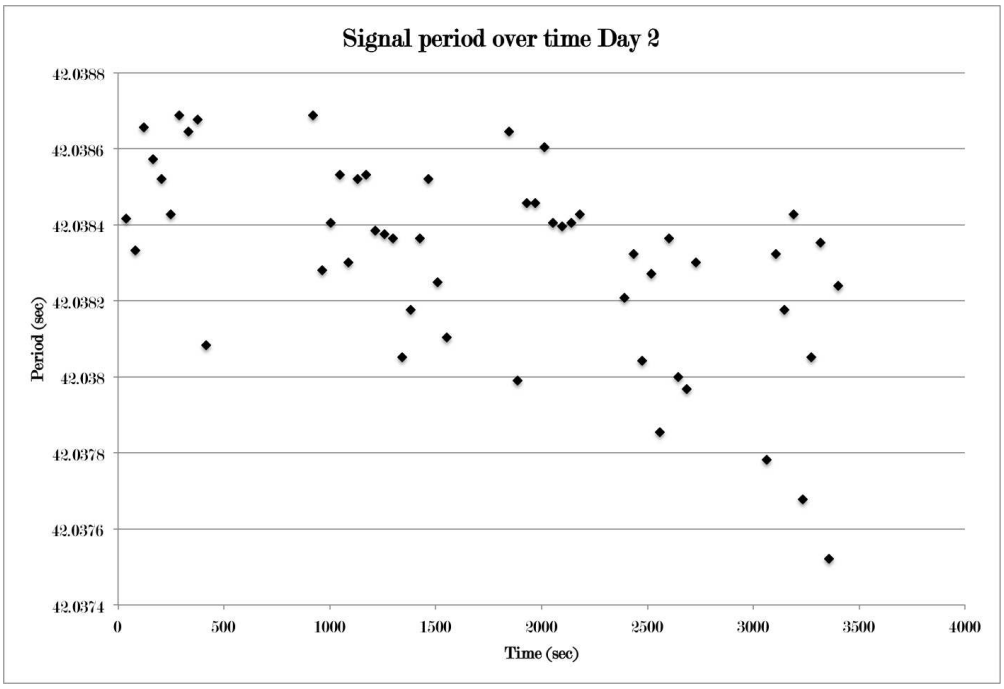


Figure 8.6: The signal period over time. Point clusters (left-right) correspond to sampling locations: $H_3$, $H_2$, $H_1$, $H_0$ and $H_4$ respectively.

receiver locations (Table 8.17).

| | Linear fits used for signal period | |
|---|---|---|
| Locations | Equation | $R^2$ |
| $H_3, H_2$ | $y = -1.61217 \times 10^{-7}x + 42.03855496$ | 0.206638361 |
| $H_2, H_1$ | $y = -4.62993 \times 10^{-9}x + 42.03839285$ | 0.000123464 |
| $H_1, H_0$ | $y = -4.44643 \times 10^{-7}x + 42.03930143$ | 0.348991705 |
| $H_0, H_4$ | $y = -1.40668 \times 10^{-7}x + 42.03851213$ | 0.038435447 |

Table 8.17: Linear regression equations and coefficients of determination for the signal periods of adjacent receiver locations on Day Two.

The relative TDOA and derived relative radial distance between receiver locations is contained in Table 8.18.

| | Relative arrival times and distances | |
|---|---|---|
| Locations | Rel. TDOA | Rel. dist |
| $H_3, H_2$ | $-0.378\,990\,235$ s | $-545.6559$ m |
| $H_2, H_1$ | $-0.182\,799\,771$ s | $-263.1883$ m |
| $H_1, H_0$ | $-0.000\,334\,932$ s | $-0.4822$ m |
| $H_1, H_0$ | $-0.083\,976\,151$ s | $-120.9057$ m |

Table 8.18: Relative difference in arrival times and distances for Day Two. Note that negative signifies radially nearer to source.

The radial distance from the source location relative to $H_0$ is in Table 8.19.

| Rel. radial dist. to reference receiver | |
|---|---|
| $\delta_{00}$ | 0 m |
| $\delta_{01}$ | 0.4822 m |
| $\delta_{02}$ | 263.6705 m |
| $\delta_{03}$ | 809.3264 m |
| $\delta_{04}$ | −120.9057 m |

Table 8.19: Relative radial distances to reference receiver location on Day Two.

| | Localization results | |
|---|---|---|
| Receiver set | AIGL error | NLSL error |
| $\{H_0, H_1, H_2, H_3\}$ : | 13.412 m | 35.116 m |
| $\{H_0, H_1, H_2, H_4\}$ : | 29.858 m | 3.5659 m |
| $\{H_0, H_1, H_3, H_4\}$ : | 19.393 m | 3.7663 m |
| $\{H_0, H_2, H_3, H_4\}$ : | 5.2882 m | 1.7558 m |
| $\{H_1, H_2, H_3, H_4\}$ : | 5.2882 m | 12.738 m |

Table 8.20: Position estimate error for AIGL and NLSL using different sets of receiver locations (Day Two).

## 8.5 Discussion: Field results II

Localization using the geographic coordinates for Day Two (Table 8.14) and Day One (Table 8.3) was comparable. Both AIGL and NLSL algorithms generated a source position estimate that is very accurate with a position error of less than 1 mm in the GPS reference frame. This reinforced an earlier conclusion that GPS error does not compromise the SBSH algorithm performance.

The derived signal period from the Day Two ping times was not constant (Figure 8.6). Linear regression for adjacent receiver locations was used to generate a model to determine the ping time between sampling at receiver locations.

| | Relative radial range to $H_0$ | |
|---|---|---|
| | Est. range | Actual range |
| $\delta_{01}$: | 0.482 m | −3.882 m |
| $\delta_{02}$: | 263.670 m | 262.678 m |
| $\delta_{03}$: | 809.326 m | 809.198 m |
| $\delta_{04}$: | −120.906 m | −119.375 m |

Table 8.21: Radial distance to $H_0$ relative to source location using linear regression model estimates and actual (GPS) on Day Two.

Five different sets of receiver locations were used to generate source location estimates. The localization error for AIGL ranged from 5.288 m to 29.858 m and it ranged from 1.756 m to 35.116 m for NLSL. In two of the five instances the AIGL associated position error was less than then NLSL position error. This was different than Day One results where in every case the NLSL error was less than the AIGL error. For the Day One results, the variations were due to different methods (i.e. regression models) applied to characterize the signal period, whereas, for Day Two results, the receiver locations were interchanged. Nonetheless the NLSL error was superior for Day One in all cases and this was not true for Day Two results. It does agree with

simulation, where clearly there were instances where simulated source location results using AIGL were better than NLSL results.

The optimal localization results for Day Two were comparable with the Day One results. AIGL error was approximately 0.439 m more than the AIGL Day One error and NLSL error improved by 1.223 m on Day Two. The optimal Day Two results utilized receiver locations that had the greatest range from the source location. On Day One, the nearest receiver location was $H_1$ at 54.919 m from the source, while on Day Two, the nearest receiver location, $H_4$, was 100.365 m from the source. It is difficult to categorically state that the Day Two localization was superior to the Day One localization. Day Two had a larger receiver array dimension spacing, which was known to improve localization results in simulation, and a larger distance to the source location compared to Day One, which is known to worsen localization results. The actual error for the optimal result on Day Two was strictly slightly better than the error on Day One, but ultimately the errors for both days were very close for both algorithms.

# Chapter 9

# Summary

There is a distinct requirement for AUV localization technologies to support remote localization of a vehicle. There are only two practical approaches for locating a submerged AUV remotely: look for it or listen for it. Sonar systems can be used to conduct a search for a vehicle but the range is limited, there is a cost to mobilize sonar on a ship or another AUV or ROV, and the environment may render it impossible or impractical due to ice coverage, shallow/shoal, significant depth, etc. Underwater acoustics present a more viable option provided that the vehicle can be outfitted with either an acoustic beacon or transponder prior to deployment. Ultrashort baseline and long baseline systems are the currently commercial accepted technologies to provide this capability and generally use acoustic ranging (i.e. two way communications) to determine a distance and direction to the source. Also, there have been advances in one-way travel time using synchronized clocks between the source and receiver to determine a range. This thesis is predicated on direct experience where dependance on bidirectional signal transfer failed and contributed to the catastrophic loss of an AUV. There is a technology improvement opportunity for a remote AUV localization technology specifically to support emergency acoustic AUV localization in harsh

environments such as beneath ice or in coastal regions.

## 9.1 Conclusion

In this thesis, a novel acoustic localization algorithm is described, tested and implemented which enables one-way, asynchronous acoustic localization of a commercial-off-the-shelf acoustic source. The single-beacon, single hydrophone (SBSH) algorithms are demonstrated to successfully locate a source to within a few meters in a polar operating environment. The contribution of this thesis is a new acoustic tracking technology capable of coarsely localizing an AUV beneath ice.

The motivation for the work was borne of a first hand AUV loss experience and direct participation in the development and planning for extended AUV operations beneath ice. The initial vision for this thesis was to define an iterative process using signal TDOA at successive receiver locations to home in on a signal source. However, it was during those early investigations that the research branched into using the time difference of arrival (TDOA) information directly to remotely localize on a source location. Previous work with the 10 kHz beacon technology used in this thesis determined the effective acoustic detection range to be 5 km for Antarctic operations when the receiver location was a vessel moored in ice [21]. Simulation results have shown that the SBSH localization can effectively locate a source within this range by using a spacing between receiver locations of less than 1 km.

The primary conclusion of this work is that it is possible to remotely locate a missing AUV under ice successfully up to a range of at least 5 km using the technology described in the thesis. The SBSH localization estimate may initially be too coarse; however, an iterative procedure utilizing both the calculated location estimate and the TDOA data (general heading to source) will make it possible to converge on source

location to within an acceptable level of error. It has been demonstrated that TDOA information from a free running acoustic beacon can be used to determine a position estimate suitable for locating a missing AUV.

## 9.2 Future work

Simulation has shown that the localization error can be reduced by increasing receiver location spacing. The general source field location dimension to receiver spacing dimension ratio of 20 results in acceptable performance. That is, if the source is located in a 20 km × 20 km region then the receiver locations should be 1 km apart. However, it should be possible to more precisely determine what this ratio should be to achieve optimal performance to a given localization specification for actual acoustic data sets. Once an acoustic data acquisition and processing system has been prototyped and development has stabilized, then comprehensive system testing can determine an optimal ratio.

The variability in the period signal should be characterized prior to applying the localization algorithms. The comparison of the time between pings between the Day One and the Day Two acoustic localization data sets indicates that the period may be affected more by range to the source than time (i.e. temperature change in hardware due to exposure to extreme temperature fluctuations). A greater emphasis on hardware and system development that provides more accurate timing would benefit the overall performance. The basic commercial hardware built to a relatively loose specification such as was employed in field testing for this thesis can be used to obtain satisfactory localization results by using various techniques such as averaging and regression analysis to reconstruct the signal. This may be a necessary step due to signal period variability arising from environmental conditions; however, a more

precise and stable period signal can contribute to improved localization results.

Further investigation into the period signal should be undertaken by reversing the ping time data set from Day Two and performing a regression analysis to determine if there is a relationship with the Day One ping times and if any conclusions can be inferred. Preliminary efforts in this regard indicate that the coeffecient of determination is lower for each of the regression models; however, further processing of the data may change the result. Some technological modifications could be applied to mitigate this uncertainty in the TDOA. A GPS clock synchronized recording system would enable more accurate timing. If possible, including a second time synchronized receiver would improve signal characterization and TDOA measurements.

The SBSH algorithms (AIGL, NLSL) are different from the algorithms used in an LBL system (spherical, hyperbolic); however, the physical implementation/configuration is related in that the SBSH can be considered as a LBL system with a single receiver that is moved in space and time. The fixed source location for the two acoustic data collection days and the coincidence of the locations $H_3$ (Day One) and $H_2$ (Day Two) can be exploited to further explore signal evolution over time. It also presents an opportunity to examine the substitution of receiving data from the different data sets on the SBSH source localization performance.

The incorporation of additional receiver locations was not employed. It is possible to extend the software to:

- Derive the localization solution based on a combination of both the AIGL and NLSL algorithms; and
- Incorporate additional receiver locations to increase the fidelity of the localization solution.

Perhaps the most significant developmental undertaking should be the gener-

alization of the SBSH algorithms to three dimensions. In general, testing of the algorithm on actual data should be continued. Due to operational and logistical constraints acoustic localization data collection was limited to three days and resulting in two data sets. A statistically significant number of testing cycles is required to formally claim that this TDOA based localization is comparable or superior to the localization performance of current commercially available tracking technologies.

## 9.3 Final thoughts

Finding a missing AUV beneath ice or any missing asset is a process. The optimal end goal of this process is the physical recovery of the platform. The process starts during the vehicle design phase when critical mission constraints are being incorporated into an AUV. Manufacturers and operators might be wary of admitting that their vehicle was actually lost during the design phase or the mission planning phase. Critical decisions are regularly made during design and operations lead up that have consequences during an operation. High level design decision choices regarding navigation system, control architecture, communication system, ballast system, fault response system, etc. ultimately constrain the vehicle performance and operational envelope. Low level design choices such as materials, components, sensor placement, etc. have no less an impact. For example, a proposed root cause of the Autosub loss beneath the Fimbul Ice Shelf in 2005 is due to connector failure [11]. From a technical and operational perspective, it is never too early to consider AUV loss and the response to such an occurrence. If appropriate supports (technical and operational) are in place then the likelihood of recovery will undoubtedly increase in most cases. The SBSH algorithm is demonstrated as a possible tool and one possible piece of that puzzle during a loss event response.

With respect to the SBSH algorithms specifically, a critical consideration is a level of subjectivity regarding algorithm performance, i.e. is localization to within 1 km, 100 m or 1 m suitable. The level of acceptable localization error is mission dependent. A mission plan will indicate acceptable risk thresholds, asset value, collected data value, level of effort, available resources, etc. and other constraints that will help frame what is acceptable and what is unacceptable in terms of localization error. Under-ice bathymetric data in support of international claims to extend a nation's exclusive economic zone has significant value [76]. The potential value of the data surpasses that of the AUV used to collect such data. In this instance and supposing the low frequency acoustic source exists, then a localization system able to find an asset 150 km away to an accuracy of under 2 km but over 1 km will be very useful even if it has a small chance of success.

# Bibliography

[1] R. Lewis, N. Bose, S. Adams, J. Opderbecke and R. Bachmayer, "Preparing the MUN Explorer AUV for sea ice missions," in *Proc. IEEE/OES AUV 2008*, Woods Hole, MA, pp 1-6, 2008.

[2] J. Ferguson, "Adapting AUVs for use in under-ice scientific missions," in *Proc. MTS/IEEE Oceans 2008*, Quebec City, Canada, pp. 1-5, 2008

[3] N. Bose, R. Lewis and S. Adams, "Preparatory tests with an Explorer class Autonomous Underwater Vehicle for missions under sea ice," *Int. J. Ocean and Climate Syst.*, vol. 1, no. 2-3, pp. 145-154, Sept. 2010.

[4] G. Griffiths, N. Millard, S. McPhail, P. Stevenson and P. Challenor, "On the reliability of the Autosub autonomous underwater vehicle," *Underwater Tech.*, vol. 25, iss. 4, pp. 175-184, 2003.

[5] G. Griffiths and A. Trembanis, "Towards a risk management process for Autonomous Underwater Vehicles," in *Proc. Masterclass in AUV Tech. for Polar Sci.*, Southampton, UK, pp. 103-118, 2007.

[6] G. Griffiths and M. Brito, "Predicting risk in missions under sea ice with Autonomous Underwater Vehicle," in *Proc. IEEE/OES AUV 2008*, Woods Hole, MA, pp. 1-7, 2008.

[7] M. Brito, G. Griffiths and P. Challenor, "Risk analysis for Autonomous Underwater Vehicle operations in extreme environments," *Risk Anal.*, vol. 30, iss. 12, pp. 1771-1788, 2010.

[8] M. Brito and G. Griffiths, "A Markov Chain state transition approach to establishing critical phases for AUV reliability," *IEEE J. Ocean Eng.*, vol. 36, pp. 139-149, Jan. 2011.

[9] S. Edwards, "AUVs: How do you insure them?" *Int. Oceans Syst.*, vol. 4, iss. 1, pp. 10-12, 2000.

[10] G. Griffiths, N. Bose, J. Ferguson and D.R. Blidberg, "Insurance for autonomous underwater vehicles," *Underwater Tech.*, vol. 27, no. 2, pp.43-48, 2007.

[11] J. Strutt, "Report on the Inquiry into the Loss of Autosub2 under the Fimbulisen," Boreas Consultants Ltd., Cranfield, UK, Research and Consultancy Report No. 12, 2006.

[12] J. Ferguson, "When things go horribly wrong," in *Proc. Masterclass in AUV Tech. for Polar Sci.*, Southampton, UK, pp. 92-97, 2007.

[13] W. Kirkwood, "AUV incidents and outcomes," in *Proc. MTS/IEEE Oceans 2009*, Biloxi, MI, pp. 1-5, 2009.

[14] M. Doble, P. Wadhams, A. Forrest and B. Laval, "Experiences from two-years' through-ice AUV deployments in the high Arctic," in *Proc. IEEE/OES AUV 2008*, Woods Hole, MA, pp. 1-7, 2008.

[15] S. McPhail, M. Furlong, M. Pebody, J. Perrett, P. Stevenson, A. Webb and D. White, "Exploring beneath the PIG Ice Shelf with the Autosub3 AUV," in *Proc. IEEE Oceans 2009*, Bremen, Germany, pp. 1-8, 2009.

[16] C. Roman and R. Mather, "Autonomous Underwater Vehicles as tools for deep-submergence archaeology," *Proc. Inst. Mech. Eng., Part M: J. Eng. Maritime Environment*, vol. 224, no. 4, pp. 327-340, 2010.

[17] J. Ferguson, A. Pope, B. Butler and R. Verrall, "Theseus AUV - two record breaking missions," *Sea Tech.*, vol. 40, iss. 2, pp. 65-70, 1999.

[18] C. Kunz, C. Murphy, H. Singh, C. Willis, R. Sohn, S. Singh, T. Sato, C. Roman, K. Nakamura, M. Jakuba, R. Eustice, R. Camilli and J. Bailey, "Toward extra-planetary under-ice exploration: Robotic steps in the arctic," *J. Field Robotics*, vol. 26, no. 4, pp. 411-429, 2009.

[19] A. Brierley, P. Fernandes, M. Brandon, F. Armstrong, N. Millard, S. McPhail, P. Stevenson, M. Pebody, J. Perrett, M. Squires, D. Bone and G. Griffiths, "Antarctic krill under sea ice: elevated abundance in a narrow band just south of ice edge," *Science*, 295, pp. 1890-1892, 2002.

[20] A. Jenkins, P. Dutrieux, S. Jacobs, S. McPhail, J. Perrett, A. Webb and D. White, "Observations beneath Pine Island Glacier in West Antarctica and implications for its retreat," *Nature Geoscience*, vol. 3, no. 7, pp. 468-472, 2010.

[21] R. Lewis, M. Drogou, P. King, G. Mann, N. Bose and A. Worby, "An acoustic signal propagation experiment beneath sea ice," *Ocean Eng.*, vol. 43, pp. 56-63, 2012.

[22] D.R. Blidberg, "The development of Autonomous Underwater Vehicles (AUV): A brief summary," in *Proc. Int. Conf. Robotics and Automation*, Seoul, Korea, pp. 1-12, May 2001.

[23] J.C. Dering, ed.,"The Operation of Autonomous Underwater Vehicles Volume One: Recommended Code of Practice", Society for Underwater Technology, 2000.

[24] U.S. Department of the Navy, The Navy Unmanned Undersea Vehicle UUV Master Plan, November, 2004.

[25] Considerations for the Safe Operation of Autonomous Underwater Vehicles (AUVs), International Marine Contractors Association, March 2009.

[26] H. Widditsch, "SPURV - The First Decade," Appl. Physics Lab, U. Wash., Seattle, APL-UW 7215, 1973.

[27] W. Nodland, T. Ewart, W. Bendiner, J. Miller and E. Aagaard, "SPURV II-An Unmanned, Free-Swimming Submersible Developed for Oceanographic Research," in *Proc. MTS/IEEE Oceans 1981*, Boston, MA, pp. 92-98,1981.

[28] W. Nodland, "A General Description of the Self-Propelled Underwater Research Vehicle (SPURV)," Appl. Physics Lab, U. Wash., Seattle, WA, APL-UW 6814, 1968.

[29] R. Francois and W. Nodland, "Unmanned Arctic Research Submersible System Development Report, Phase I," Appl. Physics Lab, U. Wash., Seattle, WA, APL-UW 7108, 1971.

[30] R. Francois and W. Nodland, "Unmanned Arctic Research Submersible (UARS) System Development and Test Report," Appl. Physics Lab, U. Wash., Seattle, WA, APL-UW 7219, 1972.

[31] R. Francois, "The Unmanned Arctic Research Submersible System," *Marine Tech. Soc. J.*, vol. 7 no. 1, pp. 75-77, 1973.

[32] R. Francois and W. Nodland, "Arctic Acoustic Measurements at 50 kHz," Appl. Physics Lab, U. Wash., Seattle, WA, APL-UW 7313, 1973.

[33] J-L. Michel and H. Le Roux, "EPAULARD: Deep Bottom Surveys Now with Acoustic Remote Controlled Vehicle - First Operational Experience" in *Proc. MTS/IEEE Oceans 1981*, Boston, MA, pp. 99-103,1981.

[34] J-L. Michel, "EPAULARD," in *Proc. 2nd Int. Symp. Unmanned Untethered Submersible Tech.*, vol. 2, Durham, NH, pp. 29-30, 1981.

[35] D.R. Blidberg, *AUV System Spec Sheet: ARCS Platform* [Online] Available: http://auvac.org/platforms/view/165, Accessed on: Feb. 4, 2015.

[36] J. Brooke, "ARCS (Autonomous Remotely Controlled Submersible)", in *Proc. 2nd Int. Symp. Unmanned Untethered Submersible Tech.*, vol. 2, Durham, NH, pp. 28, 1981.

[37] J. Ferguson, "Canadian AUV Development 1979 - 2009," in *Proc. 16th Int. Symp. Unmanned Untethered Submersible Tech.*, Durham, NH, 2009.

[38] J. Mooney (chair), "World Technology Evaluation Centre Panel Report on Submersibles and Marine Technologies in Russia's Far East and Siberia," International Tech. Research Inst. - Loyola College in Maryland, Baltimore, MD, 1996.

[39] R. Urich and J. Walton, "Supervisory control of untethered undersea system: A new paradigm verified," in *Proc. 9th Int. Symp. Unmanned Untethered Submersible Tech.*, Durham, NH, pp. 1-5,1995.

[40] C. von Alt, "Autonomous Underwater Vehicles," in *Autonomous Underwater Lagrangian Platforms and Sensors Workshop*, LaJolla, CA, pp. 1-5, 2003.

[41] D.R. Blidberg, E. Allmendinger and N. Sideris, "The development of an unmanned, self-controlled, free-swimming vehicle," in *Proc. 10th Offshore Tech. Conf.*, Houston, TX, pp. 1-10, 1978.

[42] J. Glynn and D.R. Blidberg, "The UNH EAVE-East Vehicle," in *Proc. MTS/IEEE Oceans 1981*, Boston, MA, pp. 104-108,1981.

[43] D. Blidberg, "EAVE East," in *Proc. 2nd Int. Symp. Unmanned Untethered Submersible Tech.* vol. 2, Durham, NH, 1981, pp. 22-26.

[44] J. Jalbert, "EAVE East - Goals and applied technologies," in *Proc. 3rd Int. Symp. Unmanned Untethered Submersible Tech.*, vol. 3, Durham, NH, pp. 62-76, 1983.

[45] P. Heckman and H. McCracken, "An untethered, unmanned submersible," in *Proc. MTS/IEEE Oceans 1979*, San Diego, CA, pp. 733-737, 1979.

[46] P. Heckman, "Free-swimming Submersible Testbed (EAVE West)," Naval Ocean Syst. Center, San Diego, CA, Tech. Report 622, 1980.

[47] J. Durham, P. Heckman, D. Bryan and R. Reich, "EAVE-West: A testbed for plan execution," in *Proc. 5th Int. Symp. Unmanned Untethered Submersible Tech.*, vol. 5, Durham, NH, pp. 33-43, 1987.

[48] J. Jalbert, M. Shevenell, S. Chappell, R. Welsh and D.R. Blidberg, "EAVE III Untethered AUV Submersible," in *Proc. MTS/IEEE Oceans 1988*, vol. 4, Baltimore, MD, pp. 1259-1264, 1988.

[49] S. Dunn and D.R. Blidberg, "On the threshold of maturity - a summary," in *Proc. 6th Int. Symp. Unmanned Untethered Submersible Tech.*, Durham, NH, pp. 573-574, 1989.

[50] T. Ura, "Continuous development of autonomous underwater vehicles - A long way to mid-ocean ridge systems," in *Proc. 15th Int. Symp. Unmanned Untethered Submersible Tech.*, Durham, NH, pp. 1-7, Aug. 2007.

[51] K. Asakawa, J. Kojima, Y. Ito, Y. Shirasaki and N. Kato, "Development of Autonomous Underwater Vehicle for inspection of underwater cables," in *Proc. Underwater Intervention 1993*, New Orleans, LA, pp. 208-216, 1993.

[52] K. Asakawa, J. Kojima, Y. Ito, S. Takagi, Y. Shirasaki and N. Kato, "Autonomous Underwater Vehicle AQUA EXPLORER 1000 for inspection of underwater cables," in *Proc. of IEEE AUV 1996* Monterey, CA, pp.10-17,1996.

[53] C. Bizingre, P. Oliveira, A. Pascoal, F. Pereira, J-P. Pignon, E. Silva, C. Silvestre and J. de Sousa, "Design of a mission management system for the autonomous underwater vehicle MARIUS," in *Proc. IEEE AUV 1994*, Cambridge, MA, pp. 112-121, 1994.

[54] P. Egeskov, A. Bjerrum, A. Pascoal, C. Silvestre, C. Aage and L. Smitt, "Design, construction and hydrodynamic testing of the AUV MARIUS" in *Proc. IEEE AUV 1994*, Cambridge, MA, pp. 199-207, 1994.

[55] R. Seymour (chair), "World Technology Evaluation Centre Panel Report on Submersibles and Marine Technologies in Russia, Ukraine, and Western Europe," International Tech. Research Inst. - Loyola College in Maryland, Baltimore, MD, 1994.

[56] S. McPhail, "Development of a simple navigation system for the Autosub autonomous underwater vehicle," in *Proc. MTS/IEEE Oceans 1993*, Victoria, Canada, pp. 504-509, 1993.

[57] P. Collar and S. McPhail, "Autosub - An autonomous unmanned submersible for ocean data collection," *Electron. and Commun. Eng. J.*, vol. 7, no. 3, pp. 105-114, June 1995.

[58] G. Griffiths, N. Millard, M. Pebody and S. McPhail, "The end of research ships? Autosub - An autonomous underwater vehicle for ocean science," *Proc. of Underwater Tech. Int.: Remote Intervention*, vol. 30, no. 3, pp. 349-362, 1997.

[59] G. Griffiths, K. Birch, N. Millard, S. McPhail, P. Stevenson, M. Pebody, J. Perrett, A. Webb, M. Squires and A. Harris, "Oceanographic surveys with a 50 hour endurance autonomous underwater vehicle," in *Proc. Offshore Tech. Conf.*, Houston, TX, pp. 1-5, May 2000.

[60] G. Griffiths, "Autosub Under Ice," *Ignenia*, iss. 22, pp. 30-32, Mar. 2005.

[61] J. Loch, E. Wallar, J. Bellingham, R. Beaton and M. Triantafyllou, "Software development for the Autonomous Submersible Program at MIT Sea Grant and Draper Laboratory," in *Proc. 6th Int. Symp. Unmanned Untethered Submersible Tech.*, Durham, NH, pp. 25-32, 1989.

[62] J. Bellingham, J. Bales, D. Atwood, C. Chryssostomidis, T. Consi and C. Goudey, "Demonstration of a high-performance, low-cost autonomous underwater vehicle," Massachusetts Inst. of Tech., Cambridge, MA, MITSG 93-28, 1993.

[63] J. Bellingham, C. Goudey, T. Consi, J. Bales, D. Atwood, J. Leonard and C. Chryssostomidis, "A second generation survey AUV," in *Proc. IEEE AUV 1994*, Cambridge, MA, pp. 148-155, 1994.

[64] J. Bellingham, J. Leonard, J. Vaganay, C. Goudey, D. Atwood, T. Consi, J. Bales, H. Schmidt and C. Chryssostomidis, "AUV operations in the arctic," in *Proc. Sea Ice Mechanics and Arctic Modeling Workshop*, Anchorage, AK, pp.1-9,1995.

[65] S. Newburg *AUV Lab History 1991-2001* [Online] Available: http://auvlab.mit.edu/history.html, Accessed on: Feb. 16, 2015.

[66] A. Bradley and D. Yoerger, "Design and testing of the Autonomous Benthic Explorer," in *Proc. 20th Annu. Symp. Assoc. for Unmanned Veh. Syst.*, Washington, DC, pp. 1044-1055, 1993.

[67] D. Yoerger, A. Bradley, H. Singh and R. Bachmayer, "Surveying a subsea lava flow using the Autonomous Benthic Explorer (ABE)," *Int. J. of Syst. Sci.* vol. 29, no. 10, pp. 1031-1044, 1998.

[68] C. von Alt, B. Allen and R. Stokey, "Remote Environmental Measuring Units," in *Proc. IEEE AUV 1994*, Cambridge, MA, pp. 13-19,1994.

[69] H. Singh, R. Eustice, C. Roman and O. Pizarro, "The SeaBED AUV-A platform for high resolution imaging," in *Unmanned Underwater Veh. Showcase Conf. Exhibition*, Southampton, UK, pp. 1-10, 2002.

[70] J. Kristensen and K. Vestgard, "Hugin - an untethered underwater vehicle for seabed surveying," in *Proc. MTS/IEEE Oceans 1998*, vol. 1, Nice, France, 1998, pp. 118-123, 1998.

[71] P. Hagen, N. Storkersen and K. Vestgard, "HUGIN-use of UUV technology in marine applications," in *Proc. MTS/IEEE Oceans 1999*, vol. 2, Seattle, WA, pp. 967-972, 1999.

[72] R. Wernli, "AUVs-the maturity of the technology," in *Proc. MTS/IEEE Oceans 1999*, vol. 1, Seattle, WA, pp. 189-195, 1999.

[73] R. Wernli, "AUV commercialization-who's leading the pack?" in *Proc. MTS/IEEE Oceans 2000*, vol. 1, Providence, RI, pp. 391-395, 2000.

[74] J. McFarlane, "ROVs and AUVs: tools for exploring, exploiting and defending the ocean frontier," in *Proc. Int. Symp. Underwater Tech.*, Tokyo, Japan, pp. 465-471, 2000.

[75] C. Kunz, C. Murphy, R. Camilli, H. Singh, J. Bailey, R. Eustice, M. Jakuba, K. Nakamura, C. Roman, T. Sato, R. Sohn and C. Willis, "Deep sea underwater robotic exploration in the ice-covered arctic ocean with AUVs," in *IEEE/RSJ Int. Conf. Intell. Robots and Syst.*, Nice, France, pp. 3654-3660, 2008.

[76] C. Kaminski, T. Crees, J. Ferguson, A. Forrest, J. Williams, D. Hopkin and G. Heard, "12 days under ice - an historic AUV deployment in the Canadian High Arctic," in *Proc. IEEE/OES AUV 2010*, Monterey, CA, pp. 1-11, 2010.

[77] M. Doble, A. Forrest, P. Wadhams and B. Laval, "Through-ice AUV deployment: Operational and technical experience from two seasons of Arctic fieldwork," in *Cold Regions Sci. Tech.*, vol. 56, pp. 90-97, 2009.

[78] P. King, R. Lewis, D. Mouland and D. Walker, "CATCHY: an AUV ice dock," in *Proc. MTS/IEEE Oceans 2009*, Biloxi, MI, pp. 1-6, 2009.

[79] M. Jakuba, C. Roman, H. Sing, C. Murphy, C. Kunz, C. Willis, T. Sato and R. Sohn, "Long-baseline acoustic navigation for under-ice AUV operations," *J. Field Robotics*, vol. 25, pp. 861-879, 2009.

[80] R. McEwen, H. Thomas, D. Weber and F. Psota, "Performance of an AUV navigation system at Arctic latitudes," *IEEE J. Ocean Eng.*, vol. 30, pp. 443-454, Apr. 2005.

[81] J. Ferguson, "Under-ice seabed mapping with AUVs," in *Proc. IEEE Oceans 2009*, Bremen, Germany, pp. 1-6, 2009.

[82] J. Yu, A. Zhang, Z. Li and K. Yan, "The development and the challenges of underwater vehicles for polar expedition," *Int. Symp. on Underwater Tech.*, Taipei, Taiwan, pp. 95-99, 2004.

[83] A. Kleiner, J. Cheramie, J. Dean and R. Raye, "Ice class AUV development," in *Proc. OTC Arctic Tech. Conf.*, Houston, TX, pp. 1-9, 2011.

[84] T. Stockton and M. McLennan, "Acoustic position measurement, an overview," in *Proc. 7th Offshore Tech. Conf.*, Houston, TX, pp. 255-264, 1975.

[85] K. Vickery, "Acoustic positioning systems. A practical overview of current systems," in *Proc. AUV 1998*, Cambridge, MA, pp. 5-17, 1998.

[86] K. Vickery, "Acoustic positioning systems. New concepts-the future," in *Proc. AUV 1998*, Cambridge, MA, pp. 103-110, 1998.

[87] J. Leonard, A. Bennett, C. Smith and H. Feder, "Autonomous Underwater Vehicle navigation," Massachusetts Inst. of Tech. Marine Robotics Laboratory, Cambridge, MA, Tech. Memorandum 98-1, 1998.

[88] P. Milne, *Underwater Acoustic Positioning Systems*, Houston, TX: Gulf Publishing Co., 1983.

[89] C. Leroy, C. Di Giacomo and J. Prost, "Acoustic measuring system and its performances," in *Proc. 6th Offshore Tech. Conf.*, Houston, TX, pp. 849-863, 1974.

[90] J. Roberts, "An advanced acoustic position reference system," in *Proc. 7th Offshore Tech. Conf.*, Houston, TX, pp. 1-12,1975.

[91] M. Deffenbaugh, J. Bellingham and H. Schmidt, "The relationship between spherical and hyperbolic positioning," in *Proc. MTS/IEEE Oceans 1996*, vol. 2, Ft. Lauderdale, FL, pp. 590-595, 1996.

[92] R. Bucher and D. Misra, "A synthesizable VHDL model of the exact solution for three-dimensional hyperbolic positioning system," *VLSI Design*, vol. 15, no.2, pp. 507-520, 2002.

[93] A. Scherbatyuk, "The AUV positioning using ranges from one transponder LBL," in *Proc. MTS/IEEE Oceans 1995*, vol. 3, San Diego, CA, pp. 1620-1623, 1995.

[94] S. Webster, "Decentralized single-beacon acoustic navigation: Combined communication and navigation for underwater vehicles," Ph. D. dissertation, Johns Hopkins University, Baltimore, MD, 2010.

[95] J. Vaganay, P. Baccou and B. Jouvencel, "Homing by acoustic ranging to a single beacon," in *Proc. MTS/IEEE Oceans 2000*, vol. 2, Providence, RI, pp. 1457-1462, 2000.

[96] M. Larsen, "Synthetic long baseline navigation of underwater vehicles," in *Proc. MTS/IEEE Oceans 2000*, vol. 1, Providence, RI, pp. 2043-2050, 2000.

[97] P. Baccou and B. Jouvencel, "Homing and navigation using one transponder for AUV, postprocessing comparisons results with long base-line navigation," in *Proc. IEEE Int. Conf. Robotics and Automation*, vol. 4, Washington, DC, pp. 4004-4009, 2002.

[98] P. Baccou and B. Jouvencel, "Simulation results, post-processing experimentations and comparisons results for navigation, homing and multiple vehicles operations with a new positioning method using one transponder," in *IEEE/RSJ Int. Conf. Intell. Robots and Syst.*, vol. 1, Las Vegas, NV, pp. 811-817, 2003.

[99] A. Gadre and D. Stilwell, "Toward underwater navigation based on range measurements from a single location," in *Proc. IEEE Int. Conf. Robotics and Automation*, vol. 5, New Orleans, LA, pp. 4472-4477, 2004.

[100] A. Gadre and D. Stilwell, "A complete solution to underwater navigation in the presence of unknown currents based on range measurements from a single location," in *IEEE/RSJ Int. Conf. Intell. Robots and Syst.*, Edmonton, Canada, pp. 1420-1425, 2005.

[101] J. Hartsfield, "Single transponder range only navigation geometry (STRONG) applied to REMUS autonomous underwater vehicles," M.Eng. thesis, Massachusetts Inst. of Tech. and Woods Hole Oceanographic Inst., Cambridge, MA, 2005.

[102] C. LaPointe, "Virtual long baseline (VLBL) autonomous underwater vehicle navigation using a single transponder," M.Eng. thesis, Massachusetts Inst. of Tech., Cambridge, MA, 2006.

[103] J. Jouffroy and J. Reger, "An algebraic perspective to single-transponder underwater navigation," in *Proc. IEEE Int. Conf. Control Applicat.*, Munich, Germany, pp. 1789-1794, 2006.

[104] O. Hegrenas, K. Gade, O. Hagen and P. Hagen, "Underwater transponder positioning and navigation of autonomous underwater vehicles," in *Proc. MTS/IEEE Oceans 2009*, Biloxi, MI, pp. 1-7, 2009.

[105] R. Eustice, L. Whitcomb, H. Singh and M. Grund, "Recent advances in synchronous-clock one-way-travel-time acoustic navigation," in *Proc. MTS/IEEE Oceans 2006*, Boston, MA, pp. 1-6, 2006.

[106] R. Eustice, L. Whitcomb, H. Singh and M. Grund, "Experimental results in synchronous-clock one-way-travel-time acoustic navigation for Autonomous Underwater Vehicles," *Proc. IEEE Int. Conf. Robotics and Automation*, Roma, Italy, pp. 4257-4264, 2007.

[107] R. Eustice, H. Singh and L. Whitcomb, "Synchronous-clock one-way-travel-time acoustic navigation for Underwater Vehicles," *J. Field Robotics*, vol. 28, iss. 1, pp. 121-136, 2011.

[108] S. Webster, R. Eustice, H. Singh and L. Whitcomb, "Preliminary deep water results in single-beacon one-way-travel-time acoustic navigation for underwater vehicles," in *Proc. IEEE/RSJ Int. Conf. Robots and Syst.*, St. Louis, MO, pp. 2053-2060, 2009.

[109] S. Webster, R. Eustice and L. Whitcomb, "Advances in decentralized single-beacon acoustic navigation for underwater vehicles: Theory and simulation," in *Proc. IEEE/OES AUV 2010*, Monterey, CA, pp. 1-8, 2010.

[110] S. Webster, R. Eustice, H. Singh and L. Whitcomb, "Advances in single-beacon one-way-travel-time acoustic navigation for underwater vehicles," *Int. J. Robotics Research*, vol. 31, iss. 8, pp. 935-949, 2012.

[111] S. McPhail and M. Pebody, "Range-only positioning of a deep-diving Autonomous Underwater Vehicle from a surface ship," *IEEE J. Ocean Eng.*, vol. 34, pp. 669-677, Oct. 2009.

[112] P. Trefethen, "Sonic equipment for tracking individual fish," Special Scientific Report of the U.S. Fish and Wildlife Service 179, pp. 1-11, 1956.

[113] W. Watkins and W. Schevill, "Sound source location by arrival-times on a non-rigid three dimensional hydrophone array," *Deep Sea Research*, vol. 19, pp. 691-706, 1972.

[114] A. Young, P. Tytler, F. Holliday and A. MacFarlane, "A small sonic tag for measurement of locomotor behaviour in fish," *J. Fish Biology*, vol. 4, iss. 1, pp. 57-65, Jan. 1972.

[115] A. Hawkins, D. MacLennan, G. Urquhart and C. Robb, "Tracking cod *Gadus morhua L.* in a Scottish sea loch," *J. Fish Biology*, vol. 6, iss. 3, pp. 225-236, May 1974.

[116] P. Bagley and I. Priede, "An autonomous free-fall acoustic tracking system for investigation of fish behavior at abyssal depths," *Aquatic Living Resources*, vol. 10, pp. 67-74, 1997.

[117] J. Ehrenberg and T. Steig, "A method for estimating the "position accuracy" of acoustic fish tags," *ICES J. Marine Sci.*, vol. 59, pp. 140-149, 2002.

[118] K. Stafford, C. Fox and D. Clark, "Long-range acoustic detection and localization of blue whale calls in the northeast Pacific Ocean," *J. Acoust. Soc. Amer.*, vol. 104, iss. 6, pp. 3616-3625, 1998.

[119] R. Morrissey, J. Ward, N. DiMarzio, S. Jarvis and D. Moretti, "Passive acoustic detection and localization of sperm whales (*Physeter macroephalus*) in the tongue of the ocean," *Appl. Acoust.*, vol. 67, pp. 1091-1105, 2006.

[120] C. Tiemann, M. Porter and J. Hildenbrand, "Localization of marine mammals near Hawaii using an acoustic propagation model," *J. Acoust. Soc. Amer.*, vol. 115, iss. 6, pp. 2834-2843, 2004.

[121] C. Tiemann, S. Martin and J. Mobley, "Aerial and acoustic marine mammal detection and localization on navy ranges," *IEEE J. Ocean Eng.*, vol. 31, pp. 107-119, Jan. 2006.

[122] A. Alcocer, P. Oliveira and A. Pascoal, "Underwater acoustic positioning systems based on buoys with GPS," in *Proc. 8th European Conf. Underwater Acoust.*, Carvoeiro, Portugal, pp. 1-8, 2006.

[123] M. Black and B. Butler, "Arctic Ocean trials of Trackpoint ultrashort baseline acoustic positioning systems," *Proc. IEEE AUV 1994*, Cambridge, MA, pp. 297-302, 1994.

[124] M. Deffenbaugh, H. Schmidt and J. Bellingham, "Acoustic navigation for Arctic under-ice AUV missions," *Proc. MTS/IEEE Oceans 1993*, vol. 1, Victoria, Canada, pp. 1204-1209, 1993.

[125] A. Ayres and T. Calkins, "Acoustic position measurement systems," in *Proc. MTS/IEEE Oceans 1977*, Los Angeles, CA, pp. 771-774, 1977.

[126] R. Schmidt, "A new approach to geometry of range difference location," *IEEE Trans. Aerosp. Electron. Syst.*, vol. 8, pp. 821-835, Nov. 1972.

[127] H. Coxeter, "The problem of Apollonius," *Amer. Math. Monthly*, vol. 75, iss. 1, pp. 5-15, 1968.

[128] J. Hoshen, "The GPS equations and the Problem of Apollonius," *IEEE Trans. Aerosp. Electron. Syst.*, vol. 31, pp. 1116-1124, Jul. 1996.

[129] J. Coolidge, *A Treatise on the Circle and the Sphere*, Oxford, Clarendon Press, 1916.

[130] J. Smart, *Modern Geometries*, 3rd ed. Pacific Grove, CA, Brooks/Cole Publishing Co., 1988.

[131] P. Alexander, Modelling acoustic propagation under-ice in support of AUV missions in Antarctica, Ph. D. dissertation, University of Tasmania, Hobart, Tasmania, 2014.

[132] C. C. Leroy and F. Parthiot, "Depth-pressure relationship in the oceans and seas,"*J. Acoust. Soc. Am.*, vol. 103, no. 3, pp. 1346-1352, 1998.

[133] G.S.K. Wong and S. Zhu, "Speed of sound in seawater as a function of salinity, temperature and pressure," *J. Acoust. Soc. Am.*, vol. 97 no. 3, pp. 1732-1736, 1995.